Titre: Title:	Metallic Foam Formation During Continuous Hot-Dip Galvanizing of Steel Sheet
Auteur: Author:	Chris Koutsaris
Date:	2011
Type:	Mémoire ou thèse / Dissertation or Thesis
Référence: Citation:	Koutsaris, C. (2011). Metallic Foam Formation During Continuous Hot-Dip Galvanizing of Steel Sheet [Master's thesis, École Polytechnique de Montréal]. PolyPublie. https://publications.polymtl.ca/603/

UNIVERSITÉ DE MONTRÉAL

METALLIC FOAM FORMATION DURING CONTINUOUS HOT-DIP GALVANIZING OF STEEL SHEET

CHRIS KOUTSARIS

DÉPARTEMENT DE GÉNIE CHIMIQUE

ÉCOLE POLYTECHNIQUE DE MONTRÉAL

MÉMOIRE PRÉSENTÉ EN VUE DE L'OBTENTION

DU DIPLÔME DE MAÎTRISE ÈS SCIENCES APPLIQUÉES

(GÉNIE CHIMIQUE)

JUIN 2011

UNIVERSITÉ DE MONTRÉAL

ÉCOLE POLYTECHNIQUE DE MONTRÉAL

Ce Mémoire intitulé:

METALLIC FOAM FORMATION DURING CONTINUOUS HOT-DIP GALVANIZING OF STEEL SHEET

présenté par : KOUTSARIS Chris

en vue de l'obtention du diplôme de : Maîtrise ès Sciences Appliquées

a été dûment accepté par le jury d'examen constitué de :

M. BALE Christopher W., Ph.D., président

M. AJERSCH Frank, Ph.D., membre et directeur de recherche

M. TURENNE Sylvain, Ph.D., membre

When you change the way you look at things, the things you at change.

-- *Max Planck*

ACKNOWLEDGMENTS

To begin with, I would like to thank Dr. Frank Ajersch for taking me on as one of his graduate students. I am a better engineer today because of him; he is my mentor, my friend. Next, I would like to show my appreciation for the people I worked with at the Industrial Materials Institute-NRC in Boucherville Quebec. This includes Dr. Andre Moreau and especially Mr. Andre Hamel for helping me deal with the “lightning fast” work environment in government institutions. And lastly, I would like to thank the International Lead and Zinc Research Organization for funding my work.

RÉSUMÉ

Depuis la révolution industrielle, le revêtement de l'acier par le zinc a été utilisé pour améliorer la durabilité et la performance des structures. Les revêtements de zinc fournissent un moyen économique de protection de l'acier contre la corrosion. Cette protection pourrait économiser d'un pays industrialisé au moins 4% du PIB à chaque année. La fabrication de structures utilisant de l'acier zingué ou galvanisé est caractérisée par un ensemble unique de propriétés: haute résistance, formabilité, poids léger, résistance à la corrosion, l'esthétique, recyclablilité et faible coût. L'acier galvanisé est utilisé pour la fabrication des appareils ménagers et dans des structures industrielles, domestiques et décoratives. Toutefois, l'application la plus importante en valeur commerciale est l'acier galvanisé en formes de tôles destiné pour la fabrication de carrosseries d'automobiles. Les tôles avec ce revêtement sont produites dans un processus complexe métallurgique de galvanisation en continu. Deux différentes couches sont produites commercialement. Ce qui distingue les revêtements est la composition du bain et le traitement thermique subséquent. Le produit galvanneal (GA) utilise un bain contenant 0.11 à 0.14 % Al et subit un traitement thermique à la sortie du bain. Le produit galvanisé (GI) utilise un bain contenant 0.16 à 0.20 % Al et ne subit pas un traitement thermique.

Les rouleaux d'acier de différentes largeurs et épaisseurs sont déroulés et ensuite revêtus en continu par l'immersion rapide dans un bain d'alliage de zinc liquide à une température entre 450 °C et 480 °C. Une des préoccupations majeures affectant le processus de revêtement est la perte de zinc liquide en forme d'écumes. Les écumes sont des mousses métalliques qui sont produites dans la région où la tôle d'acier sort de la cuve de galvanisation. La formation des écumes est due aux conditions d'écoulement turbulent et à l'atmosphère oxydante dans cette région. Ce produit, appelé *«skimmings»* est écumé de la surface du bain et traité ultérieur pour récupérer le zinc. La présente porte sur l'étude du mécanisme de formation des skimmings et sur sa caractérisation.

Le travail fait partie d'un projet parrainé par l'International Lead and Zinc Research Organization (ILZRO) intitulé ZCO-55: «*Minimisation of skimmings formation in the galvanizing bath*». L'objectif général de ce projet consiste d'étudier l'interaction de l'air provenant des

couteaux d'essuyage (air knives) et le zinc qui est retourné vers le bain le long de la bande émergent. Deux compagnies ont accepté de participer à cette étude; ArcelorMittal Cleveland et U.S.Steel Hamilton. Ces deux aciéries ont contribué des échantillons de skimmings provenant de leurs opérations de galvanisation afin d'étudier leur taux de production d'écume et leur morphologie. Par ailleurs, seulement ArcelorMittal a fourni des feuilles de données des paramètres d'opération. Ces données ont été enregistrées pendant la période d'Octobre 2008 à Mars 2009. Les donnés ont été étudiés et traités afin de déterminer les paramètres du procédé qui avaient le plus grand effet sur la production de skimmings. Aussi, deux différentes expériences en laboratoire ont été réalisées pour simuler la formation des écumes dans le bain de zinc liquide en utilisant un creuset fermé rempli de zinc liquide, un agitateur en acier et un jet de gaz. Les résultats ont montré que le taux de formation des écumes augmente avec la vitesse de rotation de l'agitateur. Aussi, les alliages GI exposés au jet d'air produisent plus d'écumes par unité de temps que les alliages GA exposés au jet d'azote. Finalement, le taux de formation des écumes a diminué quand le creuset était couvert. Les résultats des deux cas ont été comparés pour illustrer les différences entre un creuset ouvert en utilisant un jet d'air. Une deuxième expérience a été réalisées pour simuler le transfert de mass des constituants dans le zinc liquide et l'air sur la surface du bain de galvanisation en se servant d'un jet d'air submergé dans un creuset rempli de zinc liquide. Les coefficients de transfert de mass de l'aluminium et du fer dans une solution liquide de zinc ont été évalué et ils se comparent favorablement avec la littérature.

Caractérisations des écumes

Des particules intermétalliques peuvent aussi se former dans le bain pendant la galvanisation en continu. Ces particules sont également connues comme *«dross»*. Le dross est composé des intermétalliques Al-Fe contenant du Zn (top dross) ou des intermétalliques Fe-Zn avec de l'Al (bottom dross). L'origine de ces particules est du à la réaction de fer dans la solution lors de l'immersion des tôles d'acier qui réagissent avec le zinc et l'aluminium selon leur solubilité. Il se forme une première couche intermétallique de Fe_2Al_5 à la surface de l'acier. Cette couche est très adhérente sur laquelle se fait le dépôt de l'alliage du bain. Des particules de dross continuent à précipiter dans le bain pendant le fonctionnement normal de la ligne de galvanisation. Top dross, $Fe_2Al_5Zn_x$ (phase η), est principalement formé au cours de l'opération GI. Ces particules flottent

à la surface du bain, car les particules sont moins denses que la solution de zinc. Bottom dross, $FeZn_{10}Al_y$ (phase δ), est principalement formée dans l'opération GA. Ces particules se déposent au fond du bain, car ils sont plus denses que la solution de zinc. Cependant, il est aussi possible que les particules de phase η et δ coexistent lors des opérations de GI. La galvanisation en continue est rarement, sinon jamais, un processus à l'équilibre. Les fluctuations constantes de la température, de la teneur en aluminium et de fer dans différentes régions du bain empêchent la solution d'atteindre l'équilibre chimique. Néanmoins, les diagrammes de phase du système Zn-Fe-Al ont été développées afin de mieux comprendre les conditions thermodynamiques dans lesquelles se forment le top dross et le bottom dross. Pour un bain de galvanisation à l'équilibre chimique à 460 °C, la phase η, δ et le liquide coexistent à la composition d'aluminium d'environ 0,135 % en poids. En dessous de cette concentration d'aluminium, la phase δ précipite de la solution. La phase η précipite dans la solution lorsque le bain est au-dessus de 0,135 % Al en poids.

Les skimmings sont écumés de manière manuelle ou par méthode robotisée. En général, les skimmings constituent d'un mélange poreux de zinc liquide du bain, des oxydes et des particules de dross. Cependant, il est clair que la plupart des oxydes sont produites par le jet d'air des couteaux essuyages lorsque le gaz d'essuyage est de l'air. Le gaz d'essuyage et le flux de zinc qui retourne au bain repousse les skimmings vers les bords du bain. Les analyses statistiques provenant de l'industrie ont montré que la pression d'essuyage, l'hauteur des couteaux d'essuyages, la vitesse et la largeur de la tôle d'acier ont tous un impact sur le taux de formation des skimmings. Par conséquent, la dynamique des fluides du zinc liquide dans la région de sortie de la tôle a une importance critique dans la compréhension du mécanisme de l'interaction air-zinc, qui est à l'origine de la formation des skimmings.

L'oxydation du liquide dans le bain de galvanisation en continu est contrôlée par le transfert des constituants liquides vers l'interface gazeux. Par conséquent, il est raisonnable de supposer que l'oxydation de l'alliage de zinc liquide ne produira pas un mélange d'équilibre de scories complexes de O, Zn, Fe et Al. Donc, ce travail suppose que la formation d'oxydes est le résultat des réactions chimiques suivantes:

$$Zn_{(l)} + {}^{1}/_{2}\, O_{2_{(g)}} \rightarrow ZnO_{(s)}$$

$$2Al_{(l)} + {}^{3}/_{2}\, O_{2_{(g)}} \rightarrow Al_2O_{3_{(s)}}$$

$$2Fe_{(l)} + {}^{3}/_{2}\, O_{2_{(g)}} \rightarrow Fe_2O_{3_{(s)}}$$

Les expériences en laboratoire de bullage de l'air dans le bain liquide ont simulé ces réactions à l'interface gaz-liquide. Il existe une littérature considérable sur le comportement et la réaction de bulles de gaz dans les liquides à température ambiante. Cependant, la littérature sur la réaction de bulles de gaz dans les métaux liquides à haute température est très limitée. Les difficultés de l'expérimentation à haute température empêchent également le progrès concernant l'interaction entre la bulle de gaz et le métal liquide. D'importance particulière est l'estimation de la taille des bulles générées par un tube submergé avec un débit de gaz contrôlées pour la détermination expérimentale des coefficients de transfert de masse pour les interactions entre les bulles et le métal liquide. Certains chercheurs ont montré que le comportement de bulles de gaz dans les métaux liquides est semblable à celui des bulles dans les liquides à basse température sous certaines conditions.

Analyse des données industrielles et les résultats des essais en laboratoires

La section 3.1 présente une caractérisation des écumes produites par deux différentes lignes de galvanisations (ArcelorMittal Cleveland et U.S.Steel Canada). La ligne d'ArcelorMittal Cleveland utilise de l'air ou de l'azote comme gaz d'essuyage alors que la ligne d'U.S.Steel Canada utilise l'azote exclusivement. Le résultat de cette étude identifie les paramètres opérationnels qui on la plus grande influence sur la génération des skimmings. L'approche détaillée de l'analyse statistique utilisée dans cette étude est présenté dans l'**Annexe 1**. Les montants de skimmings générés par la ligne d'ArcelorMittal Cleveland pour des opérations galvanneal et galvanisé ont été examinés. L'analyse montre que le bain de GI produit plus de skimmings que le bain GA. En fait, le bain de GI produit 38% plus de skimmings par unité de temps au cours de la même période que le bain de GA. En plus, les microstructures illustrant les

caractéristiques physiques et la composition des constituants des skimmings, déterminé par spectroscopie X à dispersion d'énergie, a aussi été présentée.

La section 3.2 présente les résultats des essais en laboratoire simulant les conditions industrielles de la formation des skimmings. Les expériences consistent de l'agitation d'environ 20 kg de zinc fondu avec un agitateur en acier dans un creuset fermée ou ouvert. Au même temps, un jet d'azote ou d'air a été dirigé sur la surface liquide du bain. L'agitateur et le jet pourraient, respectivement, simuler la tôle mobile et les couteaux d'essuyages trouvés dans l'industrie. Ces expériences peuvent, simuler la région de sortie de la tôle dans un bain de galvanisation industrielle. Néanmoins, les tendances observées au chapitre 3 ont démontré que la génération d'écume dans des conditions laboratoire représente bien les conditions industrielles. À vitesse de rotation faible, les deux solutions GA et GI génèrent des quantités similaires de skimmings par unité de temps. D'autre part, la solution GI produit 51 % plus de skimmings par unité de temps à une vitesse de rotation moyenne et 143 % plus de skimmings par unité de temps à une vitesse de rotation élevée. La constatation de l'effet de la composition du bain et le degré d'agitation sur le taux de génération de skimmings n'a pas été documentée dans la littérature, et par conséquence représente une contribution originale d'importance pour l'industrie. Les résultats montrent que deux facteurs contribuent à la stabilisation de la structure de la mousse d'écume produite dans un bain de GI: la présence de top dross et d'oxyde d'aluminium en raison de niveaux élevés d'aluminium dans le liquide.

Enfin, dans les sections 3.3 et 3.4, les données de skimmings industrielles fourni par ArcelorMittal Cleveland ont été revues et une nouvelle série d'expériences à échelle de laboratoire a également été menée. Les résultats des sections 3.1 et 3.2 ont montré une façon dont la génération de skimmings peut être quantifiée de manière fiable dans un bain de galvanisation. L'analyse de la section 3.3 a démontré que les skimmings produites par unité de surface de rouleau sont plus cohérentes. Par ailleurs, le transfert de masse entre l'air et le zinc liquide a été étudié aussi. La méthodologie utilisée pour calculer les propriétés des bulles de gaz est indiqué dans l'**Annexe 2**. À la section 3.2, la période durant laquelle la ligne de galvanisation en continu d'ArcelorMittal opérait avec de l'azote et de l'air a été examiné et réanalysé à la

section 3.3. Les valeurs calculées des skimmings par unité de surface par temps de séjour de tôle (section 3.2) demontrent une dispersion beaucoup plus large au fil du temps que les valeurs calculées pour les skimmings par unité de surface de tôle (section 3.3). Par exemple, à la section 3.2, le taux de production moyen était de 44,3 ± 25,0 g/m^2/hr pour l'essuyage avec l'azote et 103 ± 83,9 g/m^2/hr pour essuyage avec l'air. Alors qu'à la section 3.3, le taux de production moyen des skimmings était 11.2 ± 4,15 g/m^2 pour l'essuyage avec de l'azote et 18,6 ± 9,37 g/m^2 pour l'essuyage avec de l'air pour la même période. En d'autres termes, 11,2 g/m^2 ± 37% versus 44,3 g/m^2/hr ± 56% pour l'essuyage avec de l'azote et 18,6 g/m^2 ± 50% versus 103 ± 81% g/m^2/hr pour l'essuyage avec de l'air. En ce qui concerne le reste des données industrielles, la masse de skimmings produite par unité de surface de rouleau représente mieux la formation spécifique de skimmings d'un processus de galvanisation par rapport aux skimmings générés par rouleau par temps de séjour de tôle. À la section 3.3, il a été montré que l'utilisation de l'air pour essuyer les tôles d'aciers produit plus de skimmings qu'en essuyant avec de l'azote. Les mêmes résultats ont été obtenus expérimentalement dans la section 3.2. Lorsque les données industrielles pour l'essuyage avec de l'air et de l'azote sont comparé avec des compositions de bain, des vitesses de ligne et des pressions d'essuyage similaires, la ligne de galvanisation en continu d'ArcelorMittal Cleveland produit 9,6% de plus de skimmings par surface de rouleau lorsque l'air a été utilisé. De plus, il a été constaté que la pression d'essuyage était le paramètre dominant qui influençait le montant de skimmings produites par unité de surface de rouleau. En ce qui concerne les données expérimentales, il a été constaté que l'utilisation d'un jet d'air produit 10,5 fois de plus de skimmings par unité de temps par rapport à un jet d'azote. Cela peut potentiellement être expliqué par l'effet stabilisant des films d'oxyde sur la structure mousseux des skimmings. En outre, le taux de génération des skimmings à augmenté avec la vitesse de rotation de l'agitateur et, par conséquent, la surface libre du liquide. Les coefficients de transfert de masse du côté liquide pour le transport d'aluminium et de fer ont été évalués dans la section 3.4. Ces valeurs ont été du même ordre de grandeur que ceux trouvés dans des manuels qui traitent le sujet de transfert de mass entre métal liquide et gaz [30], [31], [32], [33].

Comme le montre le chapitre 1, le skimmings analysés par Thiounn et al. [23] avaient une morphologie similaire par rapport au skimmings industriels examinés dans la section 3.1. Les deux échantillons industriels contiennent des particules de dross, des oxydes et des

porosités. Toutefois, Thiounn et al. n'ont pas fait distinction de la composition variable des éléments chimiques dans leurs échantillons de skimmings. À la section 3.1, nous avons analysé les échantillons polis des skimmings industriels pour leurs distributions élémentaires en utilisant la spectroscopie X à dispersion d'énergie. Cette technique fournit une évaluation de la composition chimique de zones analysées. La série d'images identifie clairement les particules cristallines de $Fe_2Al_5Zn_x$ et de $FeZn_{10}Al_y$ ainsi que les films d'oxyde. Par conséquent, cette technique c'est montré efficace pour identifier les différentes particules intermétalliques présentes dans un bain de galvanisation. Les skimmings produites au laboratoire ont montré des caractéristiques similaires aux skimmings produites dans l'industrie. Les résultats expérimentaux avaient aussi du top et bottom dross, des porosités ainsi que des oxydes de zinc, de l'aluminium et du fer. Par ailleurs, les résultats de laboratoire ont aussi montré des enveloppes d'oxyde clairement définis qui entourent des volumes de zinc liquide. Les skimmings industrielles ne montrent pas des quantités appréciables d'enveloppes d'oxyde. On trouve des films dégénérés qui s'accumulant le long des murs du bain. Les échantillons de laboratoire ont été recueillis sur une courte période de temps. Par conséquent, l'enveloppe d'oxyde dans les échantillons de laboratoire n'a pas eu assez de temps à se transformer. La technique utilisée pour analyser la composition chimique globale des skimmings produites au laboratoire était la spectrophotométrie d'absorption atomique. Du fait que l'aluminium et le fer sont présents dans de telles petites quantités, la précision de la technique peut être imprécise. La teneur en aluminium et en fer des skimmings produites variaient respectivement entre 0,14% à 0,34% en poids et 0,04% à 0,194% en poids. Alors que ceux analysés par Thiounn et al. avaient des niveaux d'aluminium entre 0,4% et 1% en poids et les niveaux de fer entre 0,02% en poids et 1% en poids.

Conclusions

Une analyse statistique des données fournis par ArcelorMittal Cleveland HDGL conduit aux conclusions suivantes:

1. Deux paramètres opérationnels qui influencent le montant de skimmings produites dans le procédé de la galvanisation en continu ont été identifiés: (1) la pression de l'air dans le distributeur des couteaux d'essuyage et (2) la vitesse de la ligne.

La pression d'essuyage a un effet plus important que la vitesse de ligne sur le montant de skimmings produites par unité de surface de tôle traitée.

2. Le type de gaz utilisé pour le système d'essuyage a une influence importante sur la quantité de skimmings produit par unité de surface de rouleau. Essuyant avec de l'air produit plus de skimmings qu'avec de l'azote.

3. L'opération de galvanisation (GI) produit plus de skimmings que l'opération de galvannealing (GA) illustrant l'effet de la composition du bain sur la génération d'écume.

Une étude de la morphologie et de la composition des échantillons fournis par l'écumage industriels d'ArcelorMittal Cleveland et U.S.Steel Hamilton conduit à la conclusion suivante:

4. La spectroscopie X à dispersion d'énergie s'est avéré à être une méthode très efficace pour identifier la composition et la répartition des éléments dans les échantillons de skimmings. Les skimmings consistent un mélange très poreux et hétérogène d'une ou de deux différentes particules intermétalliques de $Fe_2Al_5Zn_x$ et $FeZn_{10}Al_y$ et une agglomération de films d'oxyde de zinc, d'aluminium et de fer dans une matrice de zinc liquide.

Les expériences à l'échelle laboratoire pour simuler la formation de skimmings dans la région de la sortie de la tôle du bain de galvanisation ont donné des résultats importants:

5. L'analyse d'image des échantillons montrent que les skimmings produit à l'échelle laboratoire sont similaires aux échantillons prises sur des lignes de galvanisation à ArcelorMittal Cleveland et d'U.S.Steel Hamilton. Les échantillons consistaient de mélanges hétérogènes de solution de bain, des particules de top et bottom dross et des films d'oxyde de zinc, d'aluminium et de fer.

6. Les expériences ont montré que la production d'écume augmente avec l'agitation du bain. Les alliages GI ont également produit plus de skimmings que les alliages GA. Il y a plus de skimmings formé lorsqu'un jet d'air est utilisé par rapport à un jet d'azote. Le placement d'un couvercle sur le creuset contribue à réduire la quantité de skimmings formées. Cela est particulièrement évident quand on compare les deux cas d'un creuset couvert sous un jet d'azote et un creuset ouvert sous un jet d'air.

Une deuxième série d'expériences à l'échelle laboratoire a été menée pour déterminer le transfert de fer et de l'aluminium dans le zinc et l'atmosphère ambiante près de la région de sortie de tôle d'acier du bain de galvanisation. Cela a été accompli par le bullage de l'air dans un creuset chargé avec l'alliage de zinc liquide:

7. Cette méthode a été utilisée pour évaluer les coefficients de transfert de masse de l'aluminium et de fer produit dans le zinc liquide sur la surface de réaction. Les résultats se comparent favorablement avec ceux trouvés dans la littérature. Il a été démontré que les corrélations obtenues pour calculer des flux de bulles dans l'eau peuvent être aussi appliqués aux métaux liquides.

ABSTRACT

This study examined skimmings formation in the continuous hot-dip galvanizing process. Skimmings are metallic foam that is produced near the strip exit region of the galvanizing bath due to the high degree of mixing and oxidative conditions in this area. Industrial operating data from ArcelorMittal Cleveland's HDGL was examined and it was found that the production of skimmings per coil surface area increased with wiping pressure and line speed but more so with the former. Moreover, galvanizing (GI) baths were found to produce more skimmings per unit time than galvannealing bath (GA) and air wiping produced significantly more skimmings than nitrogen wiping. Dispersive X-ray mapping was found to be a reliable technique for identifying the elemental distribution and morphology of skimmings samples from the galvanizing lines of ArcelorMittal Cleveland and U.S. Steel Hamilton. Two different bench scale experiments were conducted as well. The first attempted to simulate skimmings formation in a galvanizing bath using a shrouded crucible loaded with liquid zinc, a steel impeller for agitation and an impinging jet of gas. The results showed that the rate of skimmings generation increased with impeller rpm. Also, GI alloys and air jetting produced more skimmings per unit time than GA alloys and nitrogen jetting. Finally, shrouding the crucible had an inhibiting effect on skimmings formation especially when comparing the two cases of a shrouded crucible under a nitrogen jet and an open crucible under an air jet. The second experiment attempted to simulate the mass transfer between liquid zinc and air in a galvanizing operation by top submerging a jet of air into a crucible loaded with liquid zinc. The liquid side mass transfer coefficients for aluminum and iron in liquid zinc were evaluated and compared favourably with the literature. Therefore, the assumption that the correlations for bubble flow in water can be applied to liquid metals was satisfactory.

TABLE OF CONTENTS

LIST OF FIGURES

LIST OF TABLES

INTRODUCTION

Since the industrial revolution, zinc has been used to improve the durability and performance of steel. Zinc coatings are valued as they provide an economical way of protecting steel against corrosion which, left unchecked, is estimated to cost an industrialized country's economy at least 4% of GDP each year. Zinc-coated or galvanized steel combines a unique set of properties:

- high strength
- formability
- light weight
- corrosion resistance
- aesthetics
- recyclability
- low cost

Therefore, galvanized steel is ideally used for the manufacture of household appliances and construction materials. However, the most important product in market value is the hot-dipped galvanized or galvannealed sheet destined for auto body manufacture.

Galvanized and galvannealed steel sheets are produced in a complex metallurgical process known as the continuous hot-dip galvanizing process. Steel coils of various widths and thicknesses are unwound and continuously coated by rapid immersion in a zinc alloy bath operating at temperatures normally between 450°C and 480°C. One of the major concerns affecting the coating process is the melt loss. Usable zinc is wasted in the process and forms metallic foam which is periodically skimmed off the surface of the bath as it accumulates along the pot walls. Hence, this waste is known as skimmings and it pollutes the bath surface and impedes on the final product quality.

The work presented here is a comprehensive study of the mechanism of skimmings formation and its characterization. The work is part of a project sponsored by the International Lead and Zinc Research Organization (ILZRO) entitled ZCO-55: "Minimization of skimmings formation

in the galvanizing bath". The general objective of this project consists of a fundamental study of the interaction of the gas jet from the wiping knives on the return flow of the zinc to the bath along the emerging strip. This interaction results in the partial loss of metal from the descending zinc flow which contributes to the skimmings that collects at the bath surface.

Two sponsors of project ZCO-55 accepted to participate in this study; ArcelorMittal Cleveland and U.S. Steel Hamilton. Both sponsors contributed skimmings samples from their respective continuous galvanizing lines in order to investigate their composition and morphology. Furthermore, only ArcelorMittal provided spread sheets of their operating data. The data was recorded at the plant from October 2008 to March 2009 but was not continuous. Pockets of information lasting approximately one to four days at a time were investigated and treated in order to determine which process parameters had the greatest effect on skimmings generation.

Two different bench scale experiments were also conducted as part of satisfying the mandate of the project. The first experiment involved simulating skimmings formation at the strip exit region of a galvanizing bath using a shrouded crucible loaded with liquid zinc, a steel impeller for agitation and an impinging jet of gas. The second experiment involved trying to simulate the mass transfer between the return zinc flow from the wiping knives and the surrounding atmosphere near the strip exit region of a galvanizing bath. This was accomplished by top submerging a jet of air into a crucible loaded with liquid zinc.

CHAPTER 1 LITTERATURE REVIEW

1.1 Overview of zinc coated steel products

There are approximately 550 continuous galvanizing lines worldwide producing almost 100 million tonnes of coated steel [1]. Nearly 75% of all galvanized sheet steel is destined for auto body manufacture and the remaining 25% is used for the construction and domestic appliance industries. There are several zinc coated steel sheet products: Galvanized (GI), Galvanneal (GA), Electrogalvanized, Galvalume® and Galfan®. The combined worldwide production of electrogalvanized, Galvalume and Galfan products pales in comparison to the combined production of galvanized and galvannealed products. A comparative analysis is shown in **Figure 1.1-1** [1].

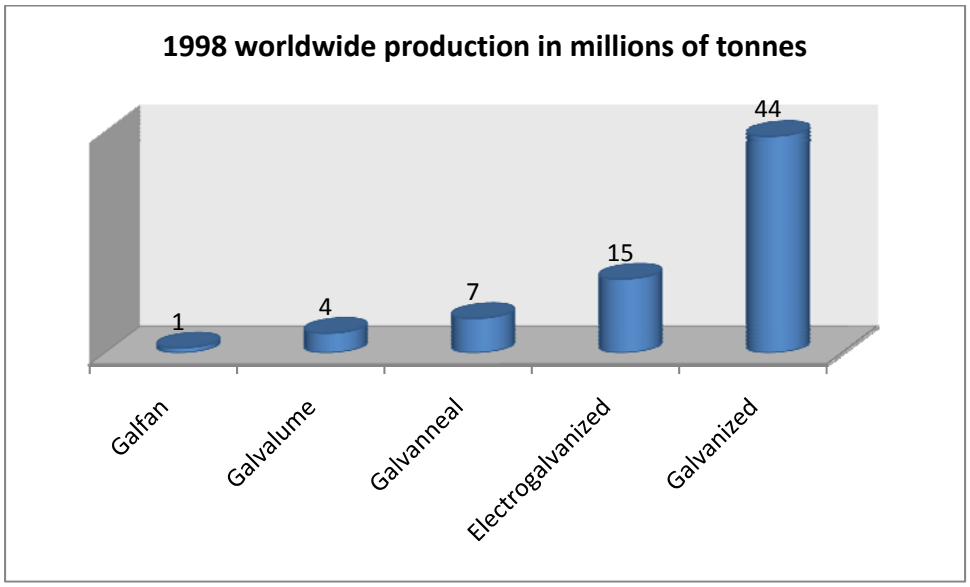

Figure 1.1-1: Continuous zinc coatings and yearly production in millions of tonnes of steel [1]

In 2007 [2] there were 10 continuous galvanizing lines in Canada, 10 in Mexico and 67 in the United States. The total GI and GA output of all 87 continuous galvanizing lines in North America and Mexico was 27.1 million tonnes. Moreover, there are 13 electrogalvanizing lines in

the United States and they have a total output of 3.3 million tonnes. Electrogalvanized products are essentially steel sheets electroplated with pure zinc although Zn-Fe and Zn-Ni alloy coatings are also commercialized. Unfortunately, electrogalvanized steel sheets are expensive to produce and their manufacture is slowly being phased out by the increased usage of galvannealed sheets. Galvalume coatings are 55 wt% Al-Zn alloys and provide excellent corrosion resistance wherever applications with severe forming are absent. Galfan coatings are 5 wt% Al-Zn alloys but unlike Galvalume coatings, they provide exceptional corrosion resistance wherever applications with severe forming are present. The bulk of zinc coated steel production is galvanized sheet which is produced using a liquid zinc bath containing about 0.16 wt% to 0.20 wt% Al. Similarly, galvanneal sheet is produced in the same manner except the zinc bath has an Al content ranging between 0.11 wt% and 0.14 wt% Al. **Table 1** [3] summarizes the applications and key characteristics of each coating type.

Table 1: Common uses and attributes of coated steel sheet [3]

Coating Type	Applications	Key Attributes
Galvanized	Steel framing Heating, ventilation, AC Corrugated culverts Roof and floor decking Pre-painted building panels Agricultural storage bins Auto body inner panels	High formability and durability Large range of coating weights High strength Paintability Cost effective
Electrogalvanized	Auto body outer panels Computer cases	Ultra-smooth surface finish Good weldability
Galvanneal	Auto body outer panels Pre-painted appliance wrappers	Good weldability Good paintability and formability
Galvalume	Bare and painted roofing and siding High temperature applications	Great corrosion performance Good paintability
Galfan	Pre-painted architectural panels Automotive equipment	Great corrosion performance Great formability and Paintability

1.2 Description of the continuous galvanizing process

Continuous hot-dip galvanizing is a process which involves the nonstop application of a molten zinc alloy coating onto the surface of steel sheets. The steel sheet is passed as a continuous ribbon through a bath of molten metal at speeds ranging between 1 m/s to 2 m/s. In the bath, the steel strip reacts with the molten zinc alloy to form a protective coating on the strip surface. The bath operating temperature usually ranges between 450 °C to 480 °C. As the strip emerges from the molten bath, it drags out excess liquid metal along with it. Using a gas-wiping process, the excess liquid dragged up with the steel sheet is pushed back into the molten bath. Moreover, the final coating thickness, also known as the deposition rate, is controlled by the gas-wiping process and is usually expressed as mass of coating per unit area of sheet (g/m^2).

A typical modern day galvanizing line is illustrated in **Figure 1.2-1** [3]. In the entry section, the sheet of cold rolled steel is uncoiled and welded to the tail end of the coil ahead of it in the processing line. Then, in the pre-treatment section, the strip is cleaned by brushing its surface with an alkaline liquid. After, the strip is rinsed and dried.

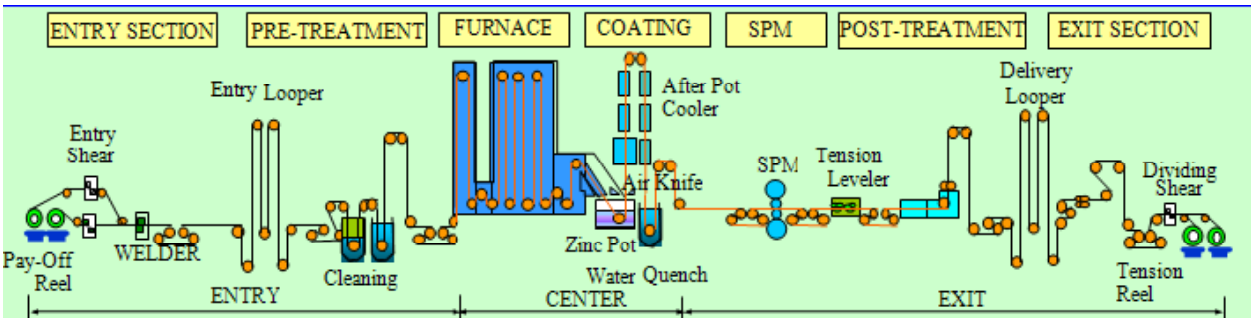

Figure 1.2-1: Typical modern galvanizing line for automotive product (POSCO-MEXICO) [3]

From the cleaning section, the strip enters the central part of the process. First, the strip passes into an annealing furnace where it is softened and the desired strength and formability are imparted to the steel. Furthermore, in the annealing furnace, the strip is maintained under a reducing gas atmosphere to convert any iron oxide to iron on the steel surface. The gas

atmosphere is generally composed of a mixture of 5% hydrogen and 95% nitrogen [4]. This oxide reduction step is vital to promoting the complete wetting of the strip surface during the time it is immersed in the zinc bath. Upon leaving the annealing furnace, the steel strip is normally at 460 °C which is about the same temperature as the molten zinc bath. The exit end of the annealing furnace is connected directly to the bath by a snout. The snout serves to prevent any air from re-oxidizing the heated steel strip before it enters the bath. In the bath, the strip passes around the sink roll and reacts with the molten zinc alloy to form the protective coating. The strip then exits vertically from the bath between two asymmetrically located guide and stabilizing rolls. The bath temperature is maintained by induction heaters which are generally located on both sides of the pot. They provide enough heat to overcome the heat losses at the bath surface and to melt makeup ingots. The pot configuration is shown in detail in **Figure 1.2-2** [5].

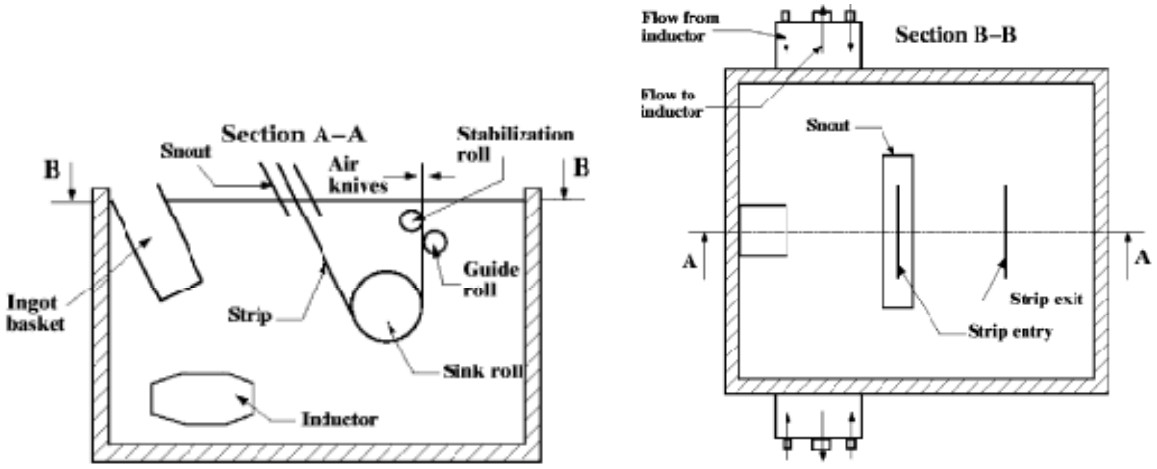

Figure 1.2-2: Schematic of the top and side view of a galvanizing bath with ingot charging [5]

As the strip emerges from the bath, excess liquid zinc is dragged up along with it. The excess zinc is deflected back to the bath by the gas-wiping knives which are located on both sides of the exiting strip. The typical wiping knives configuration is shown in **Figure 1.2-3** [6].

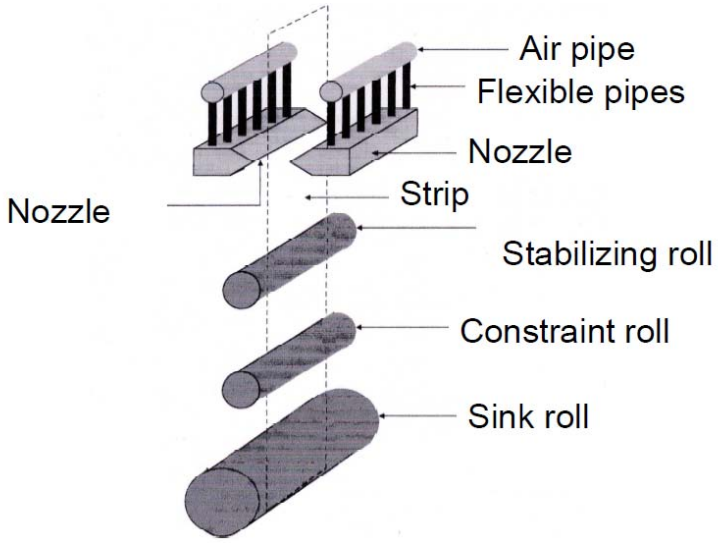

Figure 1.2-3: Typical wiping knives configuration located above the molten zinc pot [6]

The gas-wiping knives, also known as air knives, launch high pressure jets of either air or nitrogen through a narrow slit towards the strip in order to control the coating thickness. The product is then cooled to allow the coating to solidify on the steel surface. To accomplish this, the strip travels along a vertical section above the bath which can be as high as 60 m [4]. After cooling to room temperature, the strip feeds into a temper mill to impart the desired surface finish to the coated steel. Then it travels to the tension leveller which flattens the strip. Finally, the post-treatment section applies a clear water-based treatment and/or oil to assist with preventing degradation of the final coated product. The clear treatment prevents storage stains that can form on the coating surface when moisture is present and the oil serves to inhibit rusting [4]. A recoiler rewinds the finished coil of steel which is then sheared at the weld that was made at the entry end of the line in order to preserve coil-to-coil identity. Not all hot-dip coating lines have all of the above processing steps [4]. For example, some do not include the aqueous cleaning stage, relying instead on “flame” cleaning in the entry end of the annealing furnace. Others might not have a temper mill as it might not be necessary for some applications of hot-dip coated products.

1.3 Difference between galvanizing and galvannealing

The two main differences between galvanneal and galvanize are that galvannealed steel strips pass through zinc alloy baths that are less rich in aluminum and they are heated instead of cooled once they pass the wiping knives. Typically, galvanneal baths have aluminum concentrations ranging between 0.11 wt% to 0.14 wt% while galvanize baths have aluminum concentrations ranging between 16 wt% to 20 wt%. As shown in **Figure 1.3-1** [4], once the steel strip passes the wiping knives, for a galvannealing process, it is heated in a galvanneal furnace to temperatures ranging between 500 °C to 565 °C [4] and held at that temperature for approximately 10 seconds [4]. In both galvanneal and galvanize operations, dissolved aluminum preferentially reacts with the steel to form an inhibition layer of Fe_2Al_5.

Zinc protective coatings vary in thickness from 10 μm to 15 μm and they consist of an inhibition layer with a thickness of about 100 nm covered by a Zn-Al alloy. In the galvanneal process, the reaction continues as the strip passes through the galvanneal furnace to form adherent layers of intermetallic Al-Fe-Zn compounds. The end result is that the coating is converted to layers of intermetallic Zn-Fe compounds. The iron content in the coating varies with its thickness, from as low as ~6 wt% at the surface, to as high as ~23 wt% at the steel interface [4]. The final bulk iron concentration depends mostly on the heating cycle since the rate of diffusion is primarily a function of time and temperature. A galvanize coating is essentially pure zinc containing between 0.20 wt% and 0.50 wt% bulk aluminum [4]. However, the aluminum in the coating is highly concentrated in the thin inhibition layer next to the steel. Cross sections of both galvanized and galvanneal steel sheets are shown in **Figure 1.3-2**.

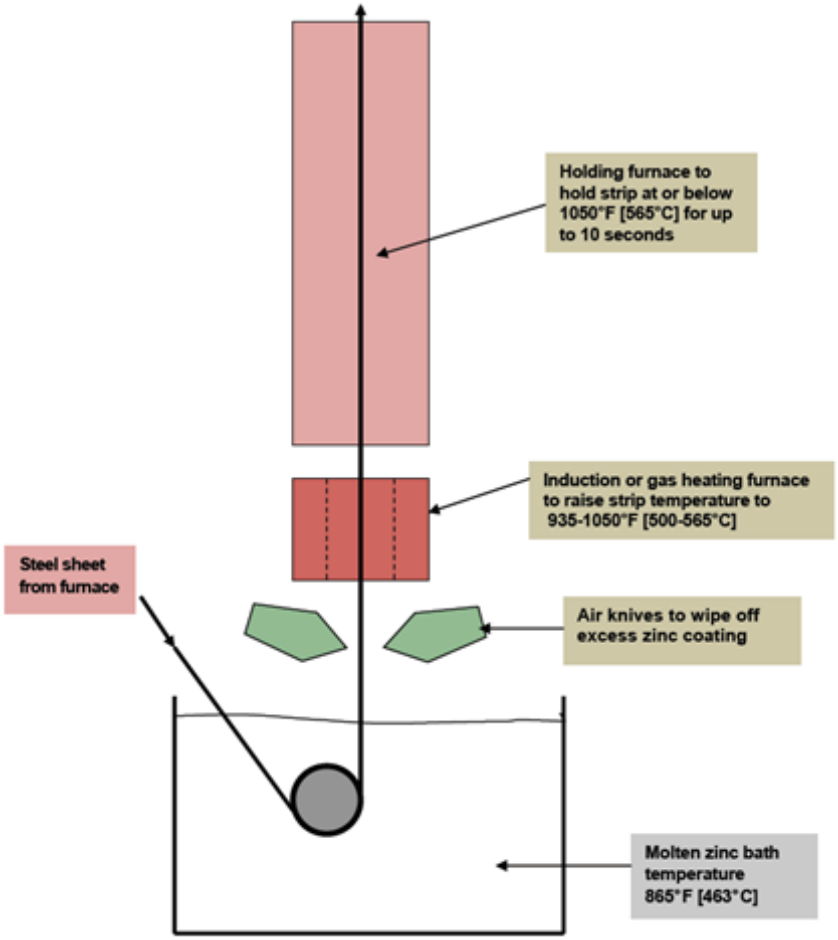

Figure 1.3-1: Schematic of the molten bath, wiping knives and galvannealing furnace [4]

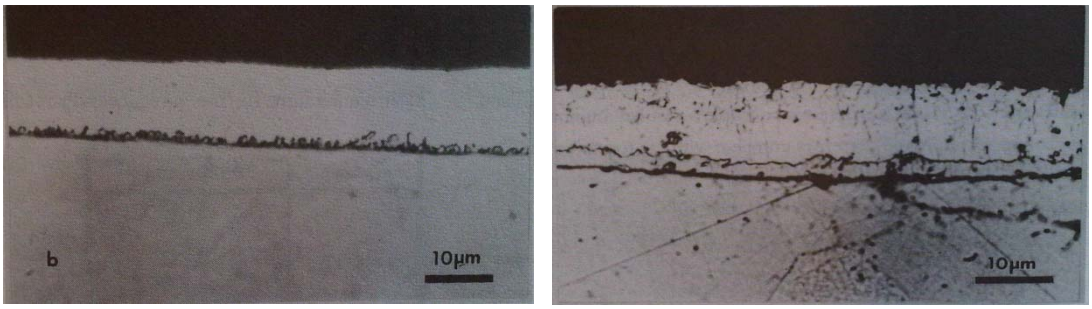

Figure 1.3-2: Cross sections of galvanize (left) and galvanneal (right) steel sheet

Galvanneal coatings typically have 3 distinct Zn-Fe phases. These phases are shown in **Table 2** [4], along with their iron and aluminum contents. The phases in Table 2 are shown in the order that they occur in the coating, with the high-iron Fe_3Zn_{10} (Γ) layer next to the steel substrate.

Table 2: Galvanneal phases and compositions [4]

Alloy Layer	wt% Fe	wt% Al
$FeZn_{13}$ (ζ)	5.2 – 6.1	0.7
$FeZn_{10}$ (δ)	7.0 – 11.5	3.7
Fe_3Zn_{10} (Γ)	15.8 – 27.7	1.4

1.4 Zn-Fe-Al alloys and dross particles

Isolated intermetallic particles form in the bath during continuous hot-dip galvanizing. These intermetallic compounds are also known as dross. Dross normally consists of Al bearing Zn-Fe intermetallics (bottom dross) or Zn bearing Fe-Al intermetallics (top dross). The origin of these particles is a direct consequence of iron being continuously dissolved into solution during hot-dipping. Any iron in excess of the solution's solubility limit is converted into dross particles at the bath/steel interface [8]. Thereafter, dross particles continue to precipitate from the melt during normal operation of the galvanizing line [9, 10, 11].

Top dross, $Fe_2Al_5Zn_x$ (η phase), is primarily formed during GI operation. These particles float to the surface of the bath since the particles are less dense than the zinc solution. Bottom dross, $FeZn_{10}Al_y$ (δ phase), is mainly formed during GA operation. These particles sink to the bottom of the bath since they are denser than the zinc solution. However, it is common to have both η and δ intermetallic particles form during GI operations. **Figure 1.4-1** shows the particles that form in molten Zn-Fe-Al alloys found in typical galvanizing baths.

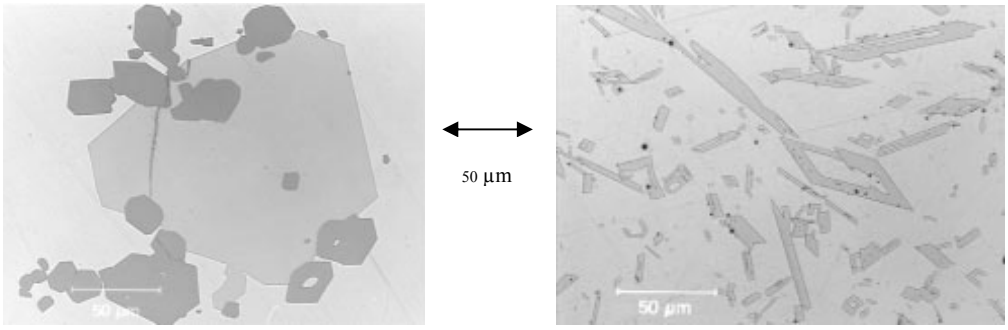

Figure 1.4-1: Typical intermetallic particles formed in molten Zn-Al-Fe alloys. Coexistent δ and η particles (left); η is darker. Collection of ζ particles (right) [12]

Continuous hot-dip galvanizing is rarely, if ever, an equilibrium process. Constant fluctuations in temperature, aluminum and iron levels in different discrete regions of the bath prevent the hot-dipping solution from attaining chemical equilibrium. Nevertheless, Zn-Fe-Al equilibrium phase diagrams have been developed in order to better understand the conditions, albeit at equilibrium, at which top and bottom dross particles form. An optimized ternary phase diagram is shown is shown in **Figure 1.4-2** [13]; however, it is the Zn-rich corner of the diagram, shown in **Figure 1.4-3** [14], which defines the equilibrium solubility of Fe and Al in liquid Zn that most closely represents the actual galvanizing process. Therefore, for a galvanizing bath that has achieved chemical equilibrium at 460 °C, the η, δ and liquid phases would all coexist at an aluminum level of approximately 0.135 wt%. Below this aluminum concentration, the δ phase precipitates out of solution. The η phase precipitates from solution when the bath operates at an aluminum concentration above 0.135 wt%.

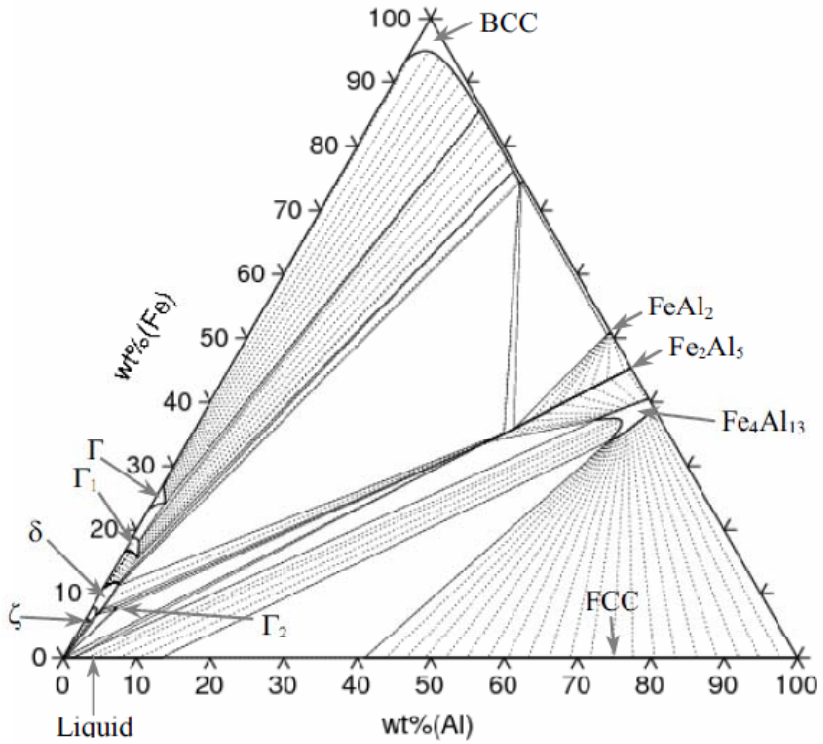

Figure 1.4-2: Isothermal section of the Zn-Fe-Al system at 450°C [13]

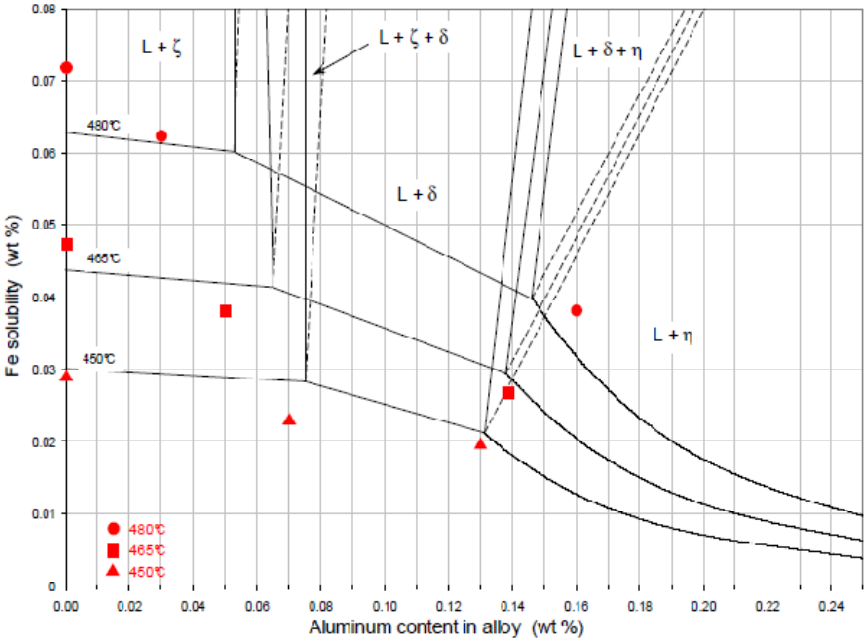

Figure 1.4-3: Zinc rich corner of the Zn-Fe-Al system [14] with experimental data points [15]

1.5 Galvanizing bath fluid flow

A comprehensive study for a fluid flow model for continuous galvanizing was first reported in 1992 [16]. A half scale water model of a typical industrial bath was constructed of Plexiglas with a circulating rubber belt to simulate the movement of the steel strip. Flow patterns within the bath were observed by tracking the movement of polymeric particles with a video camera. The analysis of the filmed results produced the general flow pattern seen in **Figure 1.5-1** [16].

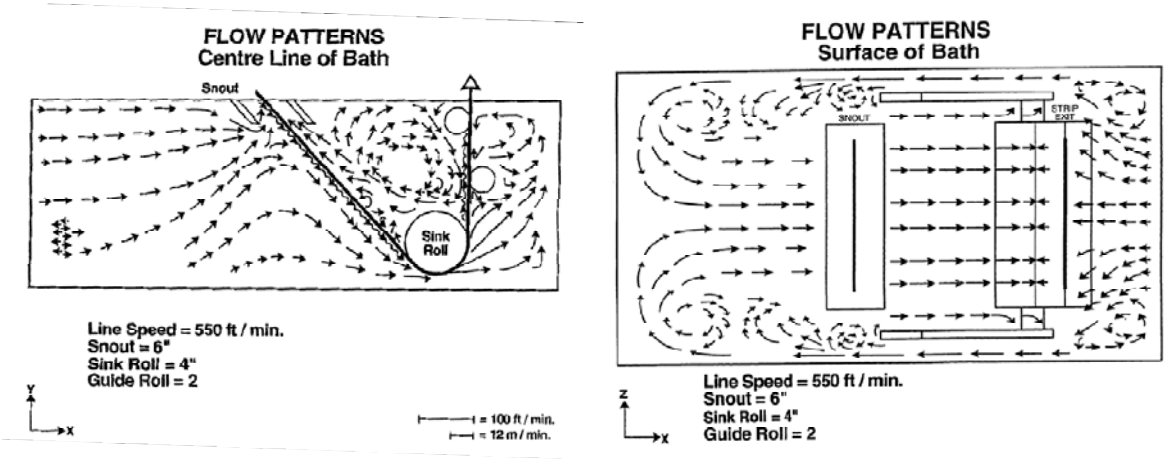

Figure 1.5-1: Experimentally determined velocity profiles using 1/2 scale water model [16]

Moreover, in the same study [16], the authors attempted to mathematically model the flow field inside the water bath. As a first attempt, they used the Navier-Stokes and continuity equations. They assumed steady isothermal incompressible laminar flow and took into account only viscous, pressure and gravity forces. Finally, the physical properties of the fluid were specified using the Boussinesq approximation. The authors concluded that the measurements of the velocities in the water bath were in good agreement with the calculated values from the mathematical model. Models which numerically simulate flow in a galvanizing bath have since become progressively more complex. A solution for turbulent flow in a thermal field was presented in 2001 [17] and the case of turbulent flow in a thermal and concentration field was published in 2004 [18, 19]. It was shown that compared to the isothermal condition, the temperature gradients in the bath during ingot melting had a significant effect on the flow due to the buoyancy of the fluid. The amount of

this variation is due to the effect of temperature and concentration on the density of the bath fluid. The results from the 2004 study are presented below. **Figure 1.5-2** [18] shows the calculated velocity vectors in a plane parallel to the symmetry plane with and without ingot melting.

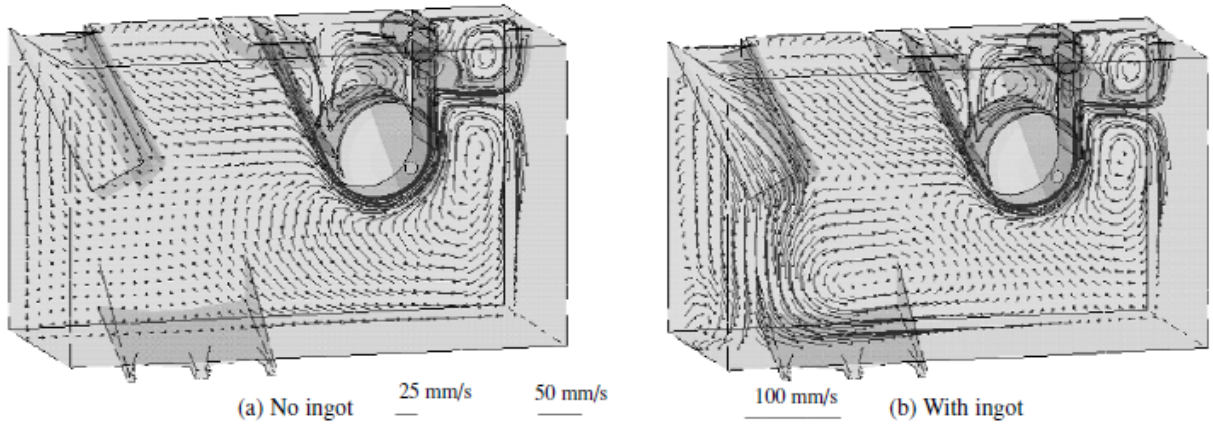

Figure 1.5-2: Velocity profile along the symmetry plane: with (left) and without (right) ingot [18]

Figure 1.5-3 [19] shows the temperature profile along the symmetry plane. With the ingot present, the cold zinc melting from the ingot flows to the bottom of the bath.

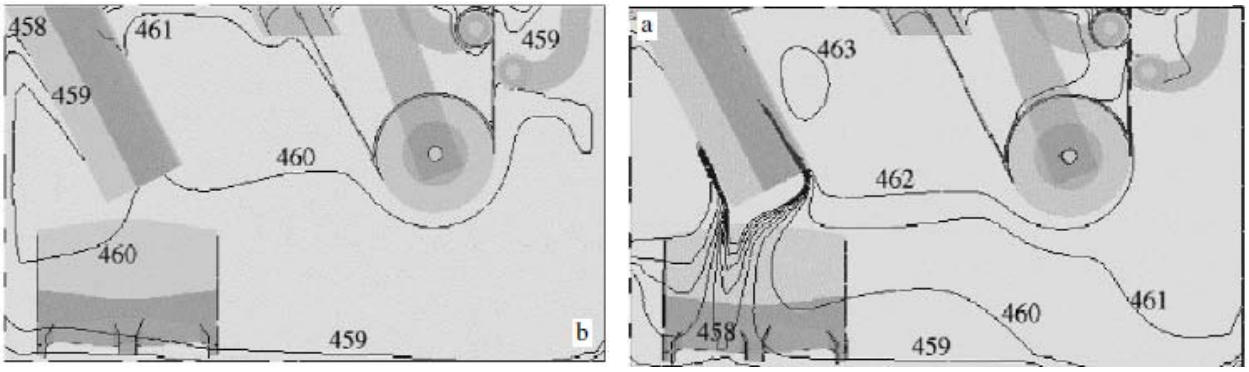

Figure 1.5-3: Temperature distribution along the symmetry plane: (left) with ingot (t = 10 minutes) and (right) no ingot (t = 60 minutes) [19]

Figure 1.5-4 [19] illustrates the distribution of aluminum concentration on the symmetry plane. With the ingot present, we observe a higher level of aluminum near the melting ingot. When no ingot is present, the bath aluminum concentration is relatively uniform throughout the bath.

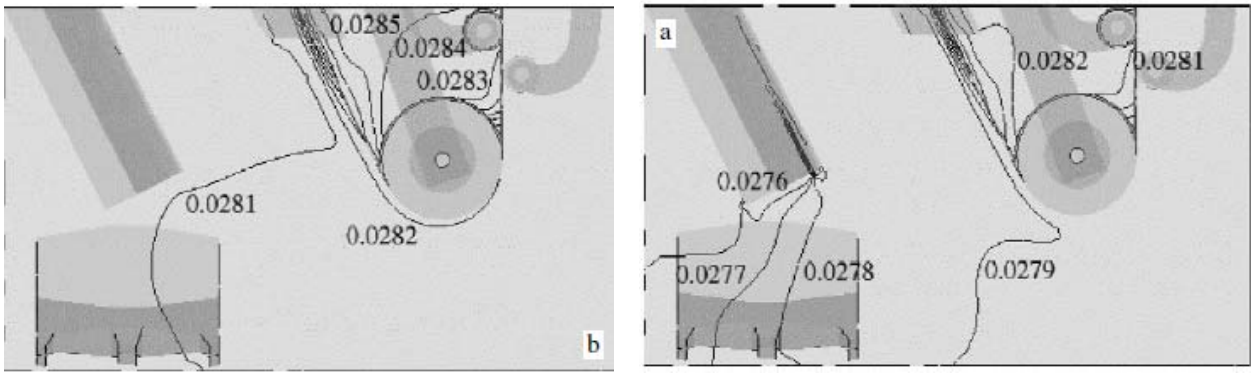

Figure 1.5-4: Aluminum concentration on the symmetry plane: (left) no ingot (t = 20 minutes) and (right) with ingot (t = 60 minutes) [19]

Similar results are shown in **Figure 1.5-5** [19] for the iron concentration. The region below the melting ingot has a lower iron concentration because the ingot has no iron. When the ingot is absent, the bath iron content is relatively uniform.

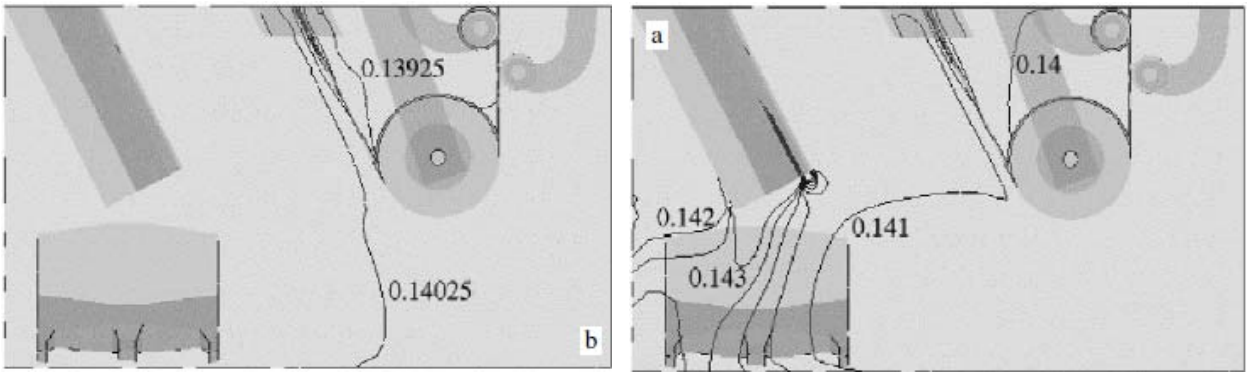

Figure 1.5-5: Iron concentration on the symmetry plane: (left) no ingot (t = 20 minutes) and (right) with ingot (t = 60 minutes) [19]

Even though the numerical simulation takes into account the variation in boundary conditions, solubility limit and changes in physical properties such as the buoyancy effect, validation of the numerical model is difficult to carry out in an industrial bath. Therefore, a 1/5 scale water model shown in **Figure 1.5-6** was also used to validate the numerical simulation in a galvanizing bath for isothermal and non isothermal conditions [20]. Experiments were conducted to measure the variation of temperature as a function of time for the case of cold ingot immersion. Turbulent flow was quantified using a Particle Image Velocimetry (PIV) system and the transient temperature within the bath was measured over a period of time. The experimental set up is also shown in **Figure 1.5-6**. The PIV system consists of a computer coupled to a camera that focuses on the bath that is illuminated by a laser light. Glass beads 10 μm in diameter were added to the water to visualize the fluid movement. Time increments between images were set to monitor the displacement and the turbulence of the liquid. The variation of temperature with respect to time was monitored at about 20 locations in the bath. The comparison of the velocity field in the vertical symmetry plane is shown in **Figure 1.5-7**. It was confirmed that the flow patterns calculated numerically compare very favourably with the PIV measurements.

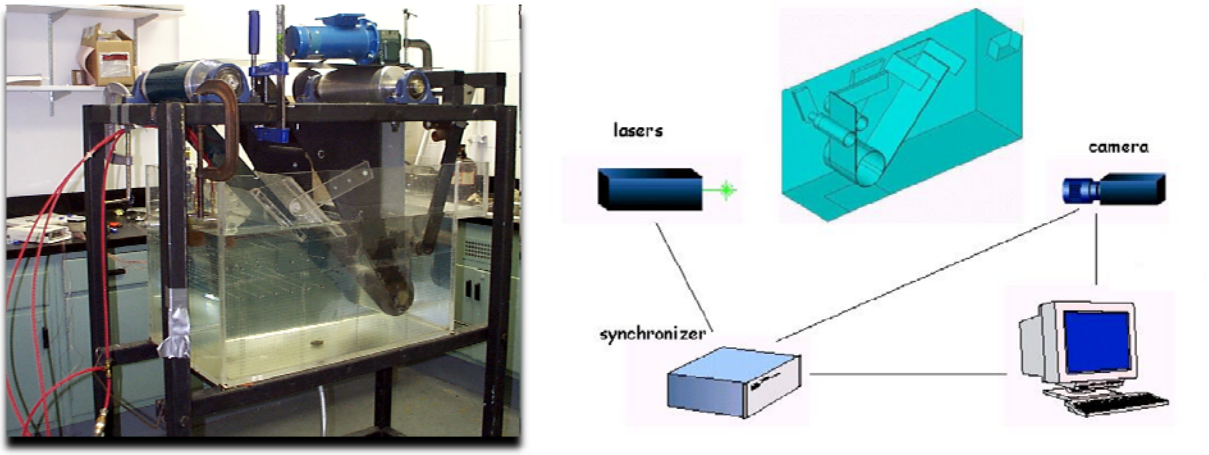

Figure 1.5-6: (left) Photograph of 1/5 scale water model and (right) Set-up of PIV system for monitoring fluid velocity in model bath [20]

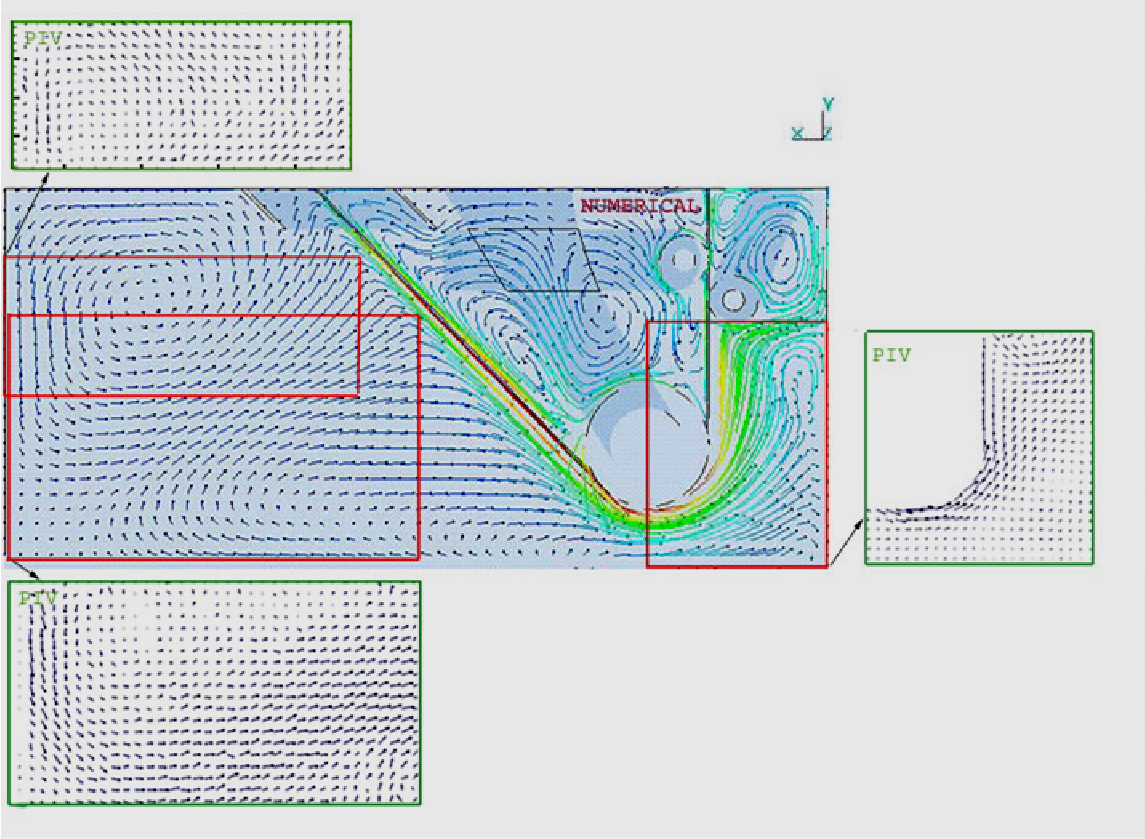

Figure 1.5-7: Comparison of the numerical simulation and PIV measurements from the water bath [20]

With the development of technology such as Laser Breakdown Induced Spectroscopy (LIBS), the continuous monitoring of Al and Fe in a galvanizing bath can be achieved. And in 2005 [21], a more precise validation study of the numerical simulation of the transient temperature and concentration distributions in the Serevco galvanizing bath was conducted. LIBS [22] is an analytical technique for the continuous element analysis of liquids, solids and gases. A high power pulsed laser vaporizes and ionizes a small volume (10^{-8} cm^3 – 10^{-6} cm^3) of material to produce plasma. The optical emission from this plasma is representative of the material ablated and is spectrally analyzed to obtain its atomic composition. The temperature, Al and Fe content of the Serevco bath was measured in time with both the Teck Cominco and LIBS monitoring systems. Data recording lasted 36 hours and covered the entire transition of a GA to a GI bath.

Figure 1.5-8, Figure 1.5-9 and **Figure 1.5-10** show the excellent agreement between the numerical solution of the flow model and the experimental data [21].

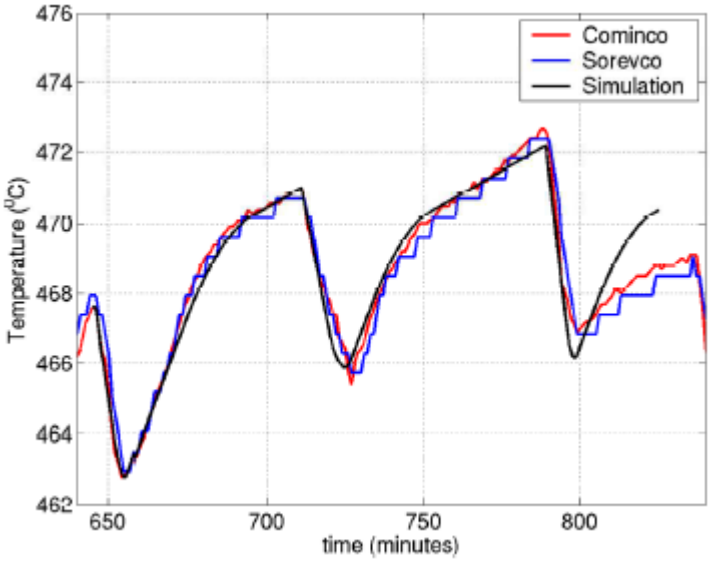

Figure 1.5-8: Comparing simulated and measured temperatures using two thermocouples [21]

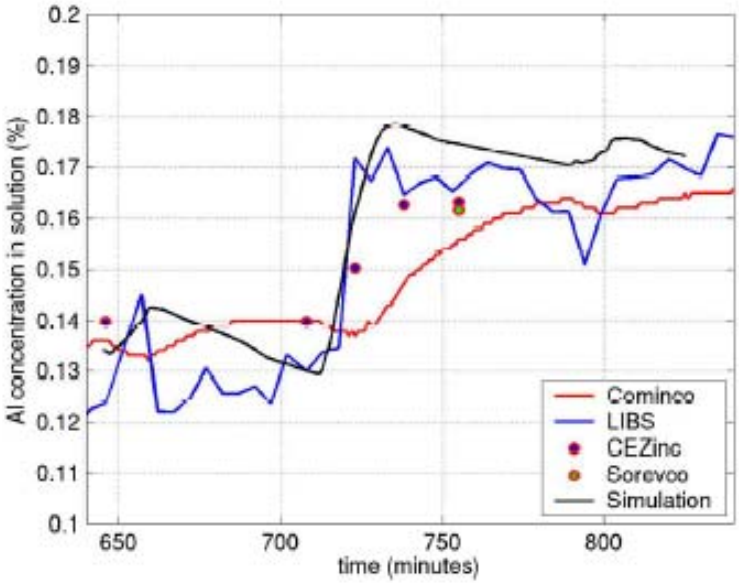

Figure 1.5-9: Comparing simulated and measured Al concentration [21]

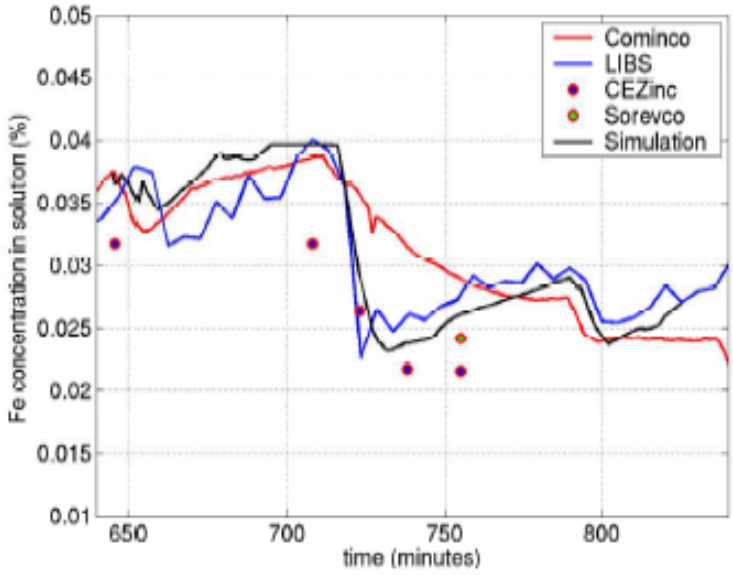

Figure 1.5-10: Comparing simulated and measured Fe concentration [21]

Figure 1.5-11 [21] illustrates the temperature distribution simulated by the numerical solution of the flow model before, during and after ingot melting. The temperature decreases during ingot melting and lower temperatures are observed around the ingot, at the bottom of the bath, on the ingot side and near the top surface in the strip exit region.

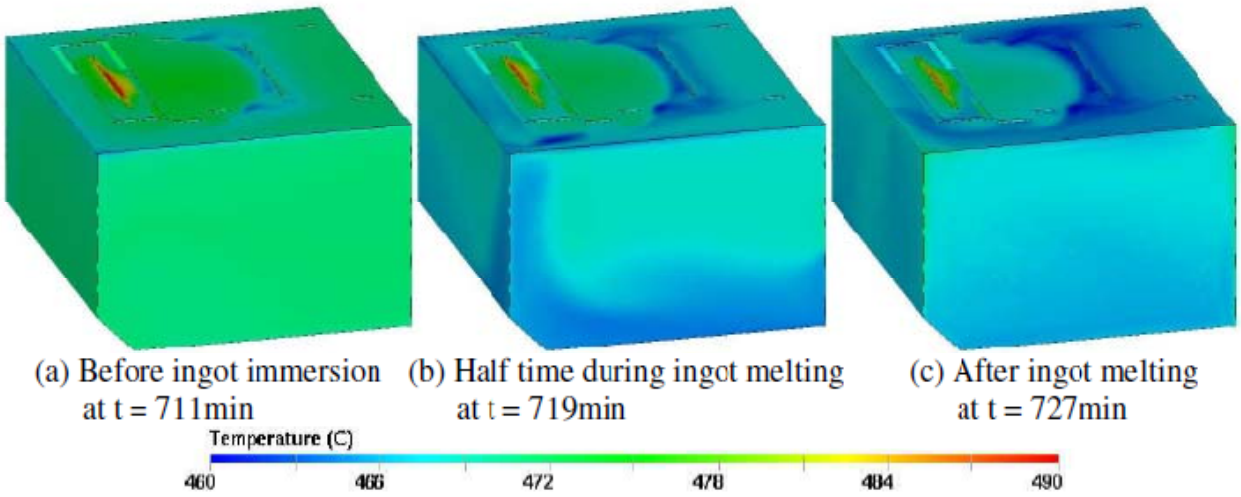

Figure 1.5-11: Temperature distribution during ingot melting at the Serevco galvanizing line [21]

Figure 1.5-12 [21] and **Figure 1.5-13** [21] show the Al and Fe distributions in the bath predicted by the model. These pictures provide valuable information concerning the amount of solutes in solution and the precipitation of dross particles during ingot melting which would otherwise be impossible to see. In **Figure 1.5-12**, the Al distribution in the bath as a total, in solution and in precipitated form are shown before, during and after the blue ingot (4.5 wt% Al-Zn) melting period. During ingot melting, the model showed a significant increase of total Al in the bath with higher Al concentrations near the lower part of the bath at the ingot side. In this region, the Al in precipitated form also increased significantly. Also, we can observe that the regions with lower Al content are located around the entry of the strip and top of the sink roll because Al is being consumed to form the inhibition layer. In **Figure 1.5-13**, the Fe distribution in the bath as a total, in solution, and in precipitated form are shown before, during and after blue ingot immersion. The total Fe concentration decreases slightly during ingot melting periods whereas the precipitated Fe increases especially near the lower region of the bath at the ingot side. In this region, the Fe in solution decreases significantly as expected. Therefore, the numerical model predicts the sharp decrease of Fe in solution when the ingot is immersed. This is explained by the precipitation of dross particles as a result of a significant increase in Al in the bath and a decrease in the temperature. Moreover, the model also predicts that the quantity of Fe in solution increases

during the periods where no ingot is melting. This is caused by the dissolution of dross particles as a result of higher temperature and lower total Al in the bath.

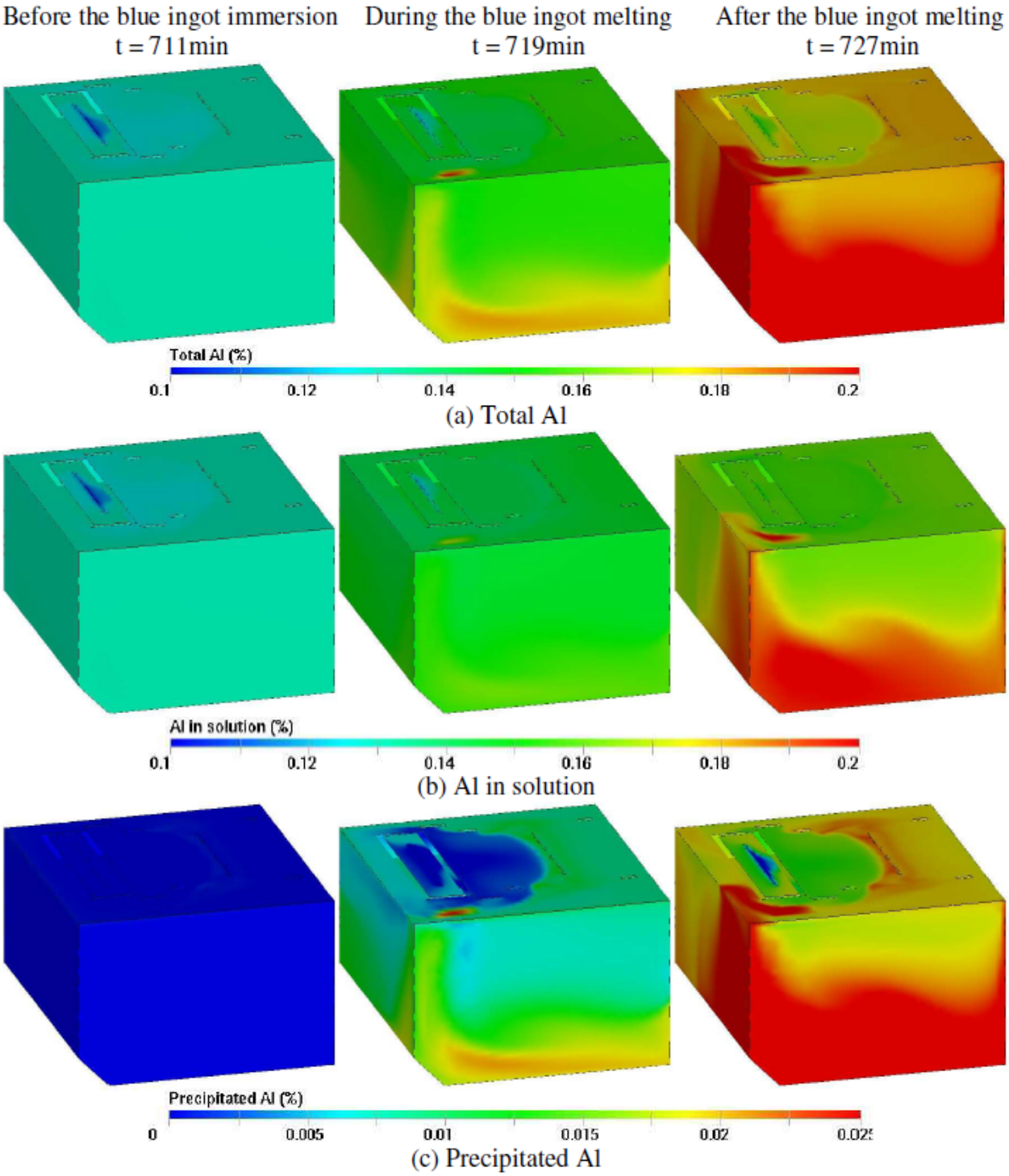

Figure 1.5-12: Mathematical model predictions of Al distribution during ingot melting [21]

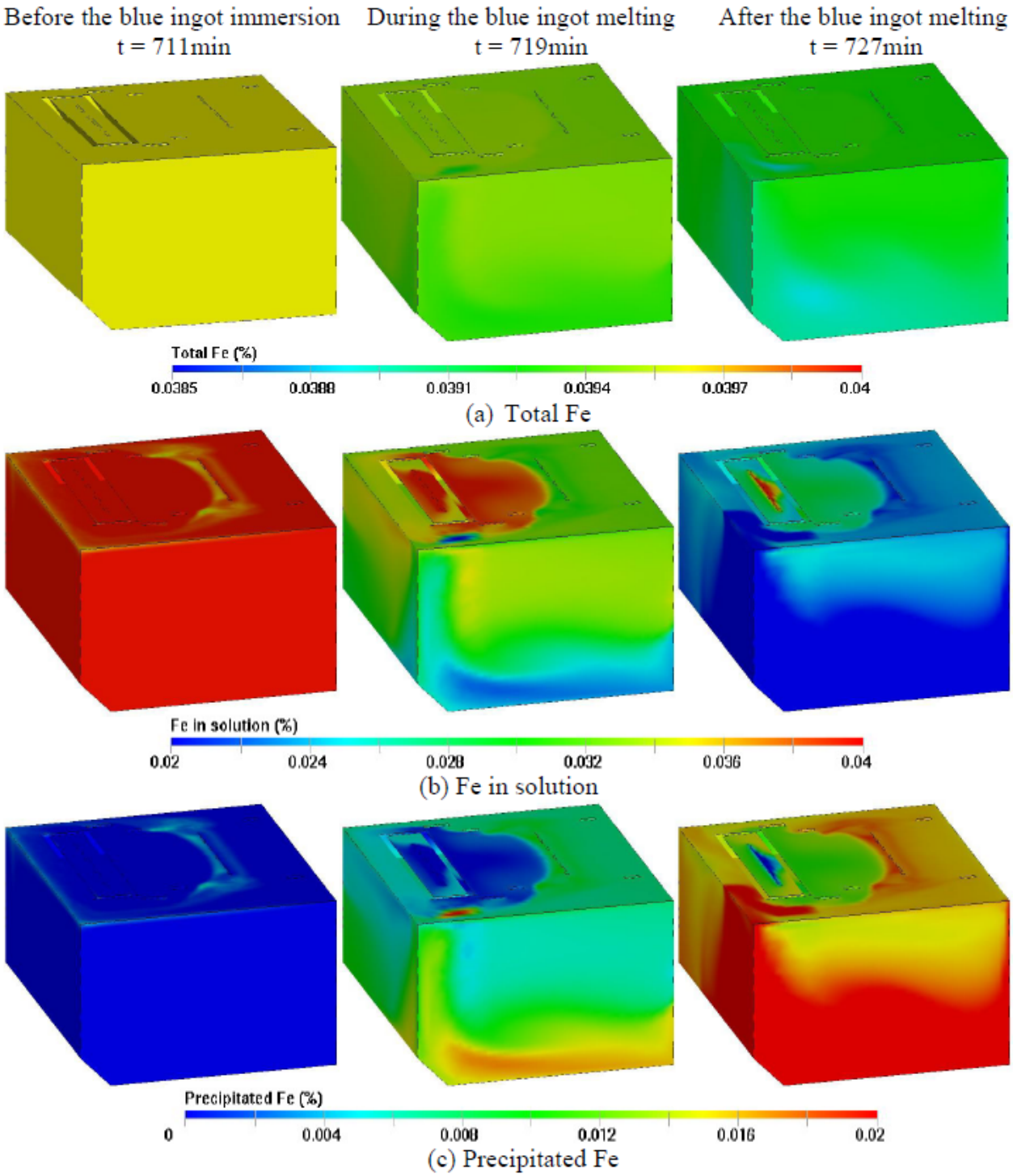

Figure 1.5-13: Mathematical model predictions of Fe distribution during ingot melting [21]

1.6 Bath pollution: scum and skimmings

For all continuous hot-dip galvanizing lines, a portion of the excess zinc which is deflected back into the bath by the wiping knives is wasted. This waste remains afloat and pollutes the bath surface, it is known as skimmings since it is manually or robotically skimmed off the surface of the bath as it builds up along the pot walls. Skimmings production is shown in more detail in **Figure 1.6-1** [23].

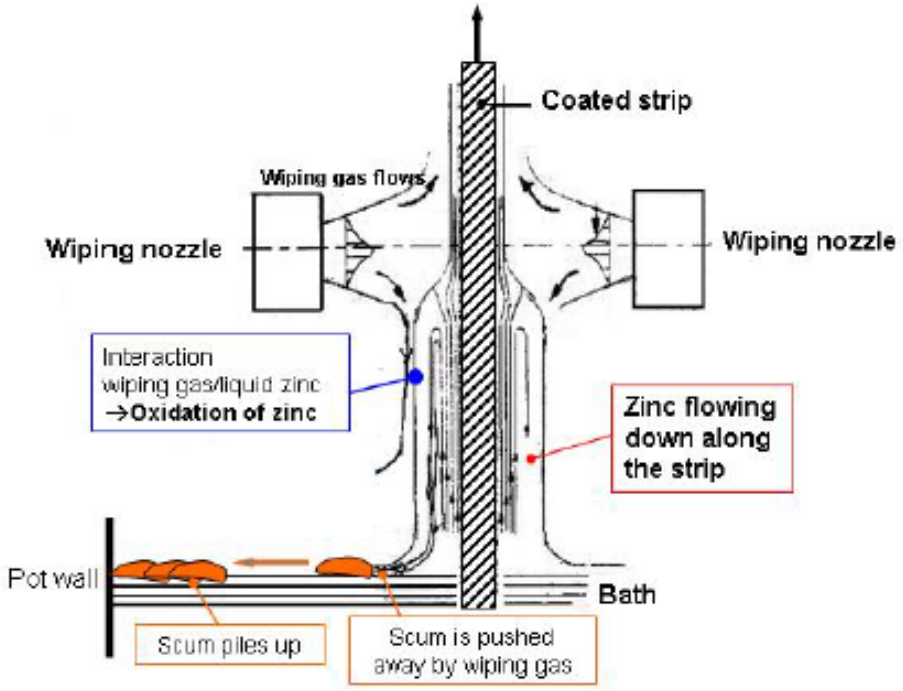

Figure 1.6-1: Scum build up along galvanizing pot walls [23]

In general, as seen in **Figure 1.6-2** [23] skimming are a porous mixture of bath liquid, oxides and dross particles. The intense bath mixing at the strip exit region blends these components together to form metallic foam on the bath surface. The turbulent flow at the strip exit region of the bath is shown in **Figure 1.6-3** [23]. Top and bottom dross particles continuously circulate inside the bath as steel is fed through it. But top dross ($Fe_2Al_5Zn_x$) has a tendency to float to the surface and remain there while bottom dross ($FeZn_{10}Al_y$) tends to sink and accumulate in the pot dead zones.

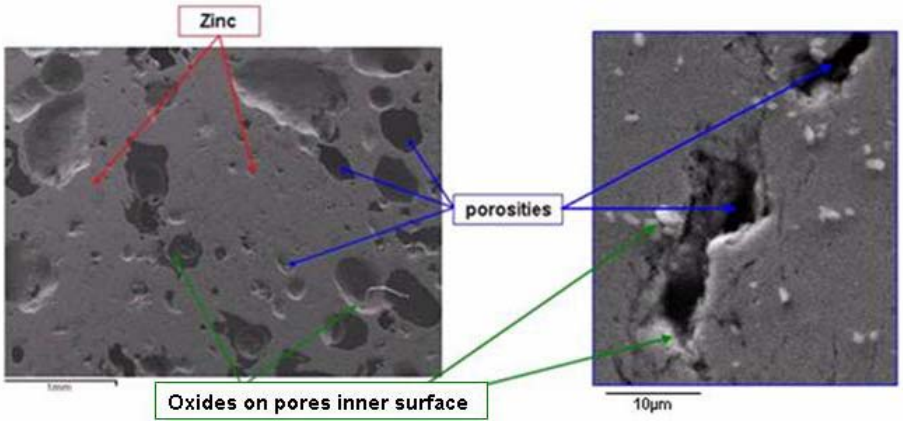

Figure 1.6-2: Cross sectional electron micrograph of an industrial skimmings sample [23]

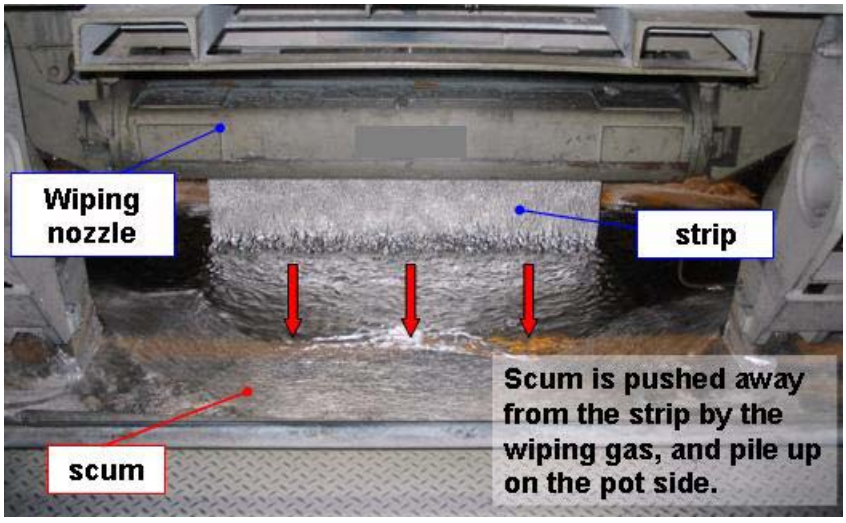

Figure 1.6-3: Turbulent flow regime near the strip exit [23]

Oxides of zinc, aluminum and iron form wherever the bath liquid is exposed to air. However, it is clear that most of the oxidized metal is produced by the wiping knives especially when the wiping gas is air. A detailed flow profile of the liquid zinc flow near the wiping knives is shown in **Figure 1.6-4** [24].

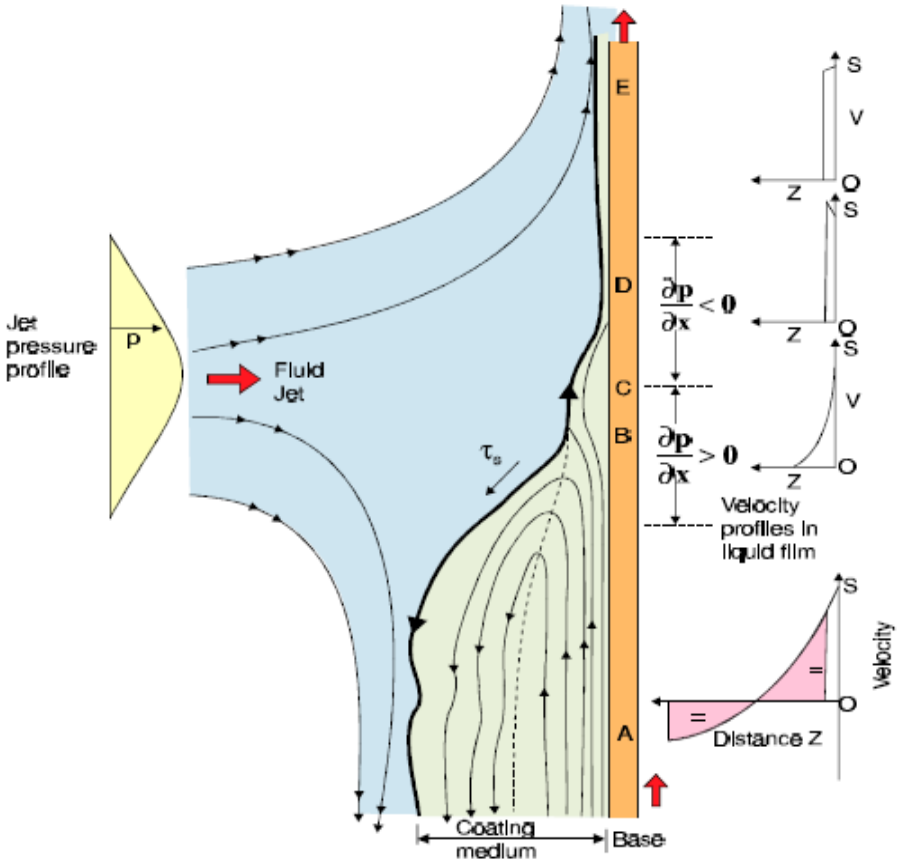

Figure 1.6-4: Detailed flow profile of liquid zinc near the wiping knives [24]

Galvanizers tend to us terms such as skimmings and scum to differentiate between high and low porosity metallic foam that floats on the bath surface. Scum is essential the freshly formed metallic foam that is found near the strip exit region of the bath surface. The wiping gas and the return zinc flow push the scum towards the bath edges. As the scum travels, it sweeps away the oxide layer on the bath surface along with some liquid zinc as well. It then piles up along the bath walls and further oxidizes to form skimmings. Industrial results have previously shown that scum is less porous then skimmings and that the porosities found in scum are smaller than those found in skimmings. This can be seen in **Figures 1.6-5** [23] and **1.6-6** [23].

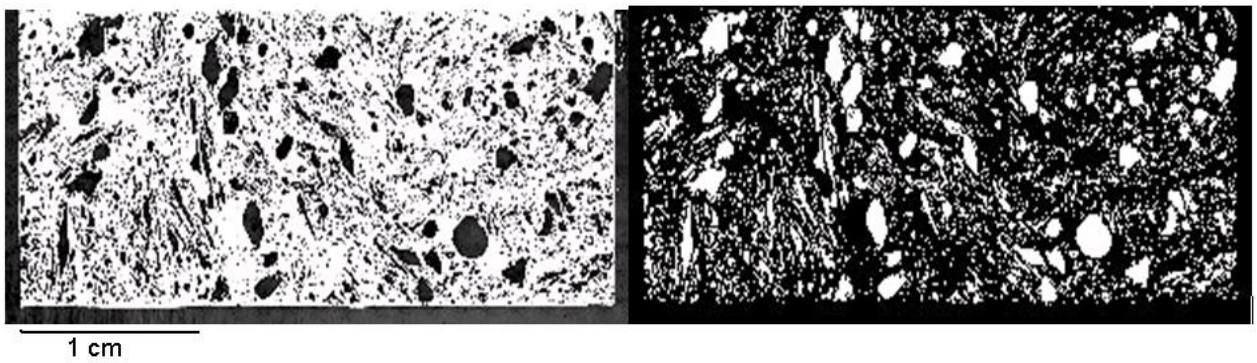

Figure 1.6-5: Cross section of scum sample. Microscope image (left) and black and white treatment (right); porosities are in white [23]

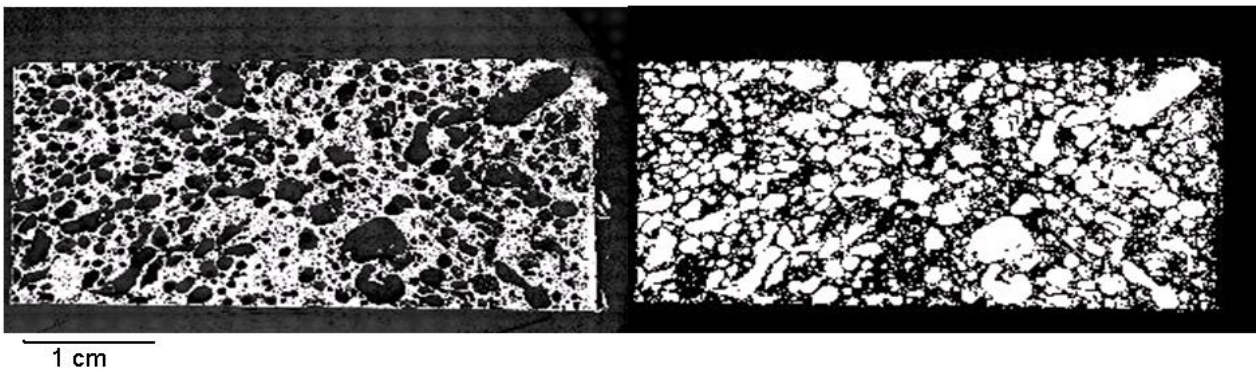

Figure 1.6-6: Cross section of skimmings sample. Microscope image (left) and black and white treatment (right); porosities are in white [23]

Statistical analyses of process parameters have shown that the wiping pressure, wiping knife height, line speed and strip width all have the greatest impact on skimmings formation [23]. It is important to note that process parameters such as the bath temperature, strip entry temperature and bath chemical composition have a greater effect on dross formation than skimmings formation. Therefore, the fluid dynamics of the liquid zinc at the strip exit region is of critical importance in understanding the mechanism of the air-zinc interaction which is the source of skimmings and scum formation.

1.7 Bubble-metal interaction

The oxidation of bath liquid observed in continuous galvanizing does not take place in a closed thermodynamic system. Moreover, as mentioned before, it is difficult to achieve chemical equilibrium in an industrial galvanizing bath. Therefore, it is reasonable to assume that the oxidation of liquid zinc alloy will not produce an equilibrium mixture of complex slags of O, Zn, Fe and Al. Instead, this work assumes that the formation of oxides is driven by the following one-way chemical reactions:

$$Zn_{(l)} + {}^{1}/_{2}\, O_{2_{(g)}} \rightarrow ZnO_{(s)}$$

$$2Al_{(l)} + {}^{3}/_{2}\, O_{2_{(g)}} \rightarrow Al_2O_{3_{(s)}}$$

$$2Fe_{(l)} + {}^{3}/_{2}\, O_{2_{(g)}} \rightarrow Fe_2O_{3_{(s)}}$$

The present work attempts to simulate the oxidation in continuous galvanizing by bubbling air through a liquid zinc alloy solution. In metallurgical processes, bubbles bring about mass transfer by either giving or taking some element to or from the melt. Generally, these reactions take place in the metallic phase. There is considerable literature on the behaviour and reaction of bubbles in liquids at room temperature. However, literature on high temperature liquid metals is very limited. This is attributed to the fact that metallic solutions are opaque and make visual examination of the bubbles impossible. Moreover, difficulties with high temperature experimentation also impedes on any progress concerning bubble-metal interactions. Of particular importance to the author is the estimation of bubble size and shape for a given orifice diameter and flow rate and the experimental determination of mass transfer coefficients for interactions between bubbles and liquid metals. Some researchers have shown that the behaviour of gas bubbles in liquid metals is similar to that of the bubbles in low temperature liquids under certain conditions [25, 26] such as low bubble velocities, small bubble sizes and a laminar flow regime of the liquid phase. The correlations used to estimate bubble size and velocity will be presented below.

1.8 Bubble size

Leibson *et al*. [27] studied the mechanics of bubble formation in the air-water system and showed that the bubble diameter was heavily influenced by the orifice diameter and Reynolds number. The orifice Reynolds number is given by:

$$Re_o = \frac{d_o \, v_g \, \rho_g}{\mu_g}$$

Where d_o is the orifice diameter, v_g is the average gas velocity at the orifice and ρ_g and μ_g are, respectively, the gas density and viscosity. In the laminar flow regime, $Re_o \leq 2000$, uniformly sized bubbles are formed at the orifice and, if large enough, may coalesce or shatter into bigger or smaller bubbles some distance away. In the turbulent flow regime, $Re_o \geq 10000$, large irregular bubbles are formed at the orifice and they explode some distance away into smaller members to form a characteristic jet cone. The bubble diameter for each flow regime is given by:

$$Laminar\ flow: d_b = 0.287\ d_o^{1/2}\ Re_o^{1/3}$$

$$Turbulent\ flow: d_b = 0.71\ Re_o^{-1/20}$$

Where d_b is the bubble diameter and along with d_o is expressed in centimetres. These empirical equations indicate that the bubble size is only a function of the physical system. Therefore, it appears reasonable to directly apply these air-water formulae to gas-metal systems.

1.9 Bubble velocity

Very small spherical bubbles, rising in liquids containing surface active agents, do not exhibit internal circulation. Internal circulation ceases as the surface active agents form an immobile film

on the bubble surface. Hence, the bubbles behave as rigid spheres and their terminal velocity is given by Stokes' Law:

$$U_\infty = \frac{2}{9} \frac{g\, r_b^2 \left(\rho_l - \rho_g\right)}{\mu_l}$$

Where U_∞ is the bubble terminal velocity, g is gravity, r_b is the bubble radius, ρ_l and μ_l are, respectively, the liquid density and viscosity and ρ_g is the gas density. This expression is valid for systems where steady creeping flow around the bubble can be assumed. The author believes that the bubbles issued from the orifice will not be very small i.e. millimetre scale or less. Moreover, assuming steady creeping flow is a poor description of the process in question. Therefore, this classic expression was deemed inadequate for the present work. As bubbles increase in size their spherical shape becomes distorted and surface active agents can no longer halt internal circulation. Assuming the shape of the bubble resembles to a spherical cap, Davies and Taylor [28] have shown that potential flow can be assumed around the bubble. Based on those results, Collins [29] had developed an expression for the terminal velocity of a rising bubble:

$$U_\infty = \frac{1}{2} \sqrt{g\, r_b}$$

1.10 Gas-liquid mass transfer

Mass transfer between the bubble and the surrounding liquid was modelled using the Lewis-Whitman two-film theory. This model proposes that the rate of solute transfer happens across two stagnant films that are adjacent to a common interface. A physical representation of the model is shown in **Figure 1.10-1**.

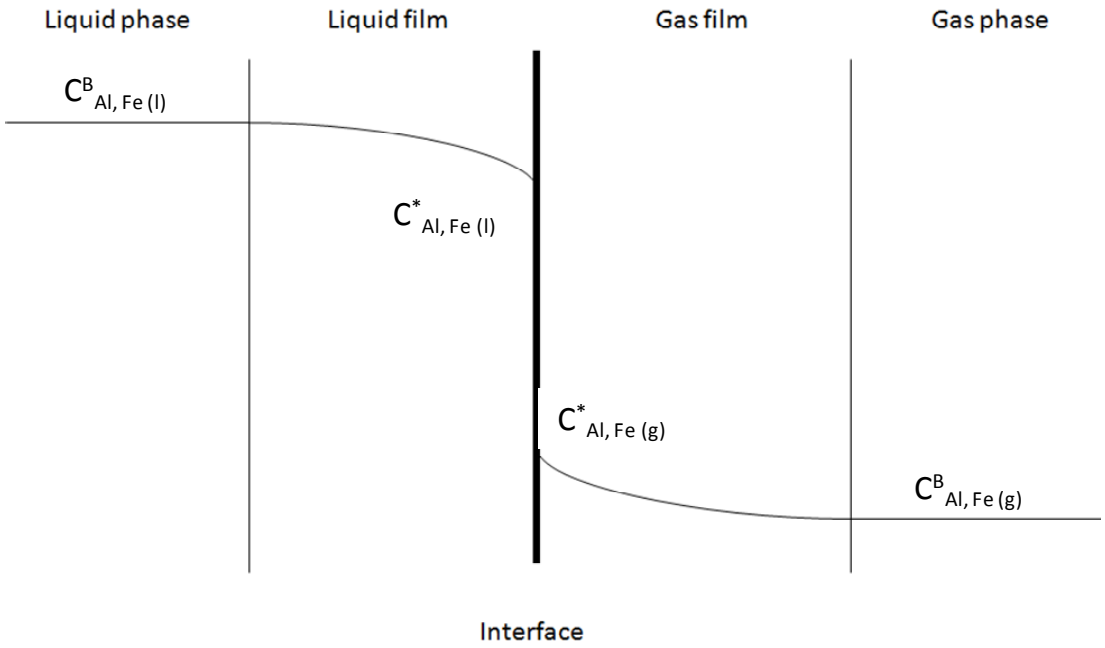

Figure 1.10-1: Concentration profiles for Fe and Al transferring between liquid metal and gas

The model assumes chemical equilibrium at the interface and steady-state diffusion across the two stagnant films. For the present work, the solvent is zinc and the solutes of interest are aluminum and iron. Therefore, from the two film model, assuming both gas and liquid phases are well mixed then the fluxes of aluminum and iron in the liquid film can be written as:

$$N_{Al} = \frac{C^B_{Al,l} - m_{Al}C^B_{Al,g}}{1/k_{Al,l} + m_{Al}/k_{Al,g}}, \; m_{Al} = \frac{C^*_{Al,l}}{C^*_{Al,g}}$$

$$N_{Fe} = \frac{C^B_{Fe,l} - m_{Fe}C^B_{Fe,g}}{1/k_{Fe,l} + m_{Fe}/k_{Fe,g}}, \; m_{Fe} = \frac{C^*_{Fe,l}}{C^*_{Fe,g}}$$

Where N_{Al} and N_{Fe} are the fluxes of aluminum and iron, $C^B_{Al,l}$, $C^B_{Al,g}$, $C^B_{Fe,l}$, $C^B_{Fe,g}$ are the bulk aluminum and iron concentrations in the liquid and gas phases, $C^*_{Al,l}$, $C^*_{Al,g}$, $C^*_{Fe,l}$, $C^*_{Fe,g}$ are the interfacial concentrations of aluminum and iron on the liquid and gas sides on the interface and $k_{Al,l}$, $k_{Al,g}$, $k_{Fe,l}$, $k_{Fe,g}$ are the mass transfer coefficients for aluminum and iron across both the liquid

and gas films. Furthermore, it is reasonable to say that both aluminum and iron immediately react with oxygen once they diffuse to the liquid side of the interface. Then, it follows that $C^*_{Al,l} = C^*_{Fe,l} \approx 0$. The flux equations above now are simplified to:

$$N_{Al} \approx \frac{C^B_{Al,l}}{1/k_{Al,l}} = k_{Al,l}\, C^B_{Al,l}$$

$$N_{Fe} \approx \frac{C^B_{Fe,l}}{1/k_{Fe,l}} = k_{Fe,l}\, C^B_{Fe,l}$$

These relationships are what should be expected from the system provided that the interfacial concentrations of aluminum and iron are almost zero. In other words, the mass transfer of solutes is controlled by their rates of diffusion through the liquid film.

CHAPTER 2 METHODOLOGY

2.1 Characterizing Top Dross Sampled from Galvanizing Lines Using Nitrogen and Air Wiping Systems

As part of International Lead Zinc Research Organization (ILZRO) project ZCO-55 entitled "Dross minimization in Galvanizing Bath", a study was undertaken to sample dross from galvanizing lines using nitrogen and air wiping systems. Top dross samples were collected during normal operating conditions for the production of various product grades from two lines with distinctly different wiping systems. ArcelorMittal Cleveland HDGL uses both nitrogen and air wiping in conventional configuration and U.S.Steel Canada Ltd uses nitrogen wiping exclusively enclosed in a shroud system. A statistical analysis of the rate of dross skimmed robotically as a function of line operating variables such as line speed, coating weight, strip characteristics and knife positioning were carried out. The collected samples were analyzed for chemical composition and microstructural features representative of the variable operating parameters.

2.1.1 Sampling procedure

For the ArcelorMittal operation, most of the samples were taken from the area between the snout and the exiting strip as shown in **Figure 2.1.1-1a**. The sampling device consisted of a perforated spoon 25 cm in diameter with 8 mm diameter holes allowing the molten zinc to decant from the dross. The remaining semi-solid dross was then deposited in a mould and allowed to solidify before quenching. Samples were taken at intervals between 30 and 60 minutes during the day shifts over its two and a half day period producing both GA and GI products. This first series of samples was taken in December 2008 for the case of N_2 wiping. A second series of samples was taken in February 2009, where only air was used. Dross from the surface of the bath was continuously removed by a robotized system and deposited on a weigh scale. A similar sampling procedure was employed at the US Steel Hamilton CGL. Samples were taken over a two day period in March 2009 at a location within the shroud area as indicated in **Figure 2.1.1-1b**.

The sampling device used at U.S.Steel Hamilton was essentially the same as for the samples taken at ArcelorMittal. Although the U.S.Steel facility also incorporated a robotized skimming system, the amount of dross collected was not monitored. In order to collect the dross samples near the strip exit, the shroud was raised for the short period required to take the sample and then lowered.

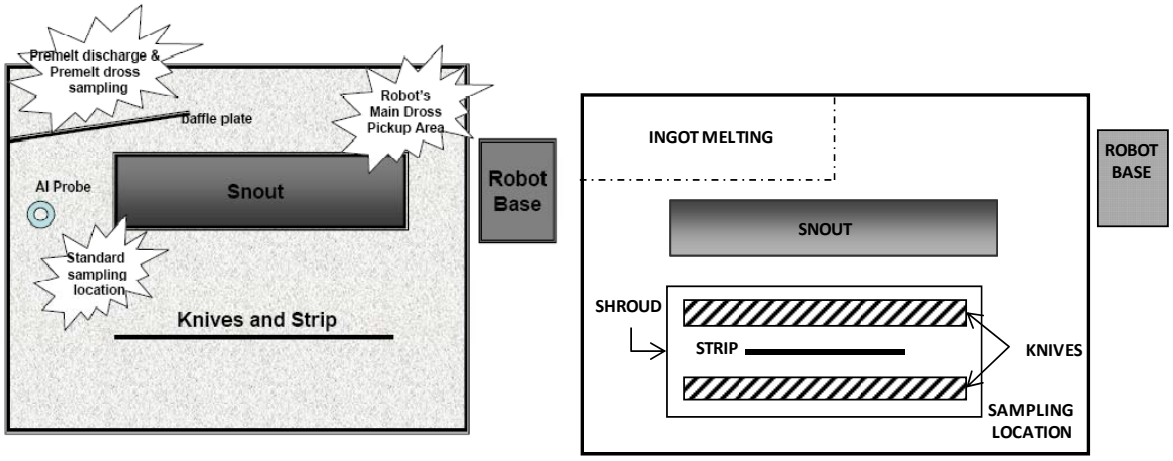

Figure 2.1-1: Schematic of (a) ArcelorMittal Cleveland HDGL and (b) U.S.Steel Hamilton GCL zinc pots showing sampling locations

2.1.2 Bath parameters and line operating conditions

ArcelorMittal has dedicated pots for GA and GI operation which can be put on line in a period of about 2 hours for the transition from one product to another. Both pots are about 300 tonnes measuring 3.7 m by 4.7 m with depth of about 2.8 m. A 25 tonne premelt pot is used for both the GA and GI operation where ingots are charged to produce the melt of the required bath composition. An electrochemical probe is used for the continuous monitoring of the Al content in the bath as shown in **Figure 2.1.1-1a**. The US Steel pot is a 500 ton pot where ingots are charged in a corner of the bath. Both GA and GI products are produced using the same pot. The distinguishing feature of this pot is the shroud used to enclose the wiping system since only N_2 is used in this operation. As shown in **Figure 2.1.1-1b**, when the bottom edge of the shroud is immersed in the bath N_2 escapes through the upper opening above the knives, avoiding air

infiltration to the descending zinc film on the strip. Operating line parameters were collected from the data logging system identifying all coils and the coating conditions that were used in the process. The parameters monitored consisted of line speed, strip width and thickness, steel grade, top and bottom side knife manifold pressure, knife height above bath, knife to strip distance, coating weight, Al content of the bath and temperature.

2.1.3 Statistical analysis of the data

A sensitivity analysis was carried out on the variables monitored in order to determine the influence of the measured parameters on the rate of dross formation. Since the quantity of dross produced was not monitored at the U.S.Steel Hamilton GCL, it was not possible to make a comparison with the ArcelorMittal data. The main objective of the statistical analysis was to demonstrate the incremental difference in dross production for the case of air and N_2 wiping. In addition, differences in top dross production for GA and GI operations were also determined. The effect of other variables such as line speed, air/N_2 knife pressure is also evaluated. The data analyzed consisted of 2353 observations taken over a period of about 5 months, including the periods when the samples were taken. Multiple linear regression was used to discriminate process variables to obtain a model that contains the most influential regressor variables. Al content in the bath (wt %), static manifold pressure of knives (kPa), line speed (m/s) and coating thickness (g/m^2) were chosen as the four most significant variables. First order polynomial models for both air and N_2 wiping operation data were generated using a level of significance of 0.10. Two variable selection techniques were used to model the response average dross formation rate (kg/min): backward elimination and forward selection (2). Using this procedure, it was found that the most influential parameters are the knife pressure, the coating weight and the line speed.

2.1.4 Metallographic analysis of the dross

Representative portions of the collected samples were mounted in bakelite moulds and polished for metallographic analysis. Features such as intermetallic inclusions, oxide particles and

porosities were identified and analysed from images produced using electron microscopy. Secondary electron and electron backscatter images were generated for the representative samples. In addition, energy dispersive X-ray analysis of the different particles and matrix were also carried out. Elemental mapping of the samples was also used to illustrate the distinct elemental distribution of Fe, Al, Zn and O in selected areas, identifying Fe_2Al_5 and $FeZn_{10}$ particles as well as oxides of Zn and Al.

2.2 Experimental simulation of dross generation in GA and GI operations

A bench scale simulation of skimmings generation was conducted in this study as well as an analysis into the rates of skimmings generation at the industrial level. The experimental apparatus consists of a graphite crucible containing liquid zinc at 460 °C which is stirred using a six bladed impeller. A jet of either nitrogen or air was directed on to the bath liquid surface simulating the flow from the air knives. The rate of skimmings generated for variable rotational speeds was measured for zinc compositions corresponding to GA and GI operations. Moreover, a numerical simulation of liquid zinc flow in the crucible was carried out to determine the surface area of the liquid zinc free surface exposed to the gas stream. This calculation was used to determine the rate of skimmings generated per unit surface area for each rotational speed. It was found that the rate of skimmings generated increased with surface velocity and the rate using nitrogen was lower than for air. Furthermore, dross particles imbedded in the skimmings from both laboratory and industrial samples were similar in morphology and composition.

2.2.1 Online sampling of top dross

Please see section 2.1.2 “**Bath parameters and line operating conditions**”.

2.2.2 Bench scale experimental apparatus

As seen in **Figure 2.2.2-1**, the experimental apparatus consists of a graphite crucible containing liquid zinc at 460 °C which is stirred using a six bladed steel impeller. The crucible has a

diameter of 16.5 cm and a height of 23 cm. The maximum load of the crucible never exceeded 20 kg in order the avoid spilling at high mixing rates. Furthermore, the steel impeller served as a continuous source of iron to the system simulating the contact with steel coils in the continuous galvanizing process. An alumina lance, 5 mm in diameter, delivered a jet of either nitrogen or air onto the liquid free surface at a flow rate of 10 SLPM. The lance was held approximately 5 cm from the free liquid surface. The gas jet was used to simulate the effects of the gas wiping system in the industrial process. The rate of skimmings generated for variable rotational speeds was measured for zinc compositions corresponding to GA and GI operations. Moreover, the temperature of the bath and the oxygen content above the free liquid surface were monitored using a thermocouple and an oxygen probe. A second set of experiments was conducted under the same conditions using a shroud which prevented oxygen infiltration to the liquid free surface when a nitrogen jet was used.

Figure 2.2-1: Open (left) and shrouded (right) experimental skimmings generation apparatus

2.2.3 Numerical Simulation of Zinc Flow in the Crucible

A numerical simulation of the flow and mixing of the zinc in the crucible was carried out to determine the surface area and shape of the liquid zinc exposed to the gas stream [2].

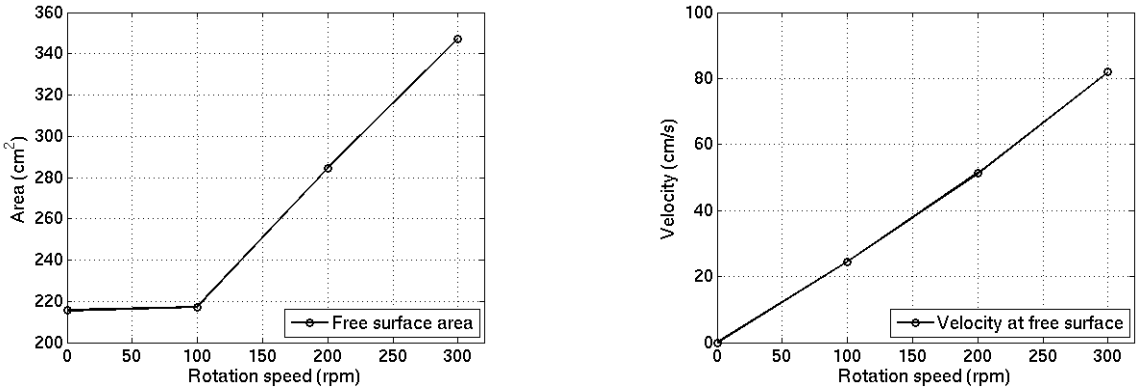

Figure 2.2-2: Free surface area (left) and velocity (right) in the crucible as functions of rotation rate

As seen in **Figure 2.2.3-1**, surface area increased sharply above 100 rpm due to vortex formation and turbulence of the liquid zinc surface. This calculation was used to determine the rate of skimmings generated per unit surface area for each rotational speed.

2.2.4 Metallographic dross analysis

Please see section 2.1.4 "**Metallographic analysis of the dross**".

2.3 Revision of ArcelorMittal Cleveland's HDGL data

The data provided by ArcelorMittal Cleveland's HDGL was revisited in order to better understand the relationship between skimmings generated per coil surface area, line speed and wiping knife pressure. As mentioned before, the industrial parameters of interest are: the mass of skimmings generated (g), surface area of the coated coil (m^2), line speed (m/s) and wiping knife pressure (bar gauge). Data was recorded at the plant from October 2008 to March 2009 but was not continuous. Pockets of information lasting approximately one to four days at a time were investigated and treated by plotting the moving averages of the skimmings generated per coil surface area (g/m^2), the cumulative skimmings generated per coil surface area, line speed and

wiping knife pressure as functions of time (hours). Furthermore, the average value of each parameter over the entire period of time examined was also overlaid onto the moving average plots. Not all the data is presented directly below, only the periods recorded which contained the largest sample sizes will be discussed. Moreover, the situation where the line transitions from nitrogen to air wiping will also be highlighted below. Finally, an attempt was made to discriminate between which parameter, wiping pressure or line speed, had the greatest effect on skimmings generation. This was accomplished by calculating the relative variation from the average value of each parameter.

2.4 Bench Scale Bubbling Experiments

2.4.1 Experimental apparatus

The experimental apparatus used for bubbling gas through the liquid zinc alloy is depicted in **Figure 2.4.1-1**. The goal of the bubbling experiments was to evaluate the liquid-side mass transfer coefficient of the bubbles. This was done by first estimating the rate of oxygen absorption by the liquid free surface using the nitrogen bubbling experiments. Then, from the air bubbling experiments, the flux of oxygen from the bubbles was determined and used to calculate a liquid-side mass transfer coefficient for both aluminum and iron species in solution.

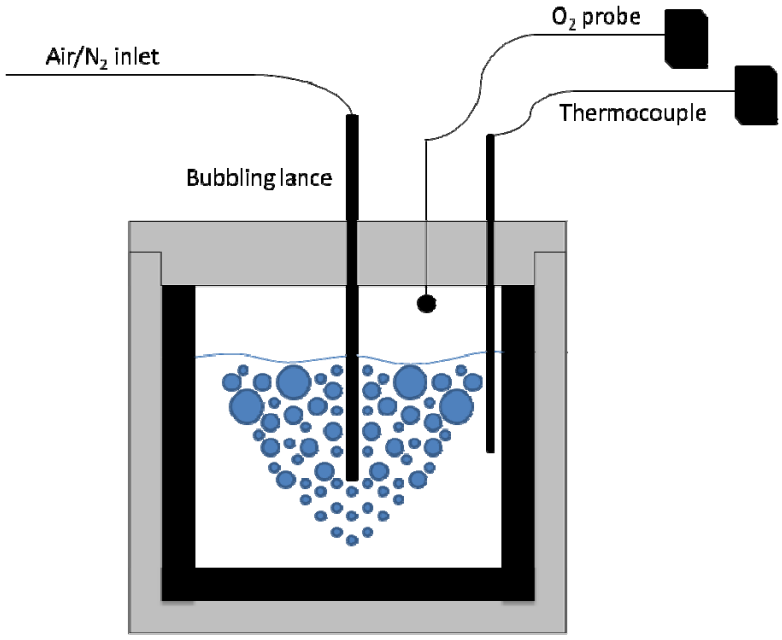

Figure 2.4-1: Bench scale bubbling apparatus

The experimental apparatus consists of a graphite crucible containing liquid zinc at about 460 °C. The crucible has a diameter of 14 cm and a height of 23 cm. Gas is bubbled through the liquid zinc alloy at a flow rate of 1 SLPM (standard litres per minute) using an alumina lance. The lance has a diameter of 5 mm and it delivers a stream of either nitrogen or air through the liquid alloy. The depth of the lance was held at 1.3 cm from the base of the crucible throughout each experimental run. Moreover, the temperature of the bath and the oxygen content above the free liquid surface were monitored using a thermocouple and an oxygen probe. Finally, a shroud was used to cover the top of the crucible. The shroud did not provide a complete seal, some ambient air did leak into the process. The shroud did however reduce the circulation of fresh ambient air to the free liquid surface. This was important since a decrease in oxygen levels near the free liquid surface could be detected and signal the reaction between oxygen and the melt. Four sets of six experiments were conducted. The first set of experiments involved bubbling pure nitrogen through 15.2 kg of liquid alloy. Each of the six experimental runs lasted 20 minutes. Skimmings would progressively build-up at the bath free liquid surface during the bubbling process. At the end of each experiment, the skimmings produced were collected, weighed and analysed for their

chemical compositions. In addition, samples of the bath were also gathered after every experimental run and analysed for their chemical compositions as well. The second set of experiments is essentially a replicate of the first except that the initial crucible load was 17.1 kg. The third and fourth sets of experiments used air instead of nitrogen during the bubbling process. Again, the procedure for these experiments was similar to that of sets one and two. The initial crucible load for the third and forth sets of experiments were 15.7 kg and 17.7 kg respectively. Determining the composition of the skimmings and bath samples was done by digesting 1 g of each sample with a 50 wt% HCl solution. The impregnated acid solution was then examined by absorption spectrophotometry.

CHAPTER 3 RESULTS

3.1 Characterizing Top Dross Sampled from Galvanizing Lines Using Nitrogen and Air Wiping Systems

3.1.1 Industrial Data

The entire set of logged data was analysed for the 5 month period to determine the effects of the knife pressure, the line speed and coating weight on the rate of dross formation. Each of these variables was grouped into high, medium and low values and the results are presented in for charts comparing air and N_2 wiping. The bulk of the data is for GI operation. A limited amount of data was available for GA operation. A comparison of the rate of dross formation for GA and GI using N_2 wiping is also presented. **Figures 3.1.1-1a** and **3.1.1-1b** show the effect of knife pressure on the dross formation rate. For the case of air wiping at high pressure, slightly more dross is produced than for the case of N_2 wiping. This is also true for the low range of knife pressure where the difference is even larger. However, for medium values, the N_2 wiping resulted in a higher dross rate which is unexpected and could be attributed to statistical variation.

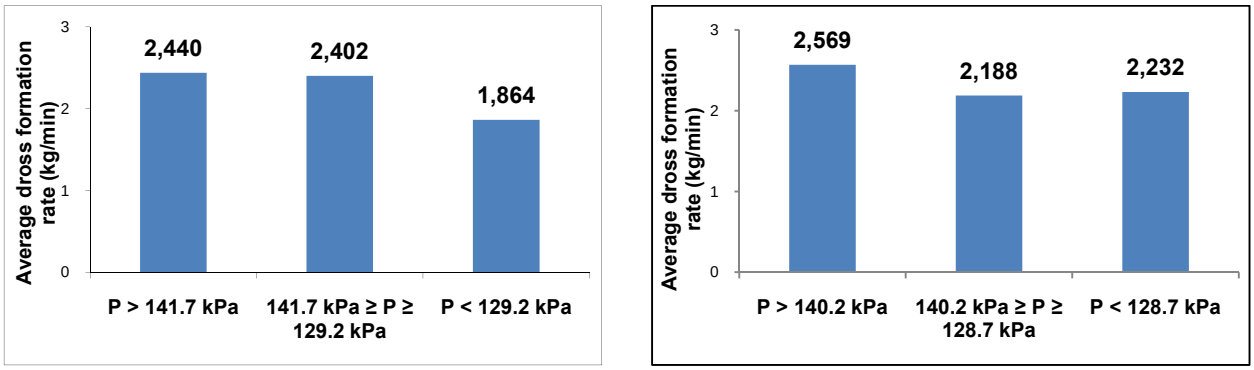

Figure 3.1-1: Effect of knife manifold pressure on dross formation rate using (a) nitrogen and (b) air for GI operation at ArcelorMittal Cleveland HDGL

The effect of line speed on dross formation is more pronounced as shown is **Figures 3.1.1-2a** and **3.1.1-2b**. As expected, increasing line speed increases the rate of dross formation from 1.697 to

2.611 kg/min for N_2 and from 1.931 to 2.680 kg/min for air, for the range of line speeds indicated. The difference at high line speeds is marginal, whereas at low range of line speeds (less than 1.90 m/s), the dross rate is about 14% lower.

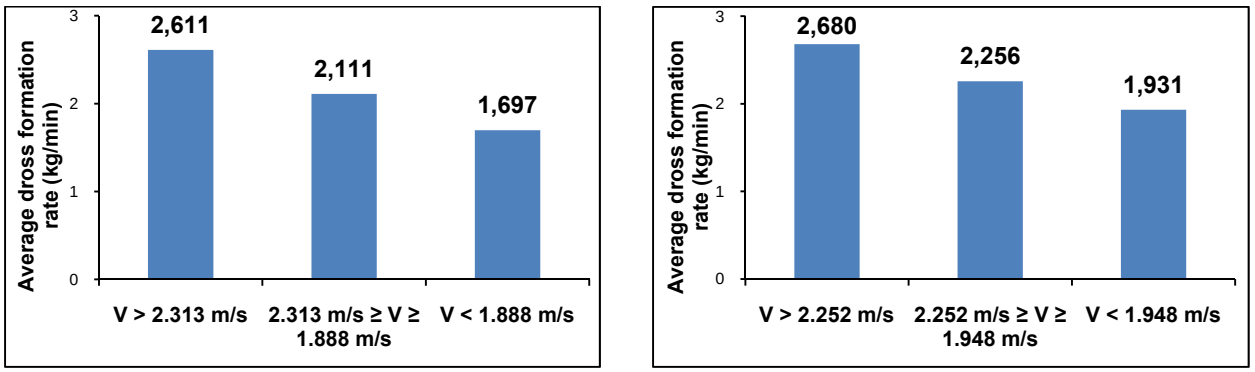

Figure 3.1-2: Effect of line speed on dross formation rate using (a) nitrogen and (b) air for GI operation at ArcelorMittal Cleveland HDGL

The effect of coating weight on dross formation does not show any significant difference over the range of values of this analysis. However, the values for N_2 wiping are all slightly lower than for the equivalent coating weight using air wiping as shown in **Figures 3.1.1-3a** and **3.1.1-3b**. The average value for N_2 wiping for all the data is about 2.189 kg/min compared to 2.321 kg/min for air.

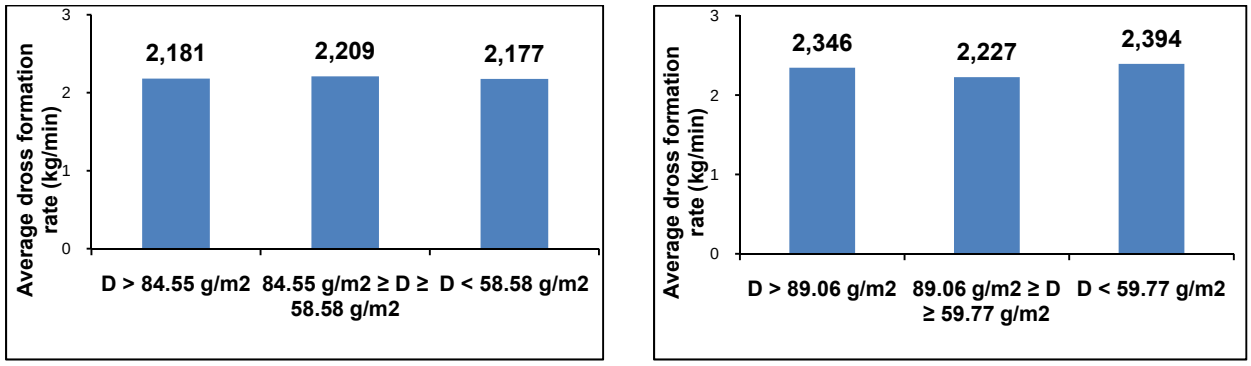

Figure 3.1-3: Effect of coating weight on dross formation rate using (a) nitrogen and (b) air for GI operation at ArcelorMittal Cleveland HDGL

A limited set of data for GA and GI operation at equivalent line speed using N_2 wiping was also analyzed. Both production periods had a time span of about 3 hours (180 minutes) and for a constant line speed of about 1.5 m/s and knife pressure of about 120 to 130 kPa. The results in **Figures 3.1.1-4** show about a 38% reduction of top dross production for the GA operation at these conditions to an average value of 1.24 kg/min compared to 1.72 kg/min for the GI production.

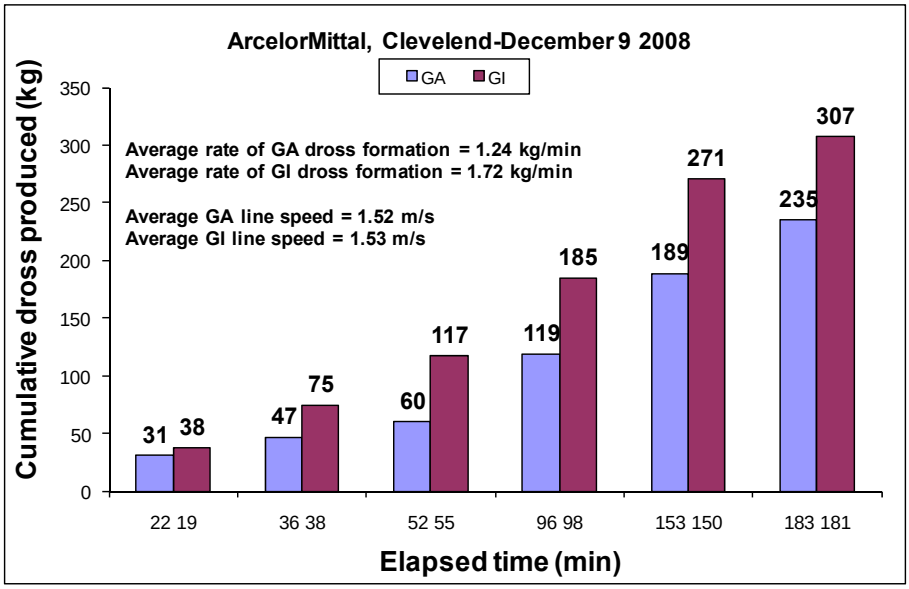

Figure 3.1-4: Cumulative dross produced versus time for GA and GI operations

3.1.2 Dross Characterization

In general, a large variability in composition and microstructure was observed on examining the polished sections of the samples of top skimmings taken at the two galvanizing knives. The composition is very heterogeneous consisting of a mixture of intermetallic particles of either, or both, Fe_2Al_5 or $FeZn_{10,}$ of regions of oxide films and of amorphous particles of oxides of zinc or aluminum within a matrix of liquid zinc. The spatial distribution of these phases can be observed in all of the samples taken during GI and GA operations at ArcelorMittal and at U.S.Steel, showing two different types of morphologies. Some regions show areas containing crystalline

Fe_2Al_5 or $FeZn_{10}$ particles of various sizes together with dispersed oxide particles. Other regions of the same sample can show areas devoid of intermetallic particles and are composed of oxide phases in the zinc matrix. Secondary electron images and the backscatter electron images are presented in **Figures 3.1.2-1a** and **3.1.2-1b** for a GI sample from ArcelorMittal.

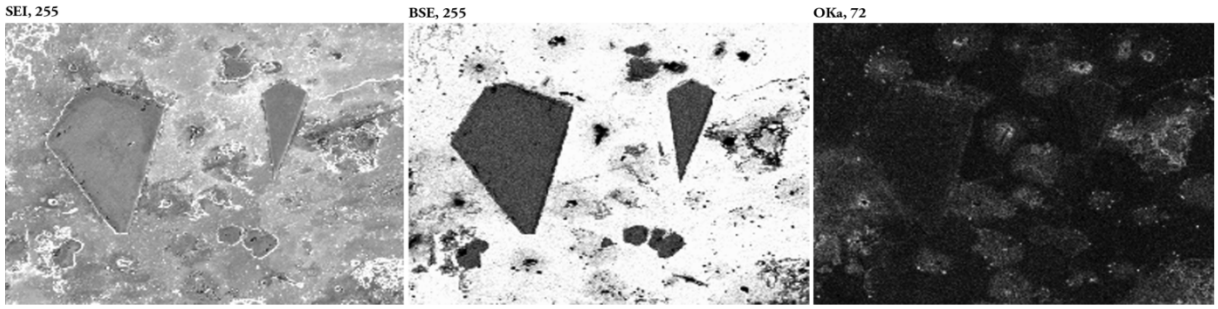

(a) Secondary electron image (b) Backscatter electron image (c) Oxygen distribution

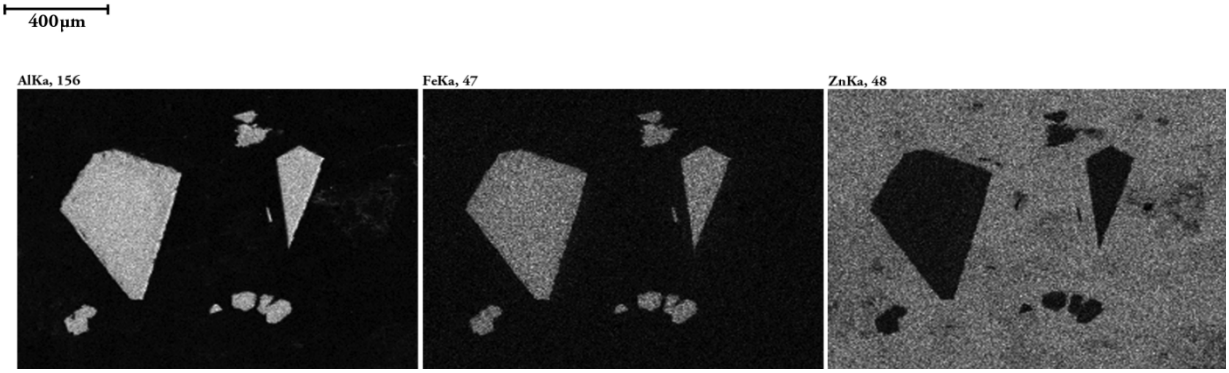

(d) Aluminum distribution (e) Iron distribution (f) Zinc distribution

Figure 3.1-5: Micrographs of top dross (Fe_2Al_5) section sampled from ArcelorMittal GI process using nitrogen wiping

The same area was analyzed using dispersive X-ray mapping. The characteristic X-ray (K_α) signal for oxygen, aluminum, iron and zinc, scanned over the same surface area generates a spatial distribution of these elements over the selected area. The series of images clearly identify the crystalline Fe_2Al_5 particles, as well as the oxide particles in this area. Due to the low atomic weight of oxygen compared to Al, Fe and Zn, the oxygen distribution shown in **Figure 3.1.2-1c**

is not as distinct as the elemental distribution of Al (**Figure 3.1.2-1d**), Fe (**Figure 3.1.2-1e**) and Zn (**Figure 3.1.2-1f**). As expected, the GI operation indicates the presence of only Fe_2Al_5 particles, since ArcelorMittal uses a dedicated pot for each product.

Another region of the same sample is shown in **Figure 3.1.2-2**, together with the same distribution of elements in this area. It can be seen that this area is void of intermetallic particles of dross but shows a relatively porous agglomeration of zinc and aluminum oxides. As previously, **Figures 3.1.2-2a** and **3.1.2-2b** show the secondary electron and backscatter electron images, whereas **Figures 3.1.2-2c**, **3.1.2-2d**, **3.1.2-2e** and **3.1.2-2f** show the spatial distribution of oxygen, aluminum, iron and zinc.

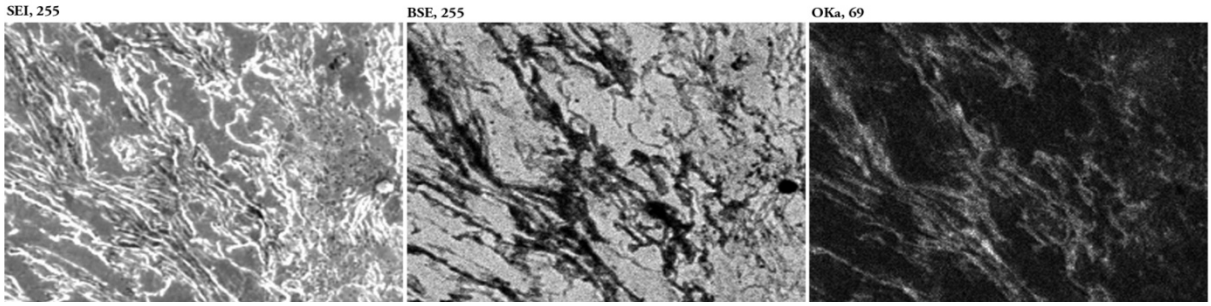

(a) Secondary electron image (b) Backscatter electron image (c) Oxygen distribution

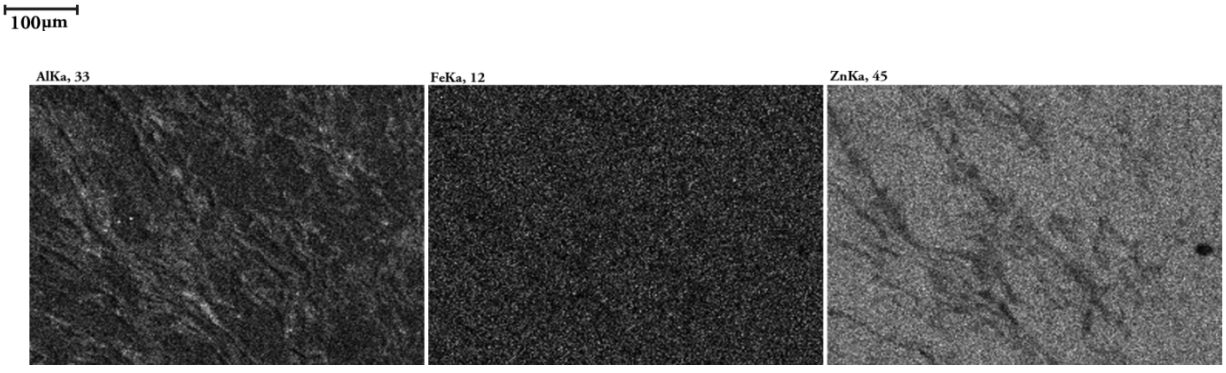

(d) Aluminum distribution (e) Iron distribution (f) Zinc distribution

Figure 3.1-6: Micrographs of dross section with oxide films sampled from ArcelorMittal GI process using nitrogen wiping

The analysis of a sample taken during a GA operation at ArcelorMittal is shown in **Figures 3.1.2-3** and **3.1.2-4**. **Figure 3.1.2-3** shows an area with a characteristic $FeZn_{10}$ particle which appears to be dissolving due to its rounded shape. Secondary electron (**Figure 3.1.2-3a**) and backscatter electron images (**Figure 3.1.2-3b**) show the particle shape and general morphology in the region. Elemental distribution maps clearly identify the intermetallic particle as $FeZn_{10}$ as illustrated in **Figures 3.1.2-3e** and **3.1.2-3f**. The difference in the concentration of Zn for the particle and the matrix is not clearly distinguishable. However, it is clear that this particle contains only traces of Al as seen in **Figure 3.1.2-3d** and a distinct region of a high concentration of iron.

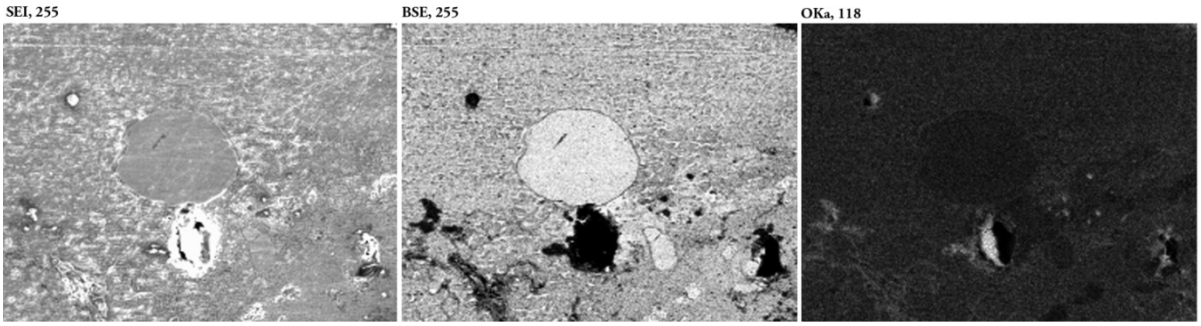

(a) Secondary electron image (b) Backscatter electron image (c) Oxygen distribution

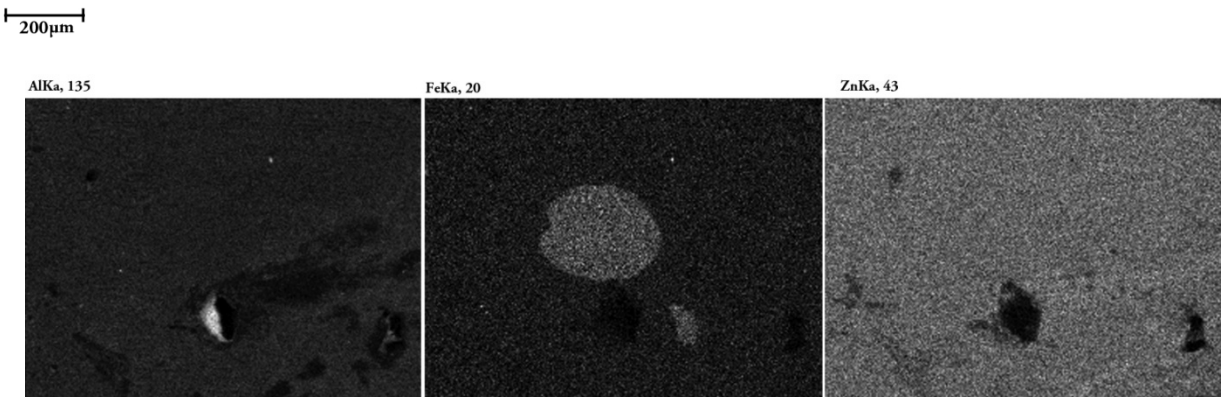

(d) Aluminum distribution (e) Iron distribution (f) Zinc distribution

Figure 3.1-7: Micrographs of bottom dross ($FeZn_{10}$) section sampled from ArcelorMittal GA process using nitrogen wiping

In another region of the same sample shown in **Figure 3.1.2-4**, we can again observe a heterogeneous and porous area (**Figure 3.1.2-4a** and **3.1.2-4b)** devoid of bottom dross particles. This area is composed predominantly of oxides of aluminum and zinc (**Figures 3.1.2-4d** and **3.1.2-4f**) as indicated by the iron distribution which is relatively homogeneous and at a low concentration.

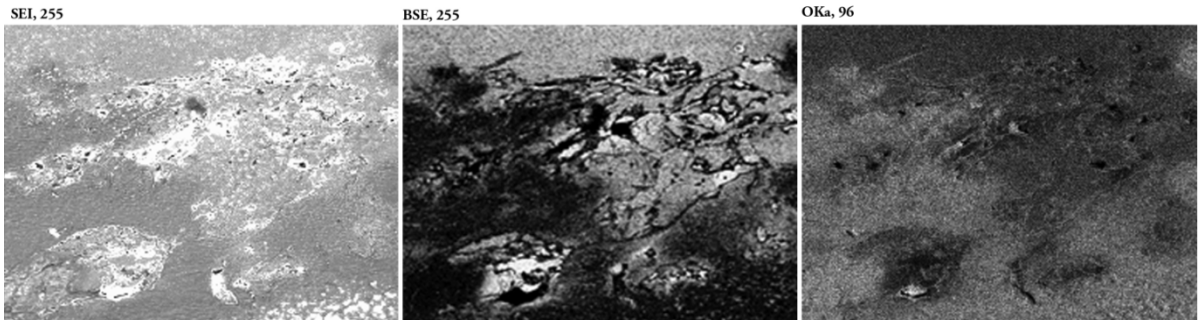

(a) Secondary electron image (b) Backscatter electron image (c) Oxygen distribution

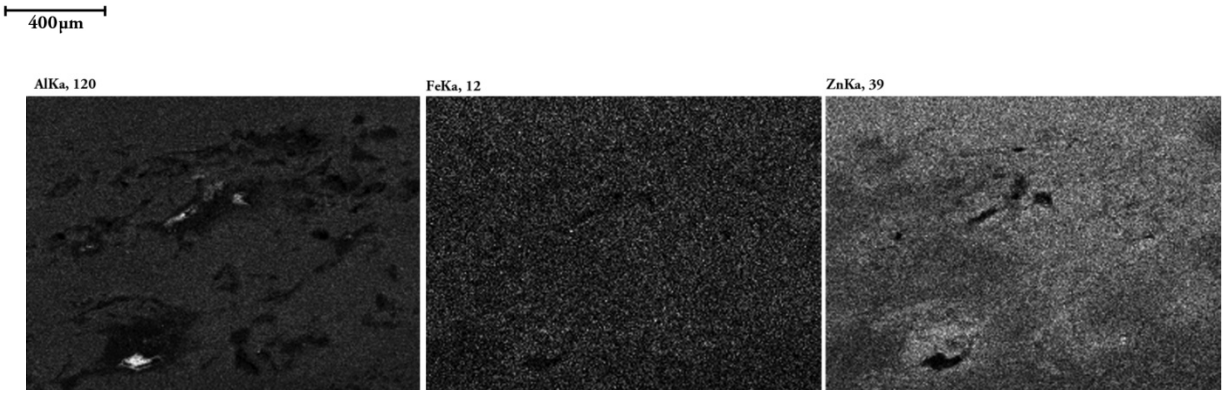

(d) Aluminum distribution (e) Iron distribution (f) Zinc distribution

Figure 3.1-8: Micrographs of dross section with oxide films sampled from ArcelorMittal GA process using nitrogen wiping

Figure 3.1.2-5 shows an agglomeration of metallic particles in a zinc matrix in a sample taken from the U.S.Steel Hamilton CGL during GI operation. The secondary electron (**Figure 3.1.2-5a**) and backscatter electron images (**Figure 3.1.2-5b**) clearly show a different composition of the

two types of particles found in this area. Elemental analysis confirms the presence of a $FeZn_{10}$ particle at the top left of the image as well as two agglomerated particles of Fe_2Al_5. The spatial distributions of Al, Fe and of Zn are shown in **Figures 3.1.2-5d**, **3.1.2-5e** and **3.1.2-5f** confirming the two different compositions. The presence of two types of particles can be expected since their operation uses the same pot for both GA and GI operations. Also, the pot is unusually large, the accumulated bottom dross is never completely removed during GI operations and the $FeZn_{10}$ particles can therefore also be transported into the bath with the Fe_2Al_5 particles during the GI operation.

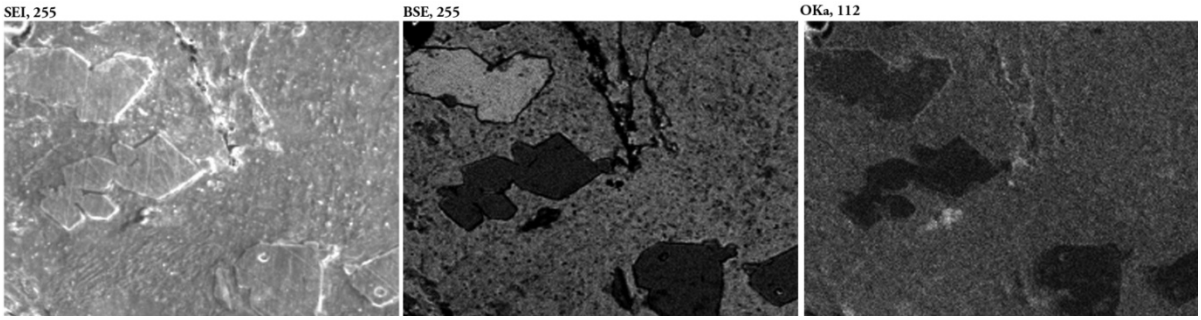

(a) Secondary electron image (b) Backscatter electron image (c) Oxygen distribution

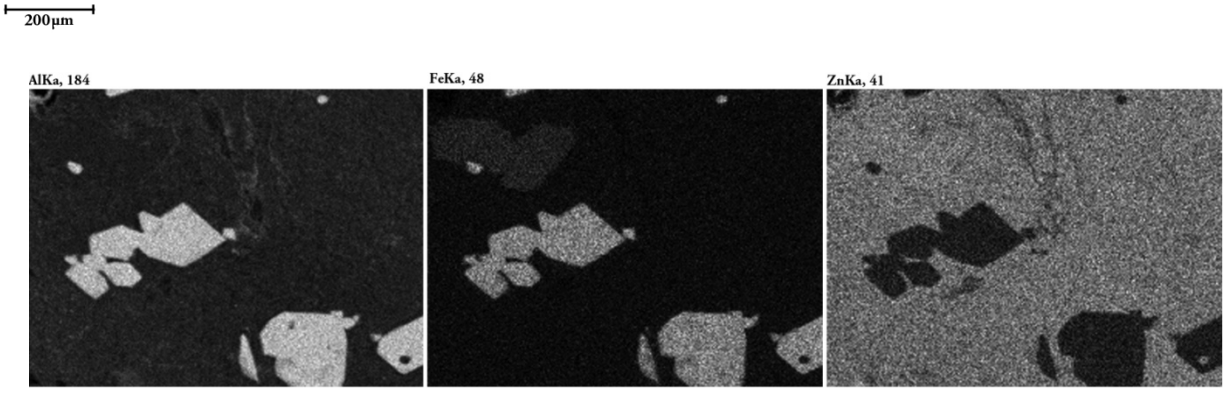

(d) Aluminum distribution (e) Iron distribution (f) Zinc distribution

Figure 3.1-9: Micrographs of dross section sampled from U.S.Steel Hamilton GI process using nitrogen wiping showing both bottom ($FeZn_{10}$) and top dross (Fe_2Al_5) particles

As in the ArcelorMittal samples, the U.S.Steel samples of top dross skimmings also show areas devoid of intermetallic particles as shown in **Figure 3.1.2-6**. The area clearly shows porous folds of oxide film layers as indicated in the secondary electron (**Figure 3.1.2-6a**) and backscatter electron (**Figure 3.1.2-6b**) images. The oxygen content is still significant as shown in **Figure 3.1.2-6c** even though this operation uses nitrogen wiping exclusively. Upon examining the Al and Zn distribution for this area (**Figures 3.1.2-6d** and **3.1.2-6f**), it can be deduced that the oxide is predominantly ZnO.

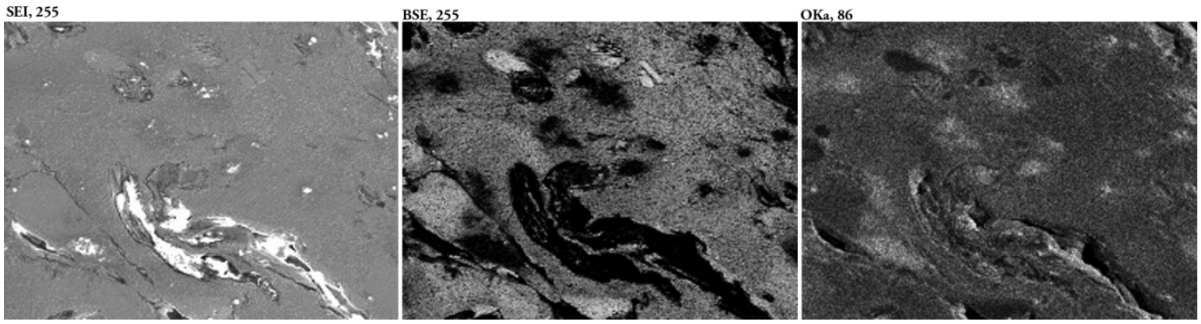

(a) Secondary electron image (b) Backscatter electron image (c) Oxygen distribution

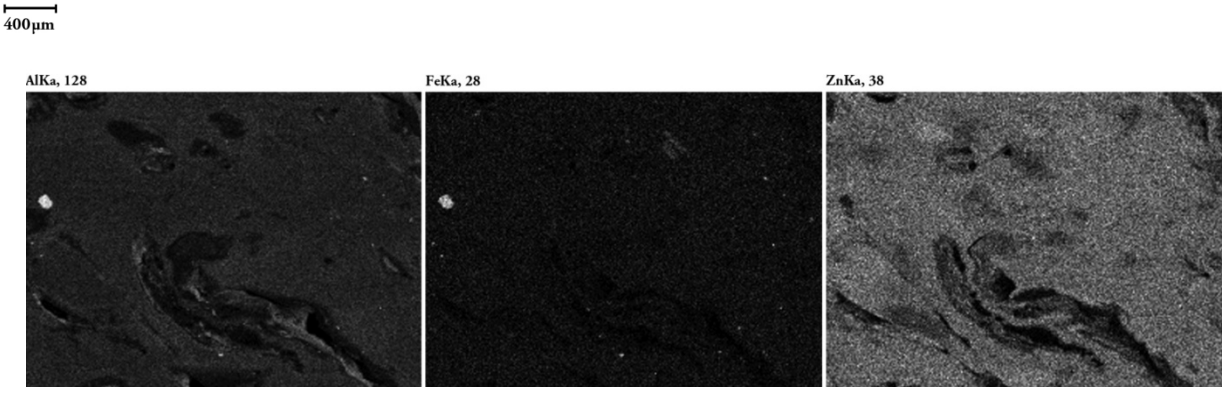

(d) Aluminum distribution (e) Iron distribution (f) Zinc distribution

Figure 3.1-10: Micrographs of dross section with oxide films sampled from U.S.Steel Hamilton GI process using nitrogen wiping

3.2 Experimental simulation of dross generation in GA and GI operations

3.2.1 Analysis of skimmings generation: ArcelorMittal Cleveland's HDGL

The data represents two complete days of continuous GI operation at ArcelorMittal Cleveland's HDGL. Approximately midway through this period, the line switched from N_2 wiping to air wiping as seen in **Figure 3.2.1-1**. Among others, the operating parameters provided by the plant included the mass of skimmings collected per coil, the coil surface area and its residence time in the GI bath. Therefore, a specific rate of skimmings generation per coil at the plant was calculated and its units are g/hr/m^2. The shift from N_2 to air wiping occurred approximately 27 hours after the start of the monitoring test. The specific rate of skimmings generation remains stable 6 hours into N_2 wiping but begins to destabilize after the 33 hour mark. Clearly, as seen in **Figure 3.2.1-1**, air wiping has a significant effect on the amount of skimmings produced compared to N_2 wiping.

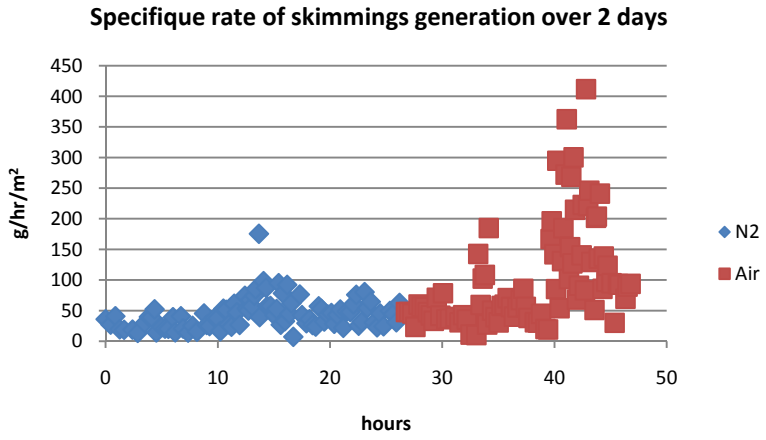

Figure 3.2-1: Specific rate of skimmings generation per coil vs. time at ArcelorMittal Cleveland's HDGL

The instantaneous specific rates of skimmings generation shown above were summed over time in order to produce the cumulative specific rate of skimmings generation curve shown in **Figure 3.2.1-2** below.

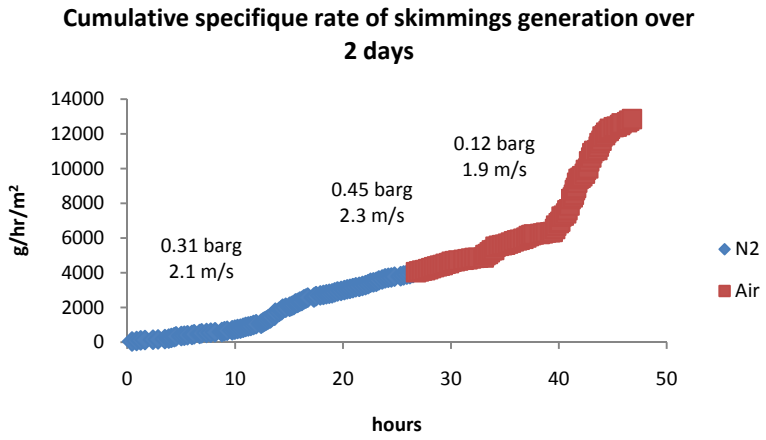

Figure 3.2-2: Cumulative specific rate of skimmings generation per coil vs. time at ArcelorMittal Cleveland's HDGL

The linear segments are the periods of time when line speed and wiping knife pressure are nearly constant. "Bumps" in the curve occur when there is a change in these two parameters. Between 0 and 10 hours, the line operates at a line speed of 2.1 m/s and a wiping pressure of 0.31 barg. The line speed and wiping pressure changed to 2.3 m/s and 0.45 barg between 20 and 30 hours and to 1.9 m/s and 0.12 barg between 40 and 43 hours. It was previously shown [3] that the rate of skimmings formation is sensitive to both line speed and wiping knife pressure. In the present analysis, it can be shown that skimmings formation becomes significantly more sensitive to these two parameters when an air whipping is used over N_2 wiping.

3.2.2 Analysis of skimmings generation: bench scale apparatus

A series of bench scale experiments were conducted for GA compositions ranging between 0.11 and 0.14 wt% Al. Two cases were examined: a shrouded crucible using both air and N_2 impinging jets and an open crucible using both air and N_2 impinging jets. **Table 3** summarizes the results.

Table 3: Rates of skimmings generation under air/N2 and open/shrouded conditions

		Shrouded crucible		**Open crucible**	
		GA-N2	GA-Air	GA-N2	GA-Air
T bath (°C)		461	458	458	467
[O_2] above bath (mol%)		0.00	20.91	9.76	20.90
Generation rate (g/s)	100 rpm	-	-	0.0248	0.0359
	200 rpm	0.0653	0.0914	0.0539	0.125
	250 rpm	0.0812	0.141	-	-
	300 rpm	0.0771	0.303	0.291	0.805
Specific generation rate ($g/s/m^2$)	100 rpm	-	-	1.15	1.66
	200 rpm	2.30	3.21	-	-
	250 rpm	2.56	4.46	1,89	4.41
	300 rpm	2.21	8.69	8.34	23.1

The average skimmings generation rate is the ratio of mass of skimmings produced over the duration of the experimental run. The average specific skimmings generation rate is the ratio of average skimmings generation rate to the free liquid surface area [2] for a particular rotation rate. Clearly, the use of an air jet significantly contributed to the formation of skimmings especially at high impeller rotation rates. Moreover, it is evident that shrouding the bath over a N_2 jet inhibited the formation of skimmings to a greater degree than all the other cases.

Figure 3.2.2-1 below is a plot of the average specific skimmings generation rate as a function of impeller rotation rate for GA and GI compositions ranging between 0.11-0.14 wt% Al and 0.16-0.19 wt% Al respectively. The data collected would suggest that at low rotation rates, the specific rates of both GA and GI bath compositions produce similar amounts of skimmings but that is no

longer evident at higher rotation rates. Furthermore, the specific rate of skimmings generation for GA remains relatively constant over the range of rotation rates used.

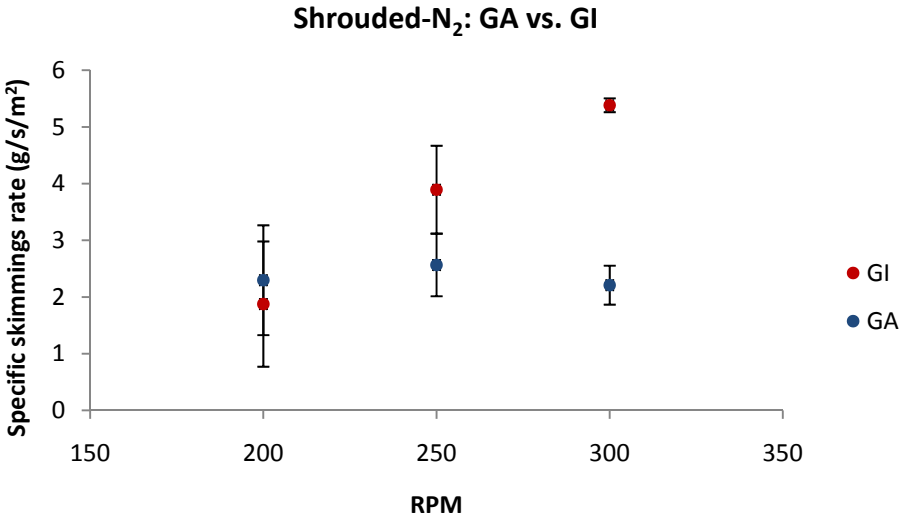

Figure 3.2-3: Specific rate of skimmings generation vs. impeller rotation rate for both GA and GI

Figure 3.2.2-2 below compares the limiting cases of a shrouded crucible using nitrogen and an open crucible using air for a GI composition ranging between 0.16 wt% Al and 0.19 wt% Al. The data depicts the contribution of air to the amount of skimmings formed at high rotation rates.

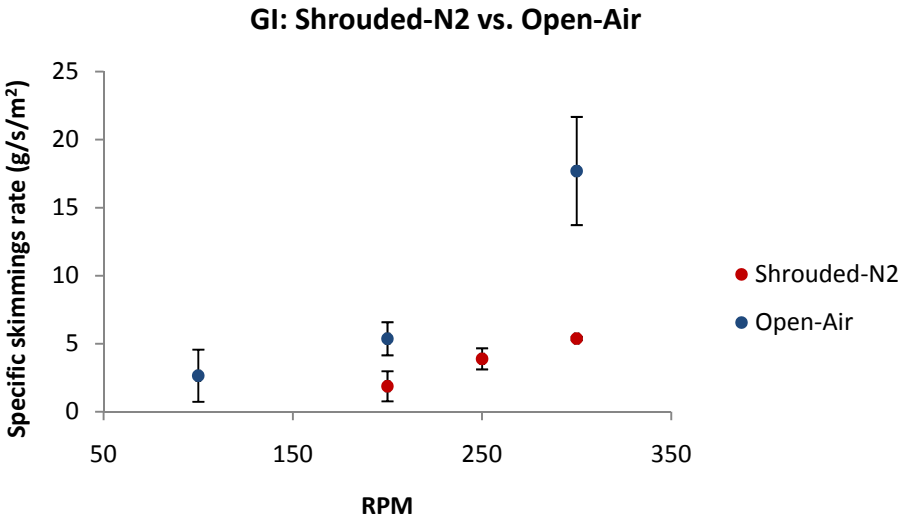

Figure 3.2-4: Effect of air on the specific rate of skimmings formation for GI

3.2.3 Skimmings characterization

Previous analyses have shown that industrial skimmings have a large variability in composition and microstructure. The same can be said in the present study upon examining polished sections of the skimmings samples collected in the laboratory. Images of the samples taken by dispersive X-ray mapping are presented in **Figures 3.2.3-1a**, **b**, **c** and **d**. The images display the Zn distribution across the sample surface area. The composition is heterogeneous consisting of a mixture of intermetallic particles of either, or both, $Fe_2Al_5Zn_x$ or $FeZn_{10}Al_y$. Moreover, the skimmings samples also contain Zn, Al and Fe oxide films and porosities. Taking **Figures 3.2.3-1a** and **3.2.3-1b**, porosities as well as oxide films are present in the analyzed skimmings sample. As for **Figure 3.2.3-1c**, porosities mixed in with agglomerations of intermetallic particles and oxides are present in the sample. **Figure 3.2.3-1d** shows how the oxide films can form envelopes which can encase intermetallic particles and bath solution within them.

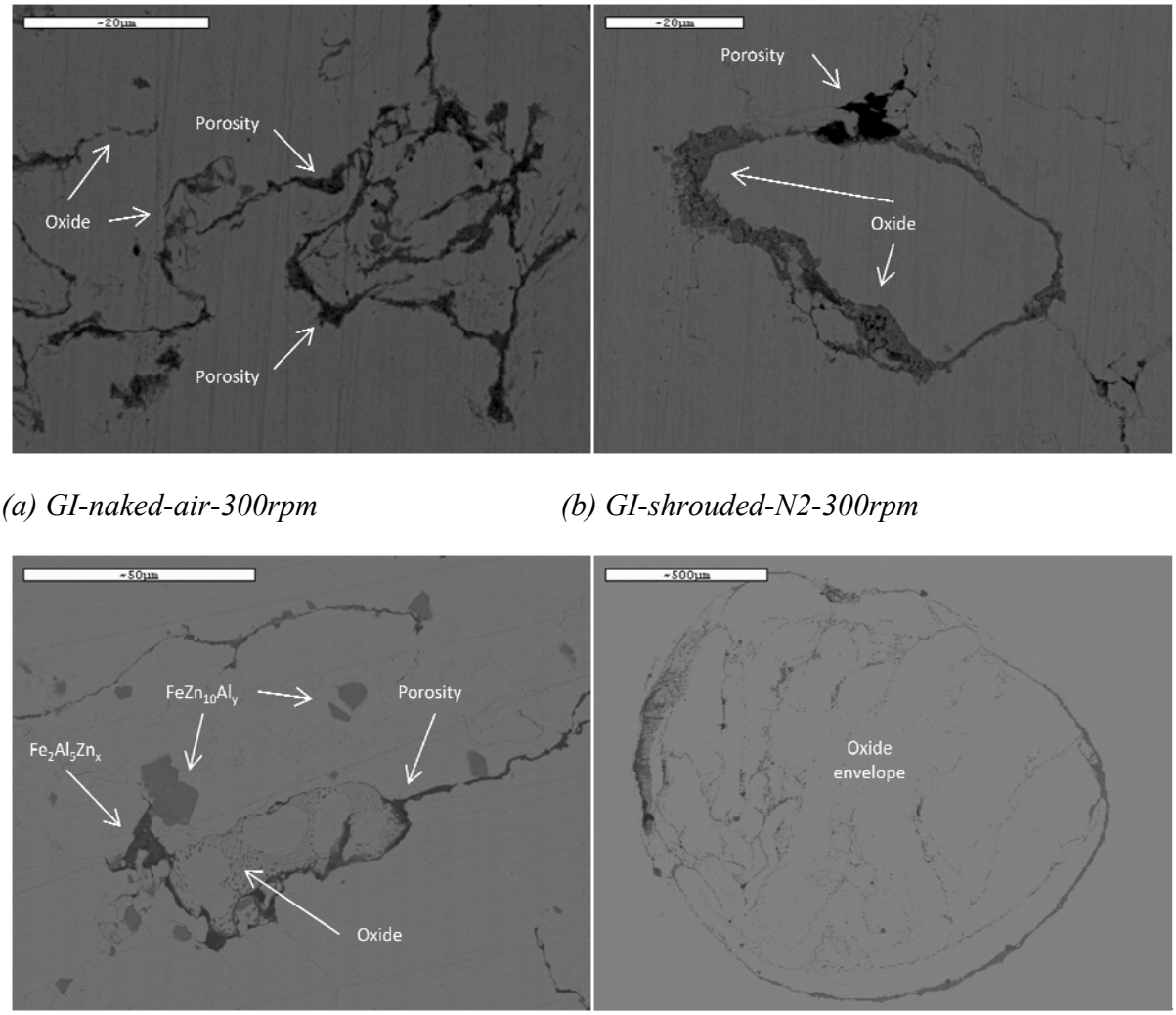

(a) GI-naked-air-300rpm *(b) GI-shrouded-N2-300rpm*

(c) GA-naked-air-300rpm *(d) GA-shrouded-N_2-300rpm*

Figure 3.2-5: Images of the polished sections of the skimmings samples collected in the laboratory taken by dispersive X-ray mapping

3.3 Revision of ArcelorMittal Cleveland's HDGL data

In section 3.1, it was shown that the rate of skimmings generation increased with line speed and wiping knife pressure regardless of which wiping gas (air or N_2) was being used in the process. Moreover, it was also made clear, in the same chapter, that the coating deposition rate had a small effect on the rate of skimmings generation. The findings in section 3.2 show how the degree of turbulence in the liquid zinc bath can strongly influence the formation of skimmings i.e., the size of the exposed liquid surface and the velocity of the fluid at the free surface. Therefore, the following analysis will focus on looking at process parameters which affect the turbulence of the liquid zinc near the strip exit region of an industrial galvanizing bath. For galvanizing processes in general, the skimmings per coil surface area will increase with line speed and wiping pressure regardless of the type of wiping gas being used. This is intuitive since increasing these two process parameters would increase the return flow of liquid zinc into the bath. Furthermore, the cumulative skimmings per coil surface area grows more quickly with time as the line speed and wiping pressure are increased. The boost in cumulative skimmings per coil surface area is much more pronounced when air wiping is used compared to nitrogen wiping. This is seen in **Figures 3.3.1-1**, **3.3.1-2**, **3.3.2-1** and **3.3.2-2**.

3.3.1 Moving average of skimmings per coil, line speed and wiping pressure during nitrogen wiping

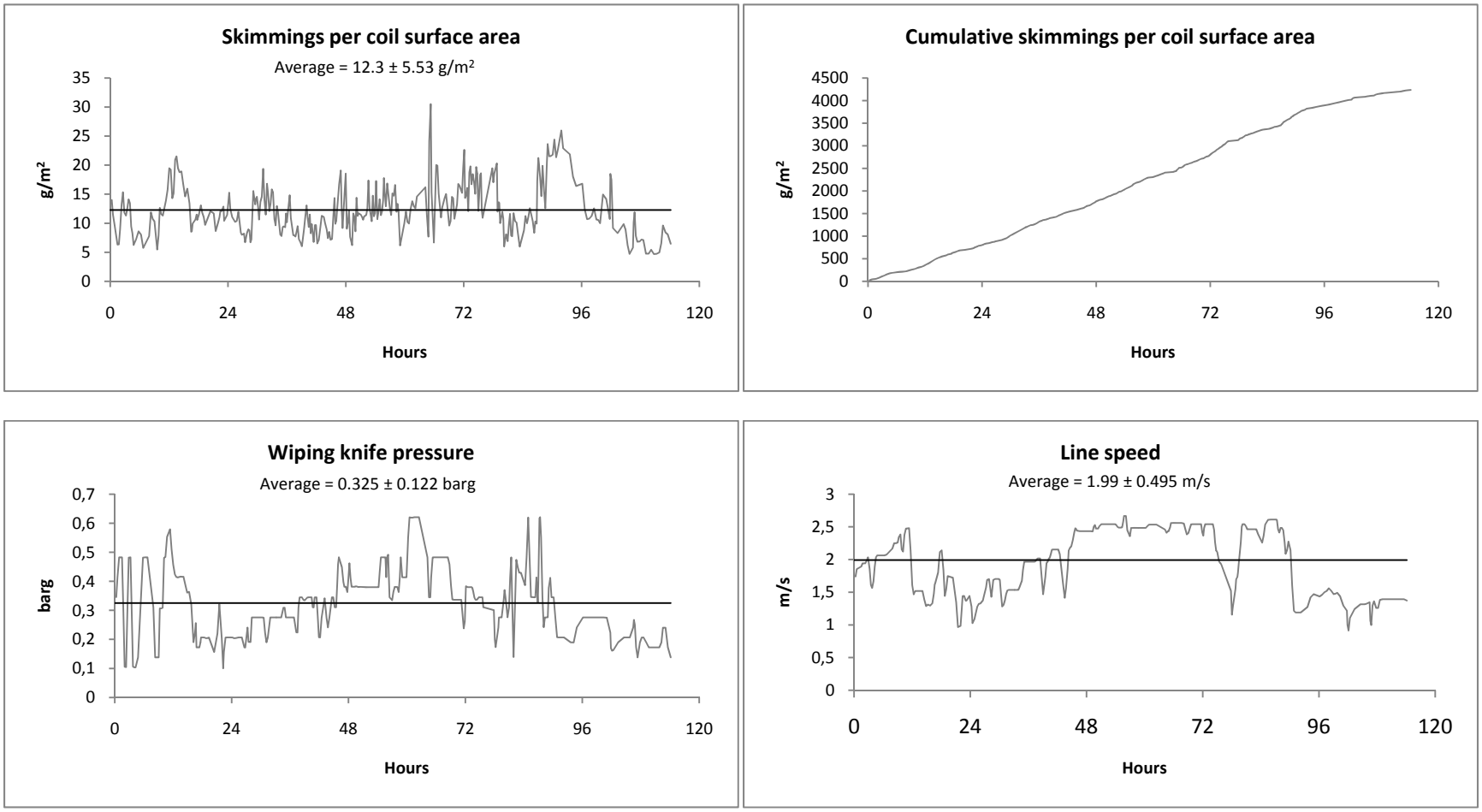

Figure 3.3-1: Operating data from ArcelorMittal Cleveland's HDGL from October 27th to November 1st 2008

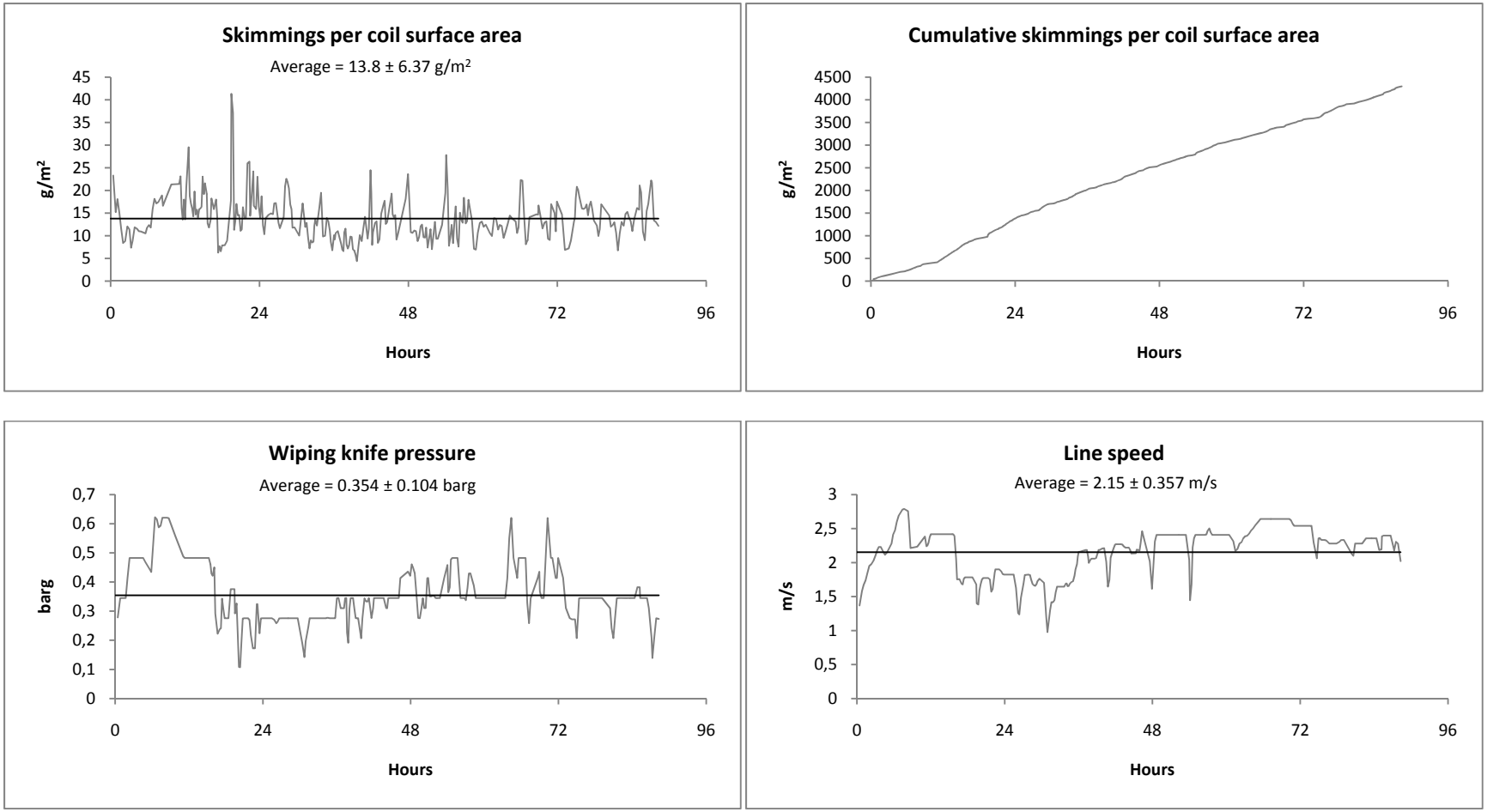

Figure 3.3-2: Operating data from ArcelorMittal Cleveland's HDGL from December 1st to December 4th 2008

3.3.2 Moving average of skimmings per coil, line speed and wiping pressure during air wiping

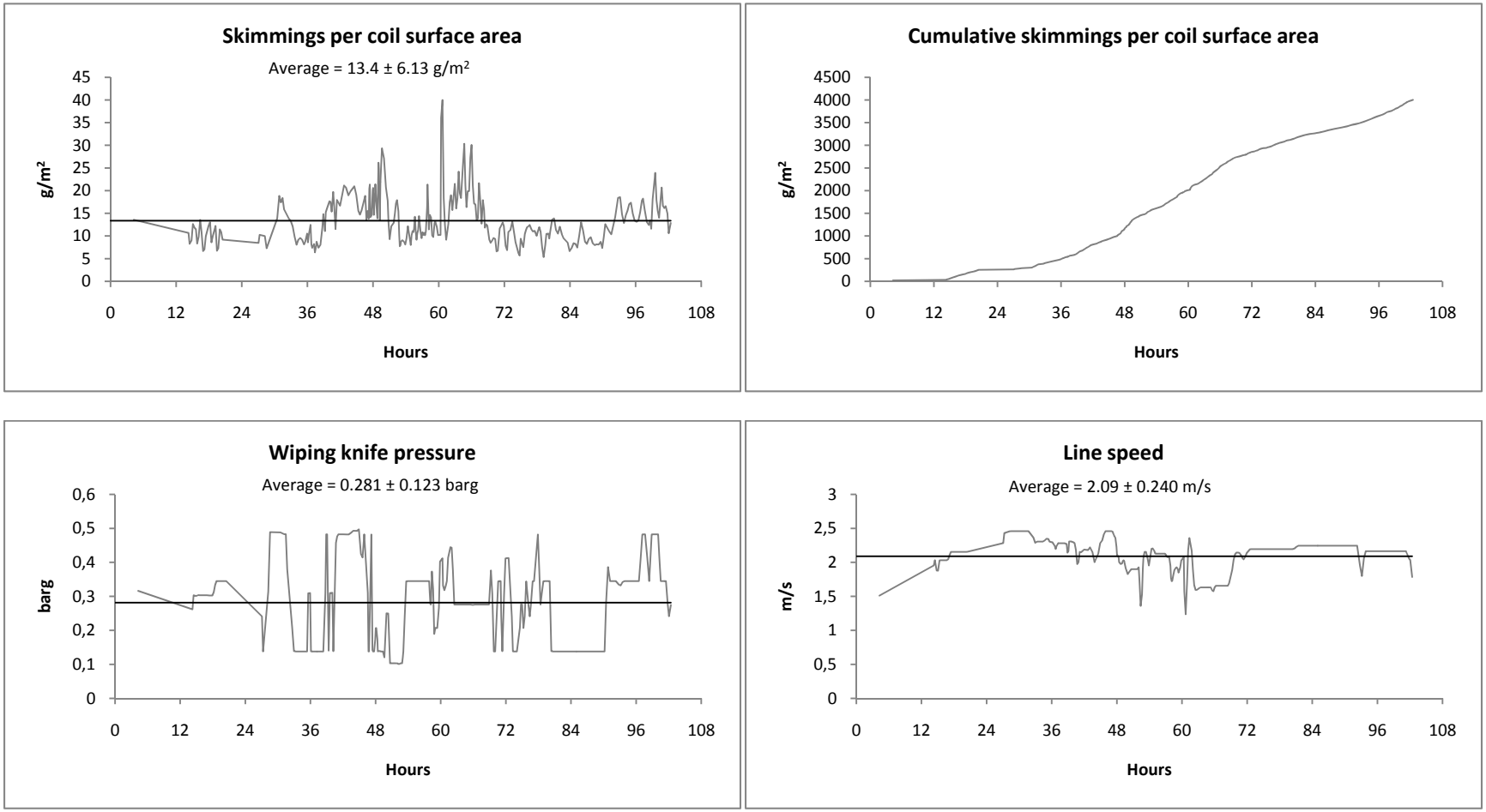

Figure 3.3-3: Operating data from ArcelorMittal Cleveland's HDGL from February 18th to February 22nd 2009

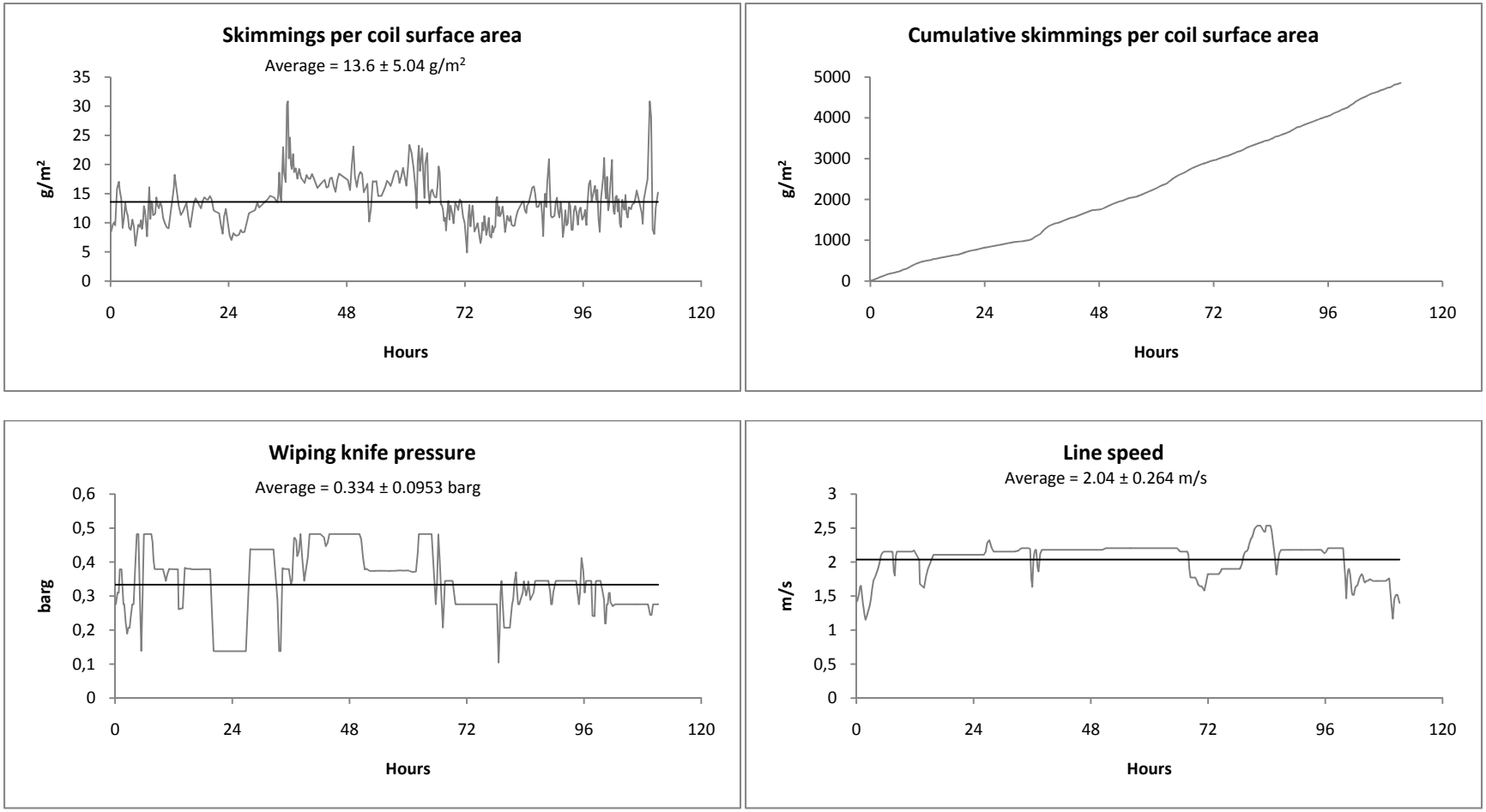

Figure 3.3-4: Operating data from ArcelorMittal Cleveland's HDGL from March 9th to March 14th 2009

3.3.3 Comparing air and nitrogen wiping at ArcelorMittal Cleveland's HDGL

The data for nitrogen and air wiping presented early was organized into pairs, shown below, for comparative purposes. Statistically, using a level of significance of 5%, the data gathered from October 27th to November 1st 2008 and from March 9th to March 14th 2009 had equal average bath aluminum composition, line speed and wiping knife pressure. These results are summarized in **Table 4**. The data gathered over the periods of December 1st to December 4th 2008 and February 18th to February 22nd 2009 had, statistically, using a level of significance of 5%, equal bath aluminum composition and specific rate of skimmings generation. These results are shown in **Table 5**.

Table 4: Skimmings generated using N_2 and air wiping for similar conditions

	[Al]bath (wt%)	Line speed (m/s)	Wiping pressure (barg)	Skimmings per coil surface area (g/m2)
N2 wiping	0.189±0.00390	1.99±0.495	0.325±0.122	12.3±5.53
Air wiping	0.186±0.00347	2.04±0.264	0.334±0.0953	13.6±5.04

For the operating conditions shown above, air wiping as opposed to nitrogen wiping produces 9.6% more skimmings per surface area of coil immersed in the bath.

Table 5: Skimmings generated using nitrogen and air wiping for different conditions

	[Al]bath (wt%)	Line speed (m/s)	Wiping pressure (barg)	Skimmings per coil surface area (g/m2)
N2 wiping	0.192±0.00333	2.15±0.357	0.354±0.104	13.8±6.37
Air wiping	0.195±0.00629	2.09±0.240	0.281±0.123	13.4±6.13

Though the period of nitrogen wiping operated at higher line speeds and wiping knife pressures, air wiping still produced as much skimmings per coil surface area as nitrogen wiping. Therefore, nitrogen wiping does inhibit the formation of skimmings.

3.3.4 Moving average of skimmings generation while transitioning from nitrogen to air wiping

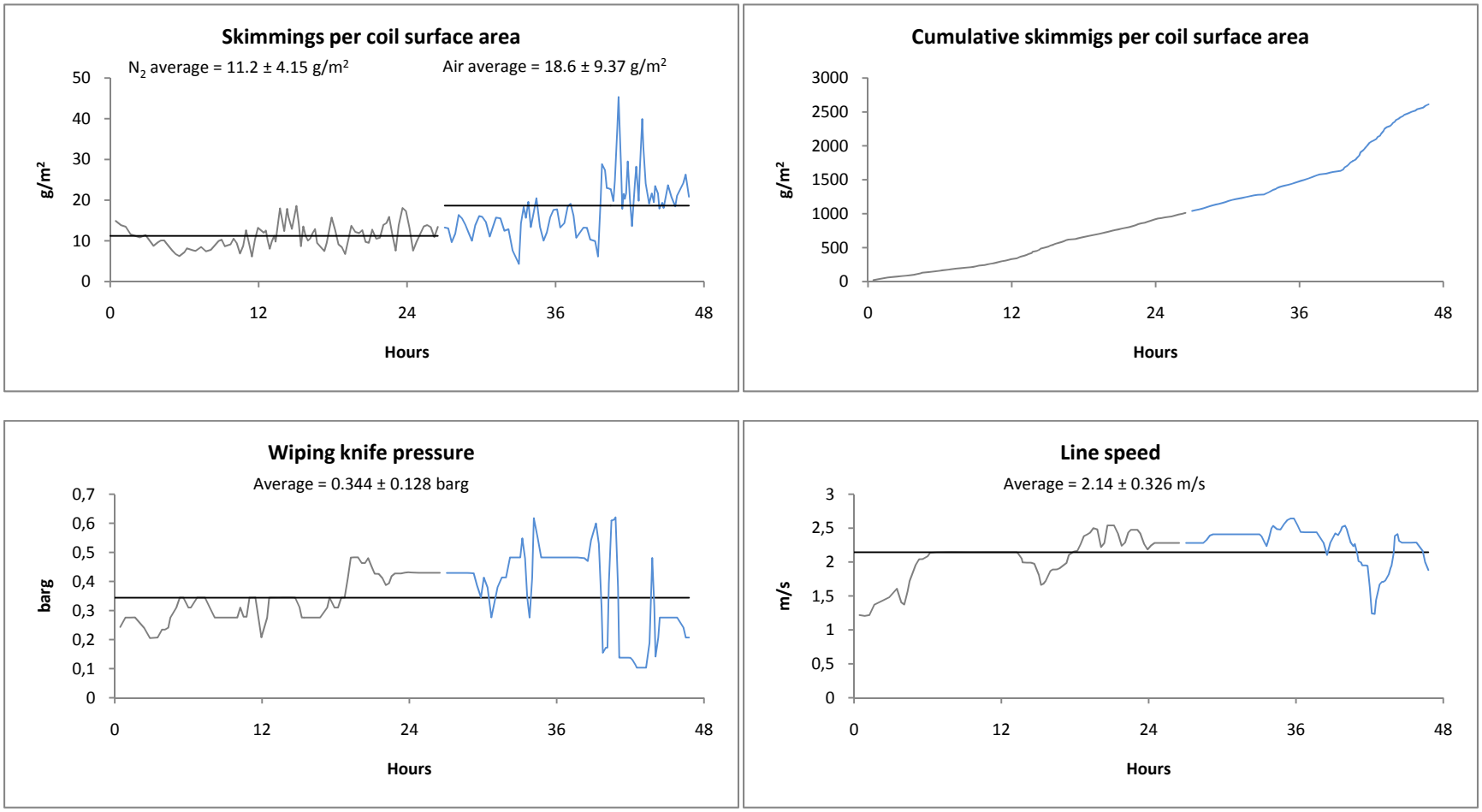

Figure 3.3-5: Operating data from ArcelorMittal Cleveland's HDGL from January 13th to January 15th 2009

The data represents two days of continuous galvanizing. After 27 hours, the process switched from N_2 wiping to air wiping. For all the figures shown above, the period in which nitrogen is used is represented by a gray curve while the period in which air is used is shown by a blue curve. **Figure 3.3.4-1** shows the skimmings per coil surface area remaining stable 13 hours into air wiping but begins to destabilize after the 40 hour mark. Clearly, air wiping has a significant effect on the amount of skimmings produced compared to N_2 wiping. The cumulative skimmings per coil surface area versus time is shown in **Figure 3.3.4-1** as well. The linear segments are the periods of time when line speed and wiping knife pressure are almost constant in time. Shifts in the curve's slope occur when there is a change in these two parameters. In the present analysis, it can be shown that skimmings formation becomes significantly more sensitive to these two parameters when an air whipping is used over N_2 wiping.

3.3.5 Normalized Operating Data

Figures 3.3.5-1, **3.3.5-2**, **3.3.5-3** and **3.3.5-4** are plots of the relative variation from the mean for skimmings per coil surface area superimposed with plots of the wiping knife pressure and the line speed. All of the data shown above was treated in this manner except for the nitrogen to air wiping transition data. To preserve clarity, all three parameters were not superimposed over one another instead the skimmings per coil area was coupled with wiping pressure and line speed separately. The data was normalized as follows:

$$\%\ deviation\ from\ the\ average = \frac{X - X_{average}}{X} \times 100\%$$

Where *"X"* is either skimmings per coil area, wiping pressure or line speed. Recall that the average values are shown in **Figures 3.3.1-1**, **3.3.1-2**, **3.3.2-1** and **3.3.2-2**. The relative variation from the mean plots shows that the skimmings per coil surface area is affected to a greater extent by the wiping pressure than the line speed. The line speed plots poorly follow the same trend as the skimmings per coil surface area plots. In fact, they only deviate slightly from the average

compared to the skimmings per coil surface area. However, the trend seen in the wiping pressure plots provides a more adequate match to that of the skimmings per coil surface area plots. When interpreting these results, it is important to realize that although the wiping pressure might be the dominating factor that influences skimmings formation, a host of other process parameters might be affecting it as well. As was just shown, the line speed had a small effect on the skimmings generated just as other process parameters such as the wiping knife height from the bath, knife to strip clearance as well as the bath size and configuration might have had a small effect as well. Finally, it is important to note that in the plots below are colour labelled. Skimmings per coil surface area is sketched in gray while the superimposed line speed and wiping pressure are sketched in red.

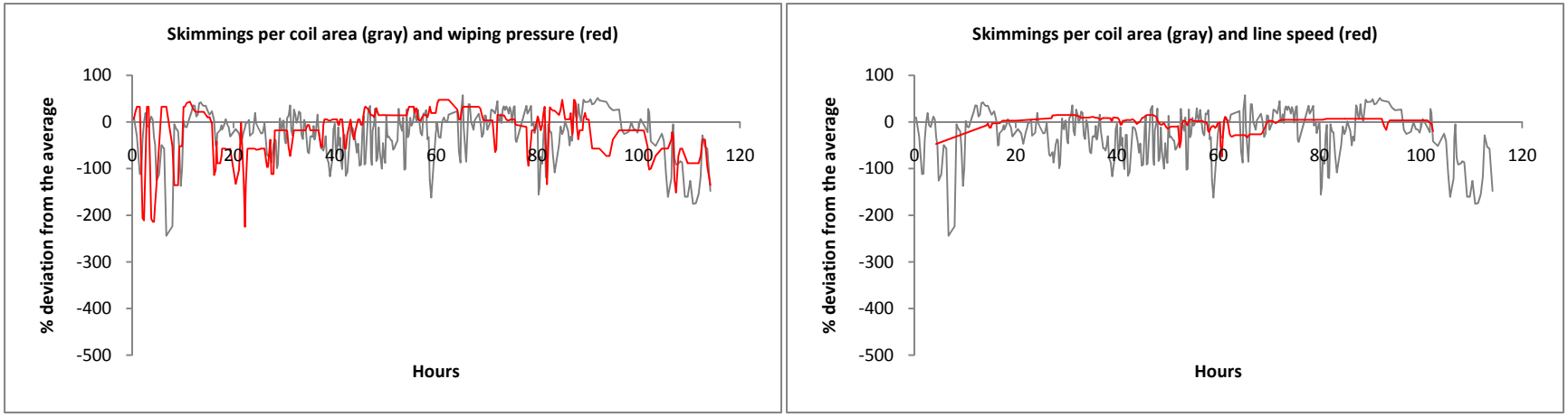

Figure 3.3-6: Relative variation from the mean of data from ArcelorMittal's HDGL from October 27th to November 1st 2008

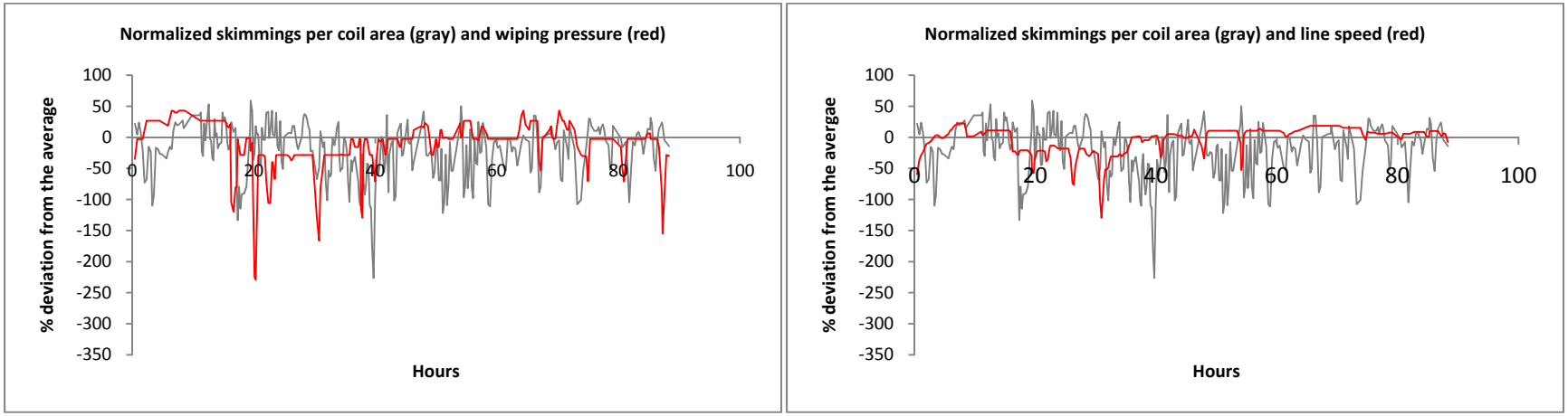

Figure 3.3-7: Relative variation from the mean of data from ArcelorMittal's HDGL from December 1st to December 4th 2008

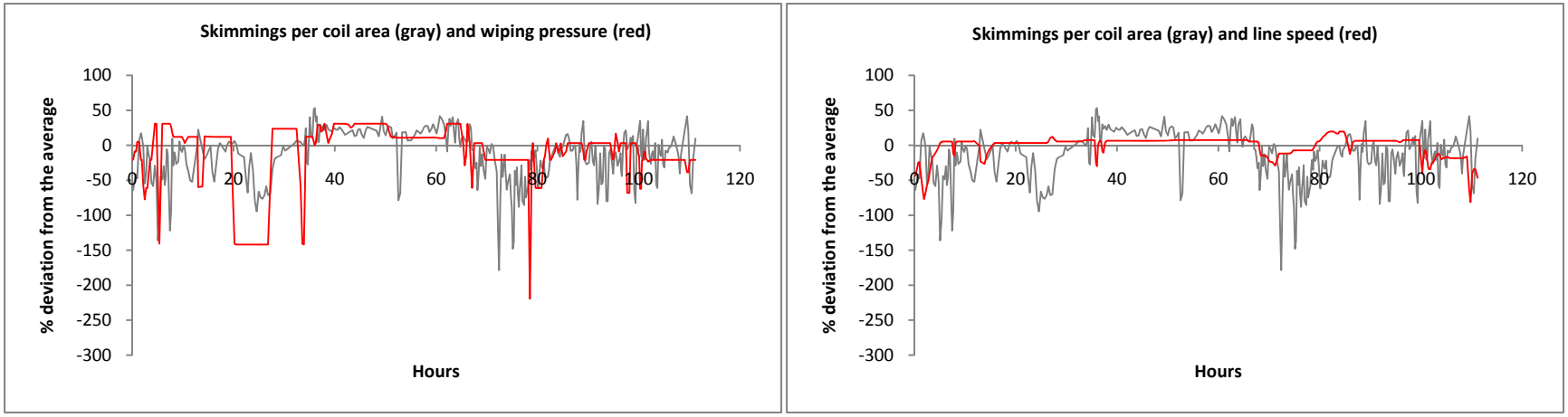

Figure 3.3-8: Relative variation from the mean of data from ArcelorMittal's HDGL from February 18th to February 22nd 2009

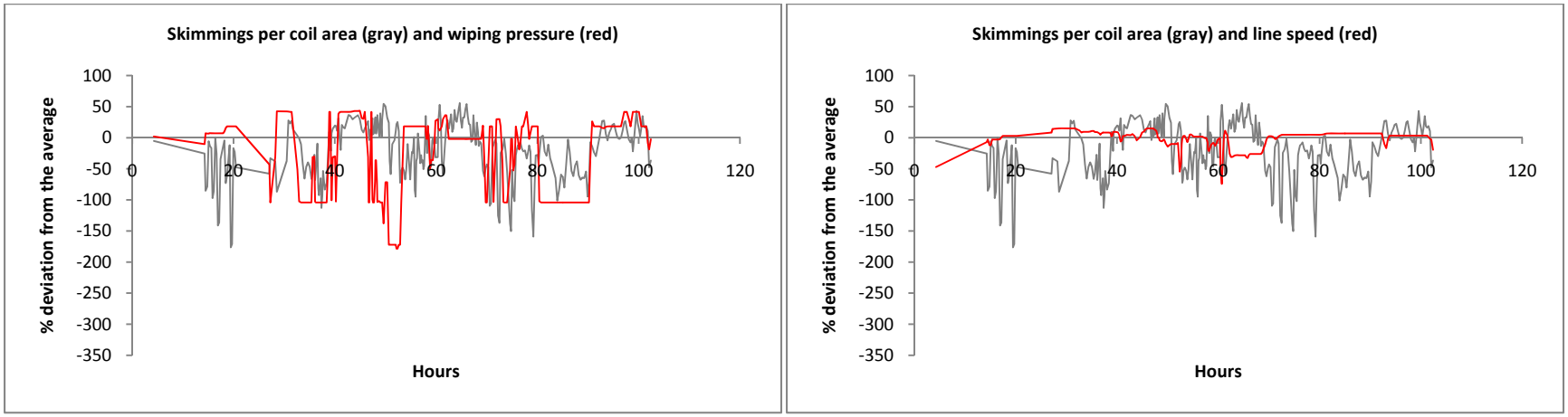

Figure 3.3-9: Relative variation from the mean of data from ArcelorMittal's HDGL from March 9th to March 14th 2009

3.4 Bench Scale Bubbling Experiments

3.4.1 Bath temperature and oxygen levels above the free liquid surface

The oxygen concentration above the bath as well as the bath temperature was monitored during both nitrogen and air bubbling campaigns and were recorded at 0 s, 10 s and 1200 s into each 20 minute experiment. Initially (t = 0 s), for both nitrogen and air bubbling experiments, the gas above the liquid free surface was ambient air. The oxygen level of the ambient air was found to be approximately 20.9 mol%. The bath temperatures and oxygen levels above the free liquid surface at 10 s and 1200 s for both nitrogen and air bubbling are shown in **Tables 6** and **7** and **Tables 8** and **9** respectively. The results in **Tables 6** and **7** show the oxygen levels near the liquid free surface are decreasing during nitrogen bubbling. Furthermore, the results from **Tables 8** and **9** indicate that oxygen is also consumed near the liquid free surface during air bubbling but to a lesser extent than nitrogen bubbling. This could be explained by the build-up of oxidized material at the liquid free surface during the experiment.

Table 6: Experimental set #1 - N_2 bubbling, temperature and O_2 concentration measurements

Run	T (t=10 s) (°C)	T (t=1200 s) (°C)	[O_2] (t=10 s) (mol%)	[O_2] (t=1200 s) (mol%)
1	451	462	7.74	6.87
2	454	463	10.20	8.39
3	451	461	10.00	9.13
4	453	462	9.36	9.16
5	450	459	11.61	10.44
6	451	460	9.27	8.85

Table 7: Experimental set #2 - N_2 bubbling, temperature and O_2 concentration measurements

Run	T (t=10 s) (°C)	T (t=1200 s) (°C)	[O_2] (t=10 s) (mol%)	[O_2] (t=1200 s) (mol%)
1	460	456	10.62	10.01
2	452	462	10.01	9.63
3	456	463	10.50	9.70
4	457	460	9.19	9.05
5	454	462	9.40	9.34
6	457	460	9.79	9.22

Table 8: Experimental set #3 - Air bubbling, temperature and O_2 concentration measurements

Run	T (t=10 s) (°C)	T (t=1200 s) (°C)	[O_2] (t=10 s) (mol%)	[O_2] (t=1200 s) (mol%)
1	457	456	20.42	20.20
2	446	460	20.45	20.17
3	453	465	20.43	20.10
4	458	460	20.41	20.17
5	447	461	20.78	20.31
6	452	462	20.46	20.17

Table 9: Experimental set #4 - Air bubbling, temperature and O_2 concentration measurements

Run	T (t=10 s) (°C)	T (t=1200 s) (°C)	[O_2] (t=10 s) (mol%)	[O_2] (t=1200 s) (mol%)
1	460	456	19.91	19.74
2	452	462	19.86	19.80
3	456	463	20.65	19.96
4	457	460	20.21	20.05
5	454	462	20.33	20.05
6	457	460	20.95	20.06

3.4.2 Skimmings generated by bubbling

The skimmings produced after 20 minutes of bubbling were collected and weighed. An average rate of skimmings generation was calculated; moreover, the fraction of initial material converted into skimmings was also calculated and is reported as a percent conversion. The average skimmings generation rates (g/s) and the conversions for each set of experiments are reported in **Tables 10**, **11**, **12**, and **13**. Moreover, the bath and skimmings masses after each experiment are shown as stacked bar charts in **Figures 3.4.2-1**, **3.4.2-2**, **3.4.2-3** and **3.4.2-4**. The average rate of skimmings generation as well as the conversion over the first set of nitrogen bubbling experiments was 0.242 g/s and 2 % respectively.

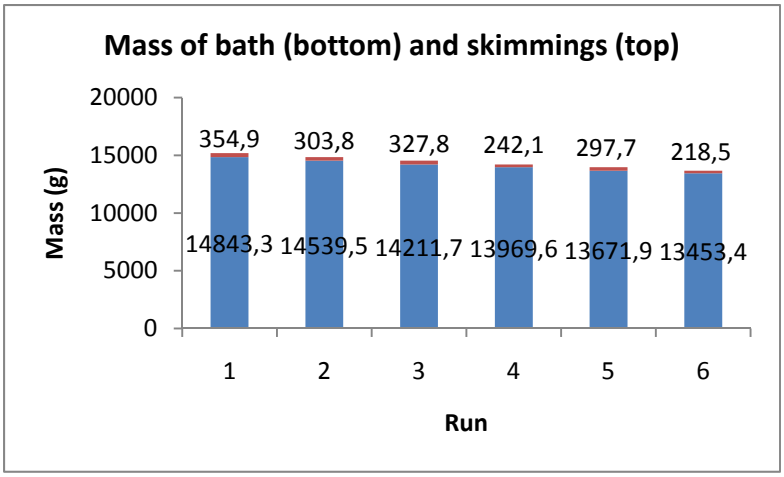

Figure 3.4-1: Experimental set #1 - N_2 bubbling, bath and skimmings masses

Table 10: Experimental set #1 - N_2 bubbling, skimmings generation rate and conversion

Run	Skimmings generation rate (g/s)	Conversion (%)
1	0.296	2.34
2	0.253	2.05
3	0.273	2.25
4	0.202	1.70
5	0.248	2.13
6	0.182	1.60

For the second set of nitrogen bubbling experiments, the average skimmings generation rate was 0.140 g/s and the average conversion was 1%. It is interesting to note that the second set of nitrogen experiments exhibited rates of skimmings formation approximately half as large as the first set. Moreover, the conversion for the second set was also half the value of the first set. There is no clear explanation as to why this occurred. It is possible that the skimmings in the first set of experiments exhibited better structural stability due to how the oxide films were imbedded in the foam mixture.

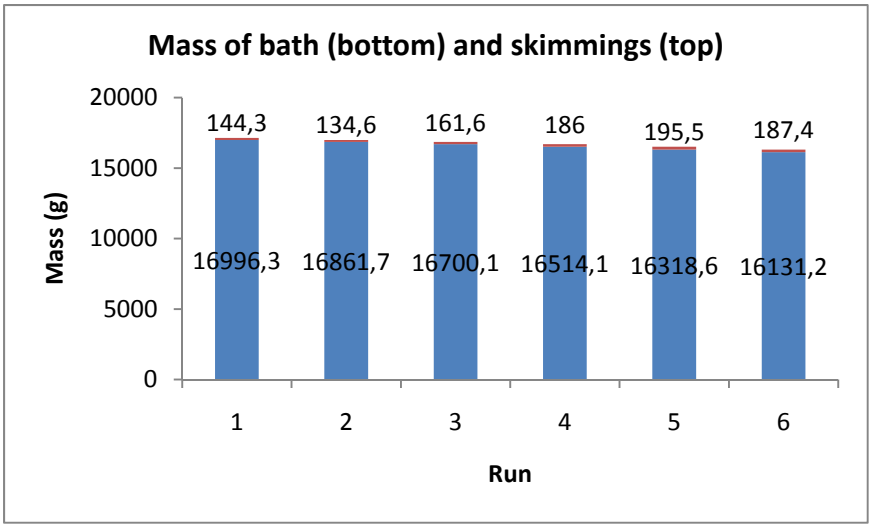

Figure 3.4-2: Experimental set #2 - N_2 bubbling, bath and skimmings masses

Table 11: Experimental set#2 - N_2 bubbling, skimmings generation rate and composition

Run	Skimmings generation rate (g/s)	Conversion (%)
1	0.120	0.84
2	0.112	0.79
3	0.135	0.96
4	0.155	1.11
5	0.163	1.18
6	0.156	1.15

Unlike the first and second set of experiments, the pair of air bubbling experiments had similar rates of skimmings generation and conversions. The third set of experiments had an average rate of skimmings generation of 0.637 g/s while the fourth set had a rate of 0.686 g/s. Furthermore, the average conversions for the third and fourth sets were 5.6% and 5.3% respectively. When comparing the results from sets #1 and #2 versus sets #3 and #4, it is clear that air bubbling produces more than twice as much skimmings than nitrogen bubbling. As mentioned before, the presence of more oxide films in skimmings can potentially stabilize its foam structure and increase its total mass over time.

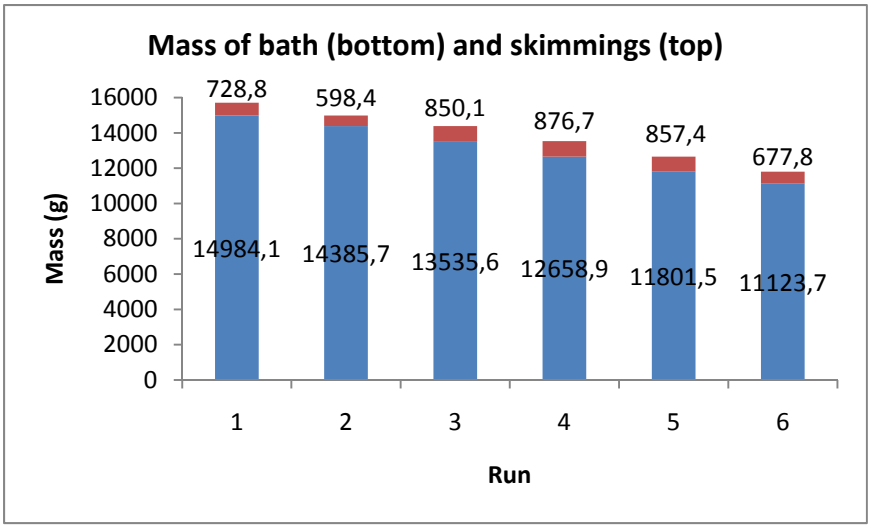

Figure 3.4-3: Experimental set #3 - Air bubbling, bath and skimmings masses

Table 12: Experimental set#3 - Air bubbling, skimmings generation rate and composition

Run	**Skimmings generation rate (g/s)**	**Conversion (%)**
1	0.607	4.64
2	0.499	3.99
3	0.708	5.91
4	0.731	6.48
5	0.715	6.77
6	0.565	5.74

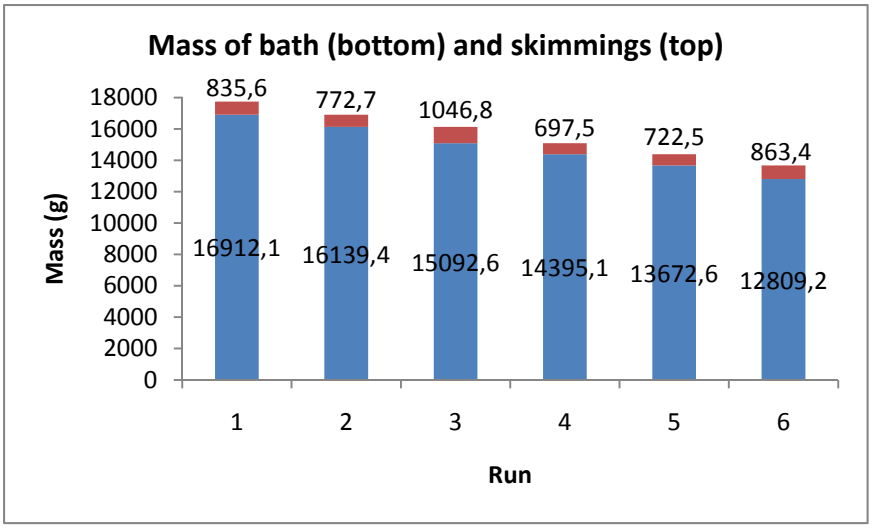

Figure 3.4-4: Experimental set #4 - Air bubbling, bath and skimmings masses

Table 13: Experimental set #4 - Air bubbling, skimmings generation rate and composition

Run	Skimmings generation rate (g/s)	Conversion (%)
1	0.696	4.71
2	0.644	4.57
3	0.872	6.49
4	0.581	4.62
5	0.602	5.02
6	0.720	6.31

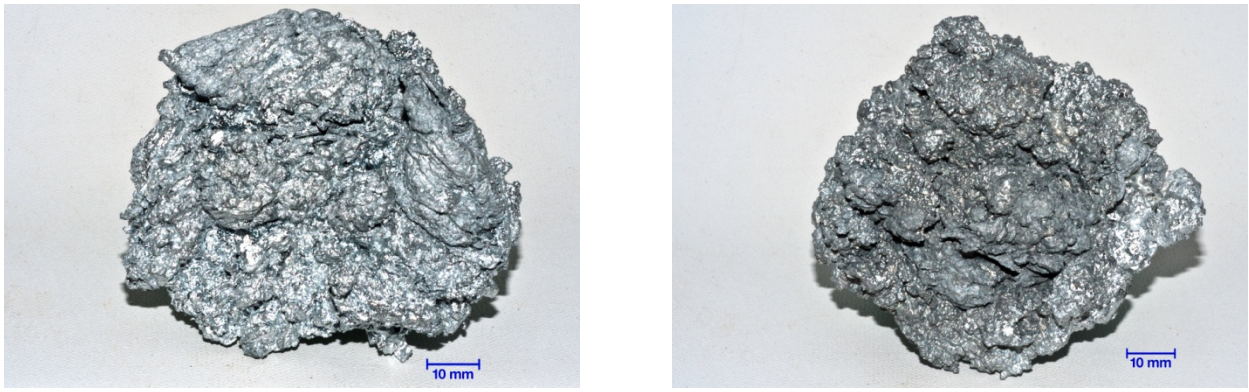

Figure 3.4-5: Samples of skimmings produced during nitrogen (left) and air (right) bubbling

Figure 3.4.2-5 displays pictures of typical skimmings samples that were produced during both air and nitrogen bubbling. The nitrogen bubbling samples maintained most of their metallic lustre whereas the air bubbling samples became darker as they contain more oxidized material.

3.4.3 Evaluating mass transfer at the liquid free surface

The average rates of aluminum and iron absorption at the liquid free surface ($N_{Al}^{surface}$ and $N_{Fe}^{surface}$) were estimated using analyzed skimmings samples from the nitrogen bubbling experiments. For this calculation, it was assumed that the difference in aluminum and iron content between the skimmings and the bath was due to oxide formation. Moreover, it is likely that the skimmings will have a higher proportion of intermetallic particles ($FeZn_{10}Al_y$ and $Fe_2Al_5Zn_x$) than the bath since the bubbles will carry them to the surface. The present calculations neglect the boost in aluminum and iron concentrations from the intermetallic particles. The results from experimental sets #1 and #2 are shown in **Tables 14** and **15**. Taking the average values of $N_{Al}^{surface}$ and $N_{Fe}^{surface}$ from **Table 14** over the six experiments yields average rates of $1.2*10^{-4}$ g/s and $3.2*10^{-5}$ g/s respectively. Similarly, the average rate of aluminum and iron absorption from **Table 15** is $9.3*10^{-5}$ g/s and $3.0*10^{-5}$ g/s correspondingly. It is clear that the rates of aluminum and iron transfer for both nitrogen bubbling experiments are comparable even though set #1 produced more skimmings than set #2.

Table 14: Experimental set #1, N_2-bubbling, free surface mass transfer of Al and Fe

Run	Time (min)	Skimmings (g)	$[Al]_{skim}$ (wt%)	$[Al]_{bath}$ (wt%)	$[Fe]_{skim}$ (wt%)	$[Fe]_{bath}$ (wt%)	$N_{Al}^{surface}$ (g/s)	$N_{Fe}^{surface}$ (g/s)
1	20	354.9	0.24	0.18	0.026	0.019	1.8*10-4	2.1*10-5
2	20	303.8	0.21	0.18	0.040	0.019	7.6*10-5	5.3*10-5
3	20	327.8	0.22	0.17	0.026	0.019	1.4*10-4	1.9*10-5
4	20	242.1	0.24	0.17	0.049	0.02	1.4*10-4	5.9*10-5
5	20	297.7	0.22	0.17	0.031	0.02	1.2*10-4	2.7*10-5
6	20	218.5	0.22	0.17	0.027	0.019	9.1*10-5	1.5*10-5

Table 15: Experimental set #2, N_2-bubbling, free surface mass transfer of Al and Fe

Run	Time (min)	Skimmings (g)	$[Al]_{skim}$ (wt%)	$[Al]_{bath}$ (wt%)	$[Fe]_{dross}$ (wt%)	$[Fe]_{bath}$ (wt%)	$N_{Al}^{surface}$ (g/s)	$N_{Fe}^{surface}$ (g/s)
1	20	144.3	0.26	0.20	0.013	0.008	7.2*10-5	6.0*10-6
2	20	134.6	0.25	0.20	0.053	0.008	5.6*10-5	5.0*10-5
3	20	161.6	0.25	0.19	0.093	0.008	8.1*10-5	1.1*10-4
4	20	186.0	0.26	0.19	0.009	0.008	1.1*10-4	1.6*10-6
5	20	195.5	0.24	0.18	0.010	0.008	9.8*10-5	3.3*10-6
6	20	187.4	0.27	0.18	0.011	0.010	1.4*10-4	1.6*10-6

3.4.4 Evaluating mass transfer across the liquid-side of the bubble interface

Again, neglecting the compositional contributions of intermetallic particles, an average rate of aluminum and iron absorption at the liquid-side of the bubble interface was estimated from the air bubbling experiments. The total rate of absorption of the elements in question (N_{Al}^{total} and N_{Fe}^{total}) is the sum of the rate at the free surface ($N_{Al}^{surface}$ and $N_{Fe}^{surface}$) and the rate at the bubble interface (N_{Al}^{bubble} and N_{Fe}^{bubble}). The average total rates of aluminum and iron absorption are reported in **Tables 16** and **17**. The average values of N_{Al}^{total} and N_{Fe}^{total} from **Table 16** are $5.1*10^{-4}$ and $2.5*10^{-4}$ g/s respectively. Likewise, the average values for of N_{Al}^{total} and N_{Fe}^{total} from **Table 17** are $5.5*10^{-4}$ and $1.7*10^{-4}$ g/s respectively. The values for the rates of aluminum and iron transfer from both sets #3 and #4 are similar.

Table 16: Experimental set #3, Air-bubbling, total mass transfer of Al and Fe

Run	Time (min)	Skimmings (g)	$[Al]_{skim}$ (wt%)	$[Al]_{bath}$ (wt%)	$[Fe]_{skim}$ (wt%)	$[Fe]_{bath}$ (wt%)	N_{Al}^{total} (g/s)	N_{Fe}^{total} (g/s)
1	20	728.8	0.29	0.19	0.069	0.021	$6.1*10^{-4}$	$2.9*10^{-4}$
2	20	598.4	0.27	0.19	0.049	0.020	$4.0*10^{-4}$	$1.4*10^{-4}$
3	20	850.1	0.26	0.19	0.042	0.020	$5.0*10^{-4}$	$1.6*10^{-4}$
4	20	876.7	0.23	0.17	0.077	0.021	$4.4*10^{-4}$	$4.1*10^{-4}$
5	20	857.4	0.26	0.18	0.044	0.020	$5.7*10^{-4}$	$1.7*10^{-4}$
6	20	677.8	0.28	0.18	0.076	0.020	$5.6*10^{-4}$	$3.2*10^{-4}$

Table 17: Experimental set #4, Air-bubbling, total mass transfer of Al and Fe

Run	Time (min)	Skimmings (g)	$[Al]_{skim}$ (wt%)	$[Al]_{bath}$ (wt%)	$[Fe]_{skim}$ (wt%)	$[Fe]_{bath}$ (wt%)	N_{Al}^{total} (g/s)	N_{Fe}^{total} (g/s)
1†	20	835.6	0.44	0.20	0.200	0.016	$1.7*10^{-3}$	$1.3*10^{-3}$
2	20	772.7	0.30	0.21	0.034	0.016	$5.8*10^{-4}$	$1.2*10^{-4}$
3	20	1046.8	0.30	0.21	0.050	0.013	$7.9*10^{-4}$	$3.2*10^{-4}$
4	20	697.5	0.27	0.20	0.026	0.016	$4.1*10^{-4}$	$5.8*10^{-5}$
5	20	722.5	0.27	0.20	0.043	0.016	$4.2*10^{-4}$	$1.6*10^{-4}$
6	20	863.4	0.28	0.20	0.044	0.016	$5.8*10^{-4}$	$2.0*10^{-4}$

† Outlier data point, therefore, was not used to estimate the average N_{Al}^{total} and N_{Fe}^{total}

The approximate values for the average rate of aluminum and iron absorption at the free surface was estimated to be $1.0*10^{-4}$ g/s and $3.0*10^{-5}$ g/s respectively. Using these values, the rate of total aluminum and iron absorption can be adjusted in order evaluate the rate of absorption by the air bubbles. Therefore, by subtracting the average $N_{Al}^{surface}$ from the average N_{Al}^{total}, the rate of absorption of aluminum by the air bubbles (N_{Al}^{bubble}) can be determined. Furthermore, if it is assumed that the liquid-side interfacial concentrations of aluminum and iron at the gas-liquid interface are zero and that the oxides produced at the surface of the bubbles do not significantly reduce the total interfacial area exposed to the liquid then the mass transfer coefficient for each species can be calculated provided that the total interfacial area of all bubbles in the system can be evaluated. These results are shown in **Tables 18** and **19**. The interfacial area associated with the bubbles was approximated using Leisbon's relationship (see Chapter 1) for submerged gas injection. The relationship assumes that the bubbles were spherical, uniformly sized and did not coalesce. Moreover, the bulk concentration of aluminum and iron in solution was calculated using the measured bath concentrations shown previously.

Table 18: Experimental set #3, Air-bubbling, mass transfer of Al and Fe from air bubbles

Run	N_{Al}^{bubble} (g/s)	N_{Fe}^{bubble} (g/s)	Total interfacial area (m^2)	$[Al]_{bulk}$ (g/m^3)	$[Fe]_{bulk}$ (g/m^3)	k_L^{Al} (m/s)	k_L^{Fe} (m/s)
1	$6.1*10^{-4}$	$2.9*10^{-4}$	$2.23*10^{-2}$	$1.24*10^{4}$	$1.37*10^{3}$	$1.8*10^{-6}$	$8.5*10^{-6}$
2	$4.0*10^{-4}$	$1.4*10^{-4}$	$2.16*10^{-2}$	$1.24*10^{4}$	$1.31*10^{3}$	$1.1*10^{-6}$	$4.1*10^{-6}$
3	$5.0*10^{-4}$	$1.6*10^{-4}$	$2.05*10^{-2}$	$1.24*10^{4}$	$1.31*10^{3}$	$1.6*10^{-6}$	$4.7*10^{-6}$
4	$4.4*10^{-4}$	$4.1*10^{-4}$	$1.90*10^{-2}$	$1.11*10^{4}$	$1.37*10^{3}$	$1.6*10^{-6}$	$1.5*10^{-5}$
5	$5.7*10^{-4}$	$1.7*10^{-4}$	$1.78*10^{-2}$	$1.18*10^{4}$	$1.31*10^{3}$	$2.3*10^{-6}$	$6.1*10^{-6}$
6	$5.6*10^{-4}$	$3.2*10^{-4}$	$1.68*10^{-2}$	$1.18*10^{4}$	$1.31*10^{3}$	$2.4*10^{-6}$	$1.3*10^{-5}$

Table 19: Experimental set #4, Air-bubbling, mass transfer of Al and Fe from air bubbles

Run	N_{Al}^{bubble} (g/s)	N_{Fe}^{bubble} (g/s)	Total interfacial area (m^2)	$[Al]_{bulk}$ (g/m^3)	$[Fe]_{bulk}$ (g/m^3)	k_L^{Al} (m/s)	k_L^{Fe} (m/s)
2	$4.8*10^{-4}$	$8.6*10^{-5}$	$2.42*10^{-2}$	$1.37*10^{4}$	$1.04*10^{3}$	$1.4*10^{-6}$	$3.4*10^{-6}$
3	$6.9*10^{-4}$	$2.9*10^{-4}$	$2.28*10^{-2}$	$1.37*10^{4}$	$8.49*10^{2}$	$2.2*10^{-6}$	$1.5*10^{-5}$
4	$3.1*10^{-4}$	$2.8*10^{-5}$	$2.16*10^{-2}$	$1.31*10^{4}$	$1.04*10^{3}$	$1.1*10^{-6}$	$1.2*10^{-6}$
5	$3.2*10^{-4}$	$1.3*10^{-4}$	$2.07*10^{-2}$	$1.31*10^{4}$	$1.04*10^{3}$	$1.2*10^{-6}$	$6.1*10^{-6}$
6	$4.8*10^{-4}$	$1.7*10^{-4}$	$1.93*10^{-2}$	$1.31*10^{4}$	$1.04*10^{3}$	$1.9*10^{-6}$	$8.5*10^{-6}$

Table 20: Experimentally determined liquid-side mass transfer coefficients

Experimental set	Average k_L^{Al} (m/s)	Average k_L^{Fe} (m/s)
#3	$1.8*10^{-6}$	$8.5*10^{-6}$
#4	$1.6*10^{-6}$	$6.9*10^{-6}$

Table 20 shows the average mass transfer coefficients for experimental sets #3 and #4. It is clear from **Table 20** that the mass transfer coefficients calculated are similar considering that both experiments began with different initial bath compositions. The detailed solution strategy for calculating the mass transfer coefficients is shown in the **Appendix 2**.

CHAPTER 4 DISCUSSION

4.1 Properly specifying a rate of skimmings generation

In section 3.2, the period in which the continuous galvanizing line at ArcelorMittal Cleveland transitioned from nitrogen to air wiping was examined and then revisited in section 3.3. The values calculated for the skimmings per coil surface area per coil residence time (section 3.2) were found to have a much larger spread over time than the calculated values for the skimmings per coil surface area (section 3.3). For example, in section 3.2, the average skimmings generation rate was 44.3 ± 25.0 g/m^2/hr for nitrogen wiping and 103 ± 83.9 g/m^2/hr for air wiping. Whereas in chapter 5, the average skimmings generation rate was11.2 ± 4.15 g/m^2 for nitrogen wiping and 18.6 ± 9.37 g/m^2 for air wiping for the same period. Using skimmings per coil surface area to specify a rate of skimmings generation resulted in a significant decrease in the variability of the computed averages. Putting it another way, 11.2 ± 37% versus 44.3 ± 56% for nitrogen wiping and 18.6 ± 50% versus 103 ± 81% for air wiping. The same can be said for the rest of the industrial data; therefore, the mass of skimmings generated per coil surface area is better at representing the specific skimmings formation of a galvanizing process than the skimmings generated per coil per coil residence time.

4.2 Skimmings generated by galvanneal (GA) and galvanize (GI) operations

In section 3.1, the amounts of skimmings produced at the ArcelorMittal Cleveland line for both galvanneal and galvanize operations were examined. The analysis showed that for similar line speed and wiping pressure, the GI bath produced more skimmings than the GA bath. In fact, the GI bath produced 38% more skimmings per unit time over the one day period that the data was collected. A similar trend was detected at the bench scale as well. At low rotation rates, both GA and GI solutions produced similar amounts of skimmings per unit time. On the other hand, the GI solution produced 51% more skimmings per unit time at the medium rotation rate and 143% more skimmings per unit time at the high rotation rate. It is important to note that both the industrial and experimental skimmings where produced under nitrogen gas. There is very little literature addressing the effect of bath composition on the rate of skimmings generation other

than what is presented in this work. Therefore, a consensus on this particular issue does not exist. The author can simply speculate that two factors contribute to stabilizing the foam structure of skimmings produced in a GI bath: the presence of more top dross particles and aluminum oxide due to higher aluminum levels in the liquid.

4.3 Skimmings generated for air wiping and nitrogen wiping

In section 3.3, it was shown that using air wiping produces more skimmings than using nitrogen wiping. The same result was obtained experimentally in section 3.2. When the industrial data for air and nitrogen wiping is compared for similar bath compositions, line speeds and wiping pressures, the continuous galvanizing line at ArcelorMittal Cleveland produced 9.6 % more skimmings per coil surface area when air wiping was used. Moreover, it was found that wiping pressure was the dominant parameter which influenced the amount of skimmings produced per coil surface area. As for the experimental data, it was found that using an air jet produced 10.5 times as much skimmings per unit time compared to using a nitrogen jet. Again, this can potentially be explained by the effect the oxide films have on the stability of the skimmings foam structure. In addition, the rate of skimmings generation increased with rotation rate and, consequently, the liquid free surface.

4.4 Skimmings characterization

As shown in chapter 1, the skimmings analysed by Thiounn et al. [23] was similar in morphology to the industrial skimmings examined in section 3.1. Both industrial samples contained dross particles, oxides and an appreciable amount of porosities. However, Thiounn et al. did not go as far as to investigate the elemental distribution of their skimmings samples. In section 3.1, polished samples of industrial skimmings were analyzed for their elemental distributions using dispersive X-ray mapping. The technique provides a qualitative as opposed to a quantitative analysis of the materials chemical composition. The series of images clearly identify the crystalline $Fe_2Al_5Zn_x$ and $FeZn_{10}Al_y$ particles as well as the oxide films. Therefore, this technique

proved to be effective at indentifying the various intermetallic particles that are present in a galvanizing bath. In section 3.2, the skimmings produced at the bench scale showed similar characteristics as those produced in industry. The bench scale results contained top and bottom dross, porosities as well as oxides of zinc, aluminum and iron. Moreover, the lab results showed clearly defined oxide envelops with liquid zinc alloy trapped within them. Industrial skimmings do not show any appreciable amounts of oxide envelops since they have likely collapsed into films due to skimmings being partially drained of liquid zinc as they build up along the pot walls. The lab samples were gathered over a short period of time and immediately quenched. Therefore, the oxide envelops in the lab samples did not have enough time to collapse and where quickly frozen in place. The technique used to analyze the chemical composition of the skimmings produced in the lab was atomic absorption spectrophotometry. Since aluminum and iron are present in such small amounts in galvanizing liquids, the accuracy of the technique may be poor. The aluminum and iron content of the skimmings produced in the lab ranged between 0.14 wt% to 0.34 wt% and 0.04 wt% to 0.194 wt% respectively. While those analyzed by Thiounn et al. had aluminum levels between 0.4 wt% and 1 wt% and iron levels between 0.02 wt% and 1 wt%.

4.5 Mass transfer coefficients

Mass transfer coefficients for the liquid side transport of aluminum and iron were evaluated in section 3.4. These values were of the same order of magnitude as those found in text books that treat the subject of liquid metal-gas transport [30], [31], [32], [33]. Therefore, the method used for evaluating the mass transfer coefficients was successful.

CONCLUSION

A statistical analysis of the process data provided by ArcelorMittal Cleveland's HDGL gave way to the following conclusions:

1. Two operating parameters were found to critically affect the amount of skimmings that are produced in the continuous hot-dip galvanizing process: wiping knife pressure and line speed. Wiping knife pressure was found to have a greater effect than line speed on the amount of skimmings produced per coil surface area.

2. The type of gas used for the wiping knives system was found to strongly influence the amount of skimmings produced per coil surface area. Air wiping produced significantly more skimmings per coil than nitrogen wiping.

3. The galvanizing bath composition was found to have an effect on the amount of skimmings produced per coil surface area. Galvanizing (GI) produced more skimmings per coated coil than galvannealing (GA).

4. The rate of skimmings produced per coil surface area observed during nitrogen wiping was found to remain stable well into the transition to air wiping. However, after approximately half a day into the transition from nitrogen wiping, the rate of skimmings produced per coil increased to levels accustomed to air wiping.

An investigation into the morphology and composition of the industrial skimmings samples provided by ArcelorMittal Cleveland and U.S. Steel Hamilton led to the following conclusion:

5. Energy dispersive X-ray analysis and elemental mapping proved to be a very effective method of identifying the composition and elemental distribution of the skimmings

samples. The analysis also indicated a very heterogeneous porous mixture of intermetallic particles of either or both $Fe_2Al_5Zn_x$ and $FeZn_{10}Al_y$ and an agglomeration of oxide films of zinc, aluminum and iron oxides in a liquid zinc matrix.

A bench scale experiment which attempted to simulate skimmings formation at the strip exit region of a galvanizing bath using a shrouded crucible loaded with liquid zinc, a steel impeller for agitation and an impinging jet of gas indicated the following:

6. An imaging analysis of the experimental data showed that the skimmings produced at the bench scale were similar in morphology to those of the ArcelorMittal Cleveland and U.S.Steel Hamilton galvanizing lines. The samples were heterogeneous mixtures of bath solution, intermetallic particles of top and bottom dross and zinc, aluminum and iron oxide films.

7. The experiments showed that skimmings generation increased with bath agitation. GI alloys also produced more skimmings than GA alloys for all mixing rates and more skimmings were produced when an air jet was used compared to a nitrogen jet. Moreover, shrouding the crucible contributed to reducing the amount of skimmings formed. This is particularly clear when comparing the two cases of a shrouded crucible under a nitrogen jet and an open crucible under an air jet.

A second bench scale experiment was conducted which attempted to simulate the mass transfer between the return zinc flow from the wiping knives and the surrounding atmosphere near the strip exit region of a galvanizing bath. This was accomplished by top submerging a jet of air into a crucible loaded with liquid zinc and the following conclusion was made:

8. The methodology used to evaluate the liquid side mass transfer coefficients for aluminum and iron produced results which compared favourably with those found in the literature. Therefore, the assumption that the correlations for bubble flow in water can be applied to liquid metals was satisfactory and the method used to estimate the interfacial area of all bubbles in solution was also reasonable.

REFERENCES

[1] International Zinc Association website: www.iza.com

[2] F.E. Goodwin, E.A. Silva, "An Overview of North American Zinc-Based Sheet Steel Coatings and Production: Status and Opportunities," GALVATECH'07 Proceedings, November 2007, pp. 6-13

[3] D. Shim, M. Lee, "New CGL of POSCO-MEXICO," Asia Pacific Galvanizing Conference, October 2009

[4] Galvinfo Center website: www.galvinfo.com

[5] F. Ajersch, C. Binet, F.E. Goodwin, K.S. Turke, P.S. Kolisnyk, "Validation Studies of the Numerical Simulation of Flow in the Bethlehem Steel, Burns Harbor Galvanizing Bath," GALVATECH'98 Proceedings, September 1998, pp. 642-647

[6] C. Heitz, "Coating Weight Control and Automatic Wiping at ARCELOR-Sollac Atlantique Continuous Galvanizing Line," 94th Galvanizers Association Meeting Proceedings, October 2002

[7] W. Maschek, S.P. Hayes, A.R. Marder, "Cross Sectional Studies of Zinc Iron Phase Growth in an Environmental Scanning Electron Microscope," GALVATECH'95 Proceedings, September 1995, pp. 309-318

[8] J. Nakano, G.R. Purdy, D.V, Malakhov, "Modeling of intermetallic formation in hot-dip galvanizing," XXXI CALPHAD Meeting Proceedings, May 2002

[9] N.-Y. Tang, "Modeling Al Enrichment in Galvanizing Coatings," Metallurgical and Materials Transactions A, July 1995, Volume 26A, pp.1699-1704

[10] M.-L. Giorgi, J-B. Guillot, R. Nicolle, "Modeling of the Kinetics of Galvanizing Reactions," GALVATECH'04 Proceedings, April 2004, pp. 703-712

[11] P.Toussaint, L.Segers, R. Winand, M. Dubois, "Experimental Study and Mathematical Modeling of Zinc Ingot Melting in Continuous Hot-Dip Galvanizing Process," Ironmaking and Steelmaking, December 1995, Volume 22, pp.171-176

[12] N.-Y. Tang, "Determination of Liquid-Phase Boundaries in Zn-Fe-Mx Systems," Journal of Phase Equilibria and Diffusion, 2000, Volume 21, Number 1, pp. 70-77

[13] J. Nakano, G.R. Purdy, D.V, Malakhov, "Thermodynamic Aspects of Dross Generation," GALVATECH'07 Proceeding, November 2007, pp. 135-140

[14] J.R. McDermid, M.H. Kaye, W.T. Thompson, "Fe Solubility in the Zn-Rich Corner of the Zn-Al-Fe System for Use in Continuous Galvanizing and Galvannealing," Metallurgical and Materials Transactions B, April 2007, Volume 38B, pp.215-230

[15] J. Nakano, D.V. Malakhov, S. Yamaguchi, G.R. Purdy, "A Full Thermodynamic Optimization of the Zn-Fe-Al System within the 420-500 °C Temperature Range," Computer Coupling of Phase Diagrams and Thermochemistry, 2007, Volume 31, pp.125-140

[16] M. Gagné, A. Paré, F. Ajersch, "Water Modeling of a Continuous Galvanizing Bath" 84th Galvanizers Association Meeting Proceedings, October 1992, pp. 147-163

[17] F. Ajersch, F. Ilinca, M. Perrault, A. Malo, J.-F. Hétu, "Numerical Analysis of the Effect of Operating Parameters on the Flow in a Continuous Galvanizing Bath," GALVATECH'01 Proceedings, June 2001, pp. 511-518

[18] F. Ajersch, F. Ilinca, J.-F. Hétu, "Simulation of the Flow in a Continuous Galvanizing Bath: Part I. Thermal Effects of Ingot Addition," Metallurgical and Materials Transactions B, February 2004, pp. 161-170

[19] F. Ajersch, F. Ilinca, J.-F. Hétu, "Simulation of the Flow in a Continuous Galvanizing Bath: Part II. Transient Aluminum Distribution Resulting from Ingot Addition," Metallurgical and Materials Transactions B, February 2004, pp. 171-178

[20] L. Ouellet, F. Ajersch, F. Ilinca, "Numerical Simulation and Validation of Flow in a Galvanizing Bath Using a Water Model," GALVATECH'04 Proceedings, April 2004, pp. 917-926

[21] F. Ajersch, F. Ilinca, M. Sabsabi, L. St. Onge, R. Héon, T.A.E. Cormode, N.-T. Tang, C. Baril, M. Gagné, F.E. Goodwin, "Monitoring of Al and Fe Content and Numerical Simulation of the Serevco Galvanizing Bath During GA and GI Transition," 94th Galvanizers Association Meeting Proceedings, October 2005

[22] E. Baril, L. St. Onge, M. Sabsabi, J.M. Lucas, "Novel Method for On-Line Chemical Analysis of Continuous Galvanizing Baths," GALVATECH'04 Proceedings, April 2004, pp. 1095-1104

[23] R. Thiounn, R. Zanfack, H. Saint-Raymond, P. Durighello, "Understanding Hot-dip Galvanizing Skimmings," 100th Galvanizers Association Meeting Proceedings, October 2008

[24] S. Hesling, K. Hochsteller, G. Voss, G. Wallace, "Integration of Coating Mass Control with Bath and Galvanneal Furnace Management," 93rd Galvanizers Association Meeting Proceedings, September 2001

[25] W.G. Davenport, A.V. Bradshaw, R. Richardson, "Behaviour of Spherical-Cap Bubbles in Liquids Metals," Journal of Iron and Steel Institue, 1967, Volume 205, pp. 1034-1042

[26] M. Panenis, N.G. Davenport, "Dynamics of Bubbles in Liquid Metals: Two Dimensional Experiments," Transactions TMS-AIME, 1969, Volume 145, pp. 735-738

[27] I. Leibson, E.G. Holcomb, A.G. Cacoso, J.J. Jasmic, "Rate of Flow and Mechanics of Bubble Formation from Single Submerged Orifices: Part I Rate of Flow Studies," American Institute of Chemical Engineers, September 1956, Volume 2, pp. 296-300

[28] R.M. Davies, G. Taylor, "The Mechanics of Large Bubble Rising through Extended Liquids and though Liquids in Tubes," Royal Society of London Proceedings, 1950, Volume 200A, pp. 375-390

[29] R. Collins, "The Cycloidal-Cap Bubble: A Neglected Solution in the Theory of Large Plane Gas Bubbles in Liquids," Chemical Engineering Science, February 1967, Volume 22, pp. 89-97

[30] H.S. Ray, "Kinetics of Metallurgical Reactions," New York: International Science Publisher, 1993

[31] R.I.L Guthrie, "Engineering in Process Metallurgy," New York: Oxford University Press, 1989

[32] H.S. Fogler, "Elements of Chemical Reaction Engineering," 4th edition, Westford: Prentice Hall Professional Technical Reference, 2005

[33] R.B. Bird, W.E. Stewart, E.N. Lightfoot, “Transport Phenomena” 2nd edition, New York: John Wiley & Sons, 2007

APPENDIX 1 – DATA ANALYSIS OF PROCESS PARAMETERS

The approach for the analysis of industrial data mentioned in chapter 2 is shown here. Investigating which process parameters have the greatest influence on dross formation in the zinc bath begins with first comparing the air knife position above the melted zinc pot and the type of wiping gas (air or nitrogen) used in the process. The analysis pointed to two conclusions. First, the average rate of dross formation is not heavily influenced by the air knife position above the pot. Second, more dross per unit time is formed when the wiping gas is air.

The next step is to determine which other process parameters heavily influence dross formation. From experience, it is assumed that these other parameters are line speed, air knife pressure, coating deposition rate and bath Al content. The analysis of the average rate of dross formation with respect to these four variables confirms that the most important process parameters are line speed, air knife pressure and deposition rate.

Comparing between high and low air knife positions above the liquid zinc

The data shows large differences in air knife position while the process operates with a nitrogen wiping gas. A hypothesis test is carried out to compare the means of the average dross formation rates between high and low air knife positions during plant operation.

STEP 1: Inference on the variances

Hypothesis test:

1) σ_1^2= variance of average dross formation rate for “high” air knife position above pot

   σ_2^2 =variance of average dross formation rate for “low” air knife position above pot

2) Assume that the average dross formation rate is a normal random variable for both “high” and “low” air knife positions.

3) Null hypothesis: $\sigma_1^2 = \sigma_2$

   Alternative hypothesis: $\sigma_1^2 \neq \sigma_2^2$

4) Probability of wrongfully rejecting the null hypothesis “α “= 0.05

5) Reject null hypothesis if $F_{statistic} > F_{critical}$

6) Excel output:

F-Test Two-Sample for Variances (α=0.05)

	Average skimmings formation rate (kg/min) for high air knife position	*Average skimmings formation rate (kg/min) for low air knife position*
Sample Mean	2.203855647	2.124319865
Sample Variance	1.08571819	0.761860478
Observations	1029	92
DOF	1028	91
F statistic	1.425087955	
P(F<=f) one-tail	0.016350274	
F Critical one-tail	1.311715181	

7) Conclusion: Since $F_{statistic} > F_{critical}$ then the null hypothesis is rejected. Therefore, there is evidence to conclude that the variance of the average dross formation rate for a high air knife position is different from the variance of the average skimmings formation rate for a low air knife position.

STEP 2: Inference on the means

Hypothesis test:

1) μ_1=mean of average dross formation rate for "high" air knife position above pot

   μ_2=mean of average dross formation rate for "low" air knife position above pot

2) Assume that the average dross formation rate is a normal random variable for both "high" and "low" air knife positions.

3) Null hypothesis: $\mu_1 = \mu_2$

   Alternative hypothesis: $\mu_1 \neq \mu_2$

4) Probability of wrongfully rejecting the null hypothesis "α "= 0.05

5) Reject null hypothesis: if $t_{statistic} > t_{critical}$ for positive $t_{statistic}$ and if $t_{statistic} < -t_{critical}$ for negative $t_{statistic}$

6) Excel output:

t-Test: Two-Sample Assuming Unequal Variances (α=0.05)

	Average skimmings formation rate (kg/min) for high air knife position	*Average skimmings formation rate (kg/min) for low air knife position*
Sample Mean	2.203855647	2.124319865
Sample Variance	1.08571819	0.761860478
Observations	1029	92
Mean Difference	0	
DOF	116	
t statistic	0.823146628	
P(T<=t) two-tail	0.412113649	
t Critical two-tail	1.980624802	

7) Conclusion: Since $t_{statistic} < t_{critical}$ then the null hypothesis is not rejected. Therefore, there is insufficient evidence to conclude that the mean average dross formation rate for a high air knife position is different from the mean average dross formation rate for a low air knife position.

Comparing between air and nitrogen wiping gas

A hypothesis test is carried out to compare the means of the average dross formation rates during air wiping and pure nitrogen wiping of the coated steel sheets.

STEP 1: Inference on the variances

Hypothesis test:

1) σ_1^2=variance of average dross formation rate for using "pure nitrogen" as a wiping gas

   σ_2^2=variance of average dross formation rate for using "air" as a wiping gas

2) Assume that the average dross formation rate is a normal random variable during both "pure nitrogen" and "air" wiping of the coated steel sheets.

3) Null hypothesis: $\sigma_1^2 = \sigma_2^2$

Alternative hypothesis: $\sigma_1^2 \neq \sigma_2^2$

4) Probability of wrongfully rejecting the null hypothesis "α "= 0.05

5) Reject null hypothesis: if $F_{statistic} > F_{critica}$

6) Excel output:

F-Test Two-Sample for Variances (α=0.05)

	Average skimmings formation rate (kg/min) during nitrogen wiping	*Average skimmings formation rate (kg/min) during air wiping*
Sample Mean	2.197328179	2.288085241
Sample Variance	1.058912345	0.85881275
Observations	1121	1230
DOF	1120	1229
F	1.232995603	
P(F<=f) one-tail	0.000166753	
F Critical one-tail	1.100769254	

7) Conclusion: Since $F_{statistic} > F_{critical}$ then the null hypothesis is rejected. Therefore, there is evidence to conclude that the variance of the average dross formation rate while using pure nitrogen as a wiping gas is different from the variance of the average dross formation rate while using air as a wiping gas.

STEP 2: Inference on the means

Hypothesis test:

1) μ_1=mean of average dross formation rate for "high" air knife position above pot

μ_2=mean of average dross formation rate for "low" air knife position above pot

2) Assume that the average dross formation rate is a normal random variable during both "pure nitrogen" and "air" wiping of the coated steel sheets.

3) Null hypothesis: $\mu_1 = \mu_2$

Alternative hypothesis: $\mu_1 \neq \mu_2$

4) Probability of wrongfully rejecting the null hypothesis "α "= 0.05

5) Reject null hypothesis: if $t_{statistic} > t_{critical}$ for positive $t_{statistic}$ and if $t_{statistic} < -t_{critical}$ for negative $t_{statistic}$

6) Excel output:

t-Test: Two-Sample Assuming Unequal Variances (α=0.05)

	Average skimmings formation rate (kg/min) during nitrogen wiping	*Average skimmings formation rate (kg/min) during air wiping*
Sample Mean	2.197328179	2.288085241
Sample Variance	1.058912345	0.85881275
Observations	1121	1230
Mean Difference	0	
DOF	2262	
t statistic	-2.239150855	
P(T<=t) two-tail	0.025242954	
t Critical two-tail	1.961011549	

7) Conclusion: Since $t_{statistic} < -t_{critical}$ then the null hypothesis is rejected. Therefore, there is evidence to conclude that the mean average dross formation rate while using pure nitrogen as a wiping gas is different from the mean average dross formation rate while using air as a wiping gas.

Discriminating between process parameters with the greatest influence on the average rate of skimmings generation

Multiple linear regression was used to screen candidate process variables to obtain a model that contains the most influential regressor variables. Four candidate variables were chosen from previous experience and underlying theoretical considerations: Al content in the bath (wt%), absolute air knife pressure (kPa), line speed (m/s) and coating deposition rate (g/m^2). First order polynomial models for both nitrogen and air wiping operating data were generated using a level of significance α = 0.10. Two variable selection techniques were used to model the response average dross formation rate (kg/min) in this analysis and they are described below:

Backward Elimination:

The backward elimination algorithm begins will all candidate regressors in the model. Then the regressor with the largest p-value is deleted if this p-value is larger than α. Next, a new model is fit with the remaining regressors. If omission of the "insignificant" regressor results in an increase of the $R^2_{adjusted}$ then the new model is retained and the next regressor for potential elimination is found. The algorithm terminates when no further regressor can be deleted or in other words, when there is no further increase in $R^2_{adjusted}$.

Forward Selection:

The forward selection procedure is based on the principal that regressors should be added to the model one at a time until there are no remaining candidate regressors that produce an increase in the $R^2_{adjusted}$. That is, variables are added one at a time as long as their p-values are less than α.

Backward elimination & Forward Selection (α = 0.10) – Air wiping

Rigorous procedures are not shown. The results are similar to the ones obtain for the nitrogen wiping.

Conclusion: The most influential parameters are air knife pressure, deposition rate and line speed.

Backward elimination (α = 0.10) – Nitrogen wiping

STEP 1: All candidates

Regression Statistics	
R^2	0.19945401
$R^2_{adjusted}$	0.196584669
Observations	1121

	Coefficients	*Standard Error*	*P-value*
Intercept	-2.036456562	0.40916506	7.47E-07
Al content (%)	-0.034552423	0.20345882	0.865178
Air knife pressure (kPa)	0.013629268	0.00305619	9.04E-06
Deposition rate (g/m^2)	0.026381025	0.00356103	2.52E-13
Line speed (m/s)	0.954409908	0.0766655	2.09E-33

STEP 2: Removing Al content

Regression Statistics	
R^2	0.199433321
$R^2_{adjusted}$	0.197283187
Observations	1121

	Coefficients	*Standard Error*	*P-value*
Intercept	-2.043588255	0.40682736	5.91E-07
Air knife pressure (kPa)	0.013663635	0.00304816	8.13E-06
Deposition rate (g/m^2)	0.026346698	0.00355374	2.42E-13
Line speed (m/s)	0.952983494	0.07617087	1.05E-33

Conclusion: The most influential parameters are air knife pressure, deposition rate and line speed.

Forward Selection (α = 0.10) – Nitrogen wiping

STEP 1: Best start point

Line speed (m/s)

Regression Statistics	
$R^2_{adjusted}$	0.158975501

	Coefficients	*Standard Error*	*P-value*
Intercept	0.166144561	0.142093092	0.24254565
Line speed (m/s)	0.967320184	0.066324989	3.0698E-44

Air knife pressure (kPa)

Regression Statistics	
$R^2_{adjusted}$	0.049790926

	Coefficients	*Standard Error*	*P-value*
Intercept	-0.30931798	0.325831689	0.34266373
Air knife pressure (kPa)	0.01850165	0.002394788	2.4602E-14

Deposition rate (g/m^2)

Regression Statistics	
$R^2_{adjusted}$	-0.000536667

	Coefficients	*Standard Error*	*P-value*
Intercept	2.167686698	0.056087073	2.858E-208
Deposition rate (g/m^2)	0.002009372	0.003180057	0.52760301

Al content (%)

Regression Statistics	
$R^2_{adjusted}$	-0.000129793

	Coefficients	*Standard Error*	*P-value*
Intercept	2.161374397	0.049570705	1.677E-243
Al content (%)	0.207842448	0.224822603	0.35543936

STEP #2: Retain line speed

Deposition rate (g/m^2)

Regression Statistics	
$R^2_{adjusted}$	0.1835741

	Coefficients	*Standard Error*	*P-value*
Intercept	-0.3795671	0.167864114	0.023941
Deposition rate (g/m^2)	0.0179208	0.003041583	5.05E-09
Line speed (m/s)	1.101309	0.069191719	1.43E-51

Air knife pressure (kPa)

Regression Statistics	
$R^2_{adjusted}$	0.1585372

	Coefficients	*Standard Error*	*P-value*
Intercept	-0.0100644	0.307621736	0.973906
Air knife pressure (kPa)	0.0017107	0.00264856	0.518488
Line speed (m/s)	0.940863	0.077969573	1.32E-31

Al content (%)

Regression Statistics	
$R^2_{adjusted}$	0.1582452

	Coefficients	*Standard Error*	*P-value*
Intercept	0.1614052	0.144833198	0.265338
Al content (%)	0.035316	0.206595868	0.8643
Line speed (m/s)	0.9666678	0.066463423	5.07E-44

STEP #3: Retain deposition rate

Air knife pressure (kPa)			
Regression Statistics			
$R^2_{adjusted}$	0.197283187		
	Coefficients	*Standard Error*	*P-value*
Intercept	-2.043588255	0.406827356	5.91E-07
Air knife pressure (kPa)	0.013663635	0.003048156	8.13E-06
Deposition rate (g/m^2)	0.026346698	0.003553744	2.42E-13
Line speed (m/s)	0.952983494	0.076170873	1.05E-33

Al content (%)			
Regression Statistics			
$R^2_{adjusted}$	0.182999473		
	Coefficients	*Standard Error*	*P-value*
Intercept	-0.371497796	0.168828085	0.027979
Al content (%)	-0.094632957	0.204721489	0.643991
Deposition rate (g/m^2)	0.018072901	0.003060383	4.66E-09
Line speed (m/s)	1.104193892	0.069496859	2.1E-51

Conclusion: The most influential parameters are air knife pressure, deposition rate and line speed.

APPENDIX 2 – MASS TRANSFER CALCULATIONS

The solution strategy for obtaining the liquid-side mass transfer coefficients for both aluminum and iron discussed in chapter 5 is shown here.

Calculating the bubble diameter and rising velocity

1) Average gas velocity at the orifice:

→Assume an ideal gas at the same temperature as the melt

$$v = \frac{Q}{A_o}$$

Q ≡ volumetric gas flow rate

A_o ≡ orifice cross-sectional area

2) Reynolds number at the orifice:

→Assume the gases (Air and N_2) have constant properties

$$Re_o = \frac{\rho_g \, v \, d_o}{\mu_g}$$

ρ_g ≡ density of the gas at 460°C (Air: 0.480 kg/m^3, N_2: 0.465 kg/m^3)

μ_g ≡ viscosity of the gas 460°C (Air: 3.52*10^{-5} Pa s, N_2: 3.35*10^{-5} Pa s)

v ≡ average gas velocity at the orifice

d_o ≡ orifice diameter

3) Bubble diameter:

→Assume Leibson's relationship applies to bubble flow in liquid metals

Laminar ($Re_o \leq 2000$): $d_b = 0.287\, d_o^{1/2}\, Re_o^{1/3}$

Turbulent ($Re_o \geq 10000$): $d_b = 0.71\, Re_o^{-1/20}$

4) Bubble rising velocity:

→Assume Collins' relationship applies to bubbles rising in liquid metals

$$U_\infty = \frac{1}{2}\sqrt{g\, r_b}$$

g ≡ gravity constant and

r_b ≡ bubble radius

Calculating the bubble residence time

5) Height of the melt in the crucible:

→Assume the melt is pure zinc and that it has constant properties

$$h = \frac{V}{A} = \frac{m/\rho_{Zn}}{A}$$

V ≡ melt volume

A ≡ cross-sectional area of the crucible

m ≡ melt mass

ρ_{Zn} ≡ liquid zinc density at 460°C (6530 kg/m^3)

6) Bubble residence time:

$$\tau_b = \frac{h}{U_\infty}$$

Calculating the interfacial area between the bubbles and the melt

7) Bubble volume and surface area:

→Assume the bubbles are spherical

$$V_b = \frac{4}{3}\,\pi\, r_b^3$$

$$A_b = 4\,\pi\, r_b^2$$

8) Number of bubbles in the melt at any time:

→Assume the bubbles do not coalesce

$$n_b = \frac{Q\,\tau_b}{V_b}$$

9) Bubble-melt interfacial area:

$$a = A_b\, n_b$$

Calculating the mass transfer coefficients for Al and Fe

10) Nitrogen bubbling experiments-Rate of solute consumption (Al, Fe) at the free surface:

→The skimmings are richer in Al and Fe then the melt, assume the excess is oxide

$$r^S_{Al,Fe} = \frac{\Delta m^S_{Al,Fe}}{\Delta t} = \frac{m^s\left(x^S_{Al,Fe} - x^b_{Al,Fe}\right)}{\Delta t}$$

$\Delta m^S_{Al,\,Fe}$ ≡ mass of Al or Fe consumed at the surface

Δt ≡ bubbling time

m^s ≡ mass of skimmings produced over Δt

$x^s_{Al,\,Fe}$ ≡ mass fraction of Al or Fe in the skimmings

$x^b_{Al,\,Fe}$ ≡ mass fraction of Al or Fe in the bath

11) Air bubbling experiments-Rate of total solute (Al, Fe) consumption:

→The skimmings are richer in Al and Fe than the melt, assume the excess is oxide

$$r^{T}_{Al,Fe} = \frac{\Delta m^{T}_{Al,Fe}}{\Delta t} = \frac{m^{s}\left(x^{s}_{Al,Fe} - x^{b}_{Al,Fe}\right)}{\Delta t}$$

$\Delta m^{T}_{Al,\,Fe}$ ≡ total mass of Al or Fe consumed

Δt ≡ bubbling time

m^{s} ≡ mass of skimmings produced over Δt

$x^{s}_{Al,\,Fe}$ ≡ mass fraction of Al or Fe in the skimmings

$x^{b}_{Al,\,Fe}$ ≡ mass fraction of Al or Fe in the bath

12) Rate of solute consumption (Al, Fe) at the bubble-melt interface:

→Assume the liquid side of the bubble-melt interface controls mass transfer

$$r^{B}_{Al,Fe} = r^{T}_{Al,Fe} - r^{S}_{Al,Fe} \cong k_{L_{Al,Fe}}\, a\, \Delta C_{Al,Fe}$$

$k_{L\,Al,\,Fe}$ ≡ liquid-side mass transfer coefficient for Al or Fe

a ≡ bubble-melt interfacial area

$\Delta C_{Al,\,Fe}$ ≡ difference in Al or Fe concentration between the bulk liquid and the interface

13) Liquid-side mass transfer coefficient of the solute (Al, Fe):

→Assume a fast reaction; the interfacial concentration of the solute is almost zero

$$k_{L_{Al,Fe}} = \frac{r^{B}_{Al,Fe}}{a\,\Delta C_{Al,Fe}} = \frac{r^{B}_{Al,Fe}}{a\left(C_{Al,Fe} - C^{*}_{Al,Fe}\right)} \approx \frac{r^{B}_{Al,Fe}}{a\left(C_{Al,Fe} - 0\right)} = \frac{r^{B}_{Al,Fe}}{a\, x^{b}_{Al,Fe}\, \rho_{Zn}}$$

$C_{Al,\,Fe}$ ≡ Al or Fe concentration in the bulk

$C^{*}_{Al,\,Fe}$ ≡ Al or Fe concentration at the interface

$x^{b}_{Al,\,Fe}$ ≡ mass fraction of Al or Fe in the bath/bulk

ρ_{Zn} ≡ liquid zinc density at 460°C (6530 kg/m^3)